UNIVERSITY OF CALIFORNIA

Los Angeles

Evaluation of Nonlinear Site Response of Soft Clay Using Centrifuge Models

A dissertation submitted in partial satisfaction of the

requirements for the degree Doctor of Philosophy

in Civil Engineering

by

Kamil Bekir Afacan

2014

ABSTRACT OF THE DISSERTATION

Evaluation of Nonlinear Site Response of Soft Clay Using Centrifuge Models

by

Kamil Bekir Afacan

Doctor of Philosophy in Civil Engineering

University of California, Los Angeles, 2014

Professor Scott J. Brandenberg, Chair

Centrifuge models of soft clay deposits were shaken with suites of earthquake ground motions to study site response over a wide strain range. The models were constructed in an innovative hinged-plate container to effectively reproduce one dimensional ground response boundary conditions. Dense sensor arrays facilitate back-calculation of modulus reduction and damping values that show modest misfits from empirical models. Low amplitude base motions produced nearly elastic response in which ground motions were amplified through the soil column and the fundamental site period was approximately 1.0s. High intensity base motions produced shear strains higher than 10%, mobilizing shear failure in clay at stresses larger than the undrained monotonic shear strength. I attribute these high mobilized stresses to rate effects, which should be considered in strength parameter selection for nonlinear analysis. The nonlinearity in spectral

amplification is parameterized in a form used for site terms in ground motion prediction equations to provide empirical constraint unavailable from ground motion databases.

The nonlinear site response is covered by total stress simulations of centrifuge models involving soft clay, and effective stress simulations of centrifuge models including liquefiable sand layers. Primary conclusions from the total stress analysis are (1) unreasonable shear strength values may arise from extrapolating modulus reduction curves to large strains, and properly modeling the shear strength by adjusting the high-strain region of the modulus reduction curve is essential for accurate nonlinear site response modeling, and (2) the shear strength must be adjusted for strain rate effects to capture the measured ground motions. The primary conclusion from the effective stress simulations is that ground motions following liquefaction triggering are significantly under-predicted using a modeling procedure in which the backbone stress-strain behavior is degraded as pore pressures develop in accordance with a pore pressure generation function. These models fail to capture the dilatancy behavior of liquefied sand that manifests as a transient stiffening in undrained loading, and enables propagation of high amplitude high frequency acceleration pulses. Constitutive models capturing the dilatancy behavior are demonstrated to have the capability to replicate these acceleration pulses, but the resulting ground motions are highly sensitive to input parameters.

The dissertation of Kamil Bekir Afacan is approved.

Jonathan P. Stewart

Hongquan Xu

Scott J. Brandenberg, Committee Chair

University of California, Los Angeles

2014

... To my beloved family.

CONTENTS

LIST OF FIGURES

LIST OF TABLES

ACKNOWLEDGMENTS

I would like to express my sincere gratitude to my advisor and the committee chair, Professor Scott J. Brandenberg, who helped me a lot and provided me with all the knowledge and essentials required to accomplish this dissertation. I would also like to thank Professor Jonathan P. Stewart for his encouragement and great support.

The performing of the test and collection of data presented in this thesis would not have been possible without the help of Alek Harounian, DongSoon Park and Lijun Deng. I would also like to thank nees@UCDavis staff, including Dan Wilson, Chat Justice, Ray Gerhardy and Anatoliy Ganchenko for their help during the test. I am also grateful to the NEEShub Team including Stanislav Pejsa,Gregory P. Rodgers, Gemez Marshall who helped me for uploading to the data to the repository. I would also like to thank Youssef Hashash for his input related to DeepSoil modeling.

Last, but not the least, I would like to express my appreciation to my family and friends for their unconditional love and endless support.

CURRICULUM VITAE

Education

2004	B.S., Civil Engineering Department of Civil Engineering Istanbul Technical University - Istanbul, Turkey
2004-2007	M.S., Civil Engineering Department of Civil Engineering Istanbul Technical University - Istanbul, Turkey
2010-2014	Graduate Research Assistant Department of Civil and Environmental Engineering University of California, Los Angeles
2010-2014	Teaching Assistant Department of Civil and Environmental Engineering University of California, Los Angeles

Professional Work Experience

2004-2005	Site Engineer Yalova Concrete Company - Ankara, Turkey
2005-2006	Project Engineer Technovision Engineering - Ankara, Turkey
2006-2008	Project Engineer Basyazicioglu Construction - Ankara, Turkey

SELECTED PUBLICATIONS AND PRESENTATIONS

Journal Papers

Ozkan, M.T., and **Afacan, K.B**., (2007). "Investigation on Axial Load Capacity of Pile Walls by Finite Elements Methods", The First Specific Symposium of Soil Mechanic and Foundation Engineering, Istanbul

Afacan, KB, SJ Brandenberg, and JP Stewart (2013). "Centrifuge modeling studies of site response in soft clay over wide strain range," J. Geotech. Geoenviron. Eng., DOI: 10.1061/(ASCE)GT.1943-5606.0001014

Reports

Brandenberg, S.J., Stewart, J.P., **Afacan, K.B**., Harounian, A., Deng, L., and Park, D, (2010), "Final Report for USGS Award Number 08HQGR0037: Evaluation of nonlinear site response of soft clay using centrifuge models": pg. United States Geological Survey

Harounian, A., **Afacan, K.B.**, Stewart, J.P., and Brandenberg, S.J. (2010). "AHA02: Evaluationof nonlinear site response of soft clay using centrifuge models." Network for Earthquake Engineering Simulation (database). Dataset. DOI: 10.4231/D3XK84Q4D

Harounian, A., **Afacan, K.B.**, Stewart, J.P., and Brandenberg, S.J. (2009). "AHA01: Evaluation of nonlinear site response of soft clay using centrifuge models." Network for Earthquake Engineering Simulation (database). Dataset. DOI: 10.4231/D32B8VB9D

1 INTRODUCTION

1.1 GENERAL BACKGROUND AND MOTIVATION

The influence of soil conditions on earthquake ground motions is typically evaluated in practice either through the use of simplified site amplification functions or site-specific one-dimensional (1-D) ground response analysis. Site amplification functions are typically empirically derived from ground motion data (e.g., Borcherdt, 1994), but the available data cannot fully constrain highly nonlinear site response. The nonlinear component of site amplification functions is therefore often constrained by ground response analyses for regional site profiles (e.g., Walling et al., 2008). Because site amplification functions utilize relatively generic descriptions of site condition (e.g., time-averaged shear wave velocity in the upper 30 m, V_{s30}), their estimates of site amplification can be more approximate than those from ground response analysis, which use more site-specific information (e.g., Baturay and Stewart, 2003).

While both site amplification functions and site-specific analyses draw upon ground response modeling, there is considerable ambiguity on how those simulations should be performed for conditions producing large-strain site response. The two principal options for ground response analysis are equivalent linear methods (EL), in which the soil is modeled as visco-elastic with shear modulus and damping selected to be compatible with the level of mobilized shear strain, or nonlinear methods (NL), in which plasticity models are utilized to simulate the soil's constitutive behavior. The equivalent linear method has historically been more popular than nonlinear analysis in practice (Kramer and Paulsen 2004), although there is a general consensus that nonlinear analysis is preferred for high intensity motions that mobilize large-strain response in the soil (i.e., for shear strains approaching 1% or more), and nonlinear methods are now more commonly used in practice. A number of hurdles related to parameter selection and other matters have tempered the use of nonlinear methods, although many of those issues have been addressed in recent work (e.g., Kwok et al., 2007; Stewart and Kwok, 2008; Phillips and Hashash, 2009; and Hashash et al., 2010).

One problem for NL methods is the lack of available data for validation. This lack of data was the motivation for the research presented in this study, in which centrifuge models were developed to study nonlinear site response. Previous centrifuge studies utilized shear beam containers that were not ideally suited to site response studies. Since the time of the earlier centrifuge testing for site response, UC Davis developed a more flexible hinged-plate container that is better suited to site response analysis.

This problem is of considerable practical importance because design-level ground motions in seismically active regions are strong, and in soft soils will induce large strain response of the type investigated here. Moreover, large-strain response is the condition where nonlinear analysis is thought to be most useful, yet for which the available data for validation is most sparse (e.g., Yee et al., 2013).

The work described in Chapter 2 to Chapter 4 was undertaken

(i) to fill the gap in available data for 1-D soil response at very large strains approaching shear failure for the purpose of ultimately validating nonlinear ground response analysis methods; and

(ii) for validating the nonlinear component of relatively simplified amplification functions.

Another important feature of nonlinear site response analysis is modeling the stress-strain behavior of the soil. Constitutive models for total stress analysis often define a backbone curve (or alternatively a modulus reduction curve), and prescribe unload/reload rules often following Masing's (1926) rules. This approach may adequately represent the behavior of soils that exhibit similar stress-strain curves from cycle-to-cycle, but using a constant backbone curve is inappropriate for soils that exhibit cyclic degradation and development of significant excess pore water pressure.

To adapt this approach for liquefiable sands, Matasović and Vucetic (1993) developed a procedure in which the backbone curve is degraded as excess pore water pressure develops. Development of excess pore pressure is commonly related to the amount of accumulated plastic shear strain that exceeds the threshold shear strain for pore pressure generation. Although such models can capture the development of excess pore pressure due to cyclic degradation, they do not capture transient stiffening associated with dilatancy.

A common observation from these models is that the first layer that liquefies becomes soft and absorbs more plastic shear strain as a result of softening, thereby becoming even softer and absorbing even more plastic shear strain. A localization forms in which the liquefied layer absorbs much of the seismic energy and acts as a soft “base isolator” that reflects seismic waves downward and protects overlying layers (Friedland et al. 2003). This “base isolator” effect is in conflict with many recorded ground motions from liquefiable sites because it does not allow for dilatancy behavior.

More complex effective stress constitutive models for sand (e.g., Yang et al. 2003, Dafalias and Manzari 2004, Hartvigsen 2007, Boulanger 2010) have the ability to capture dilatancy-induced stress-strain behavior. These models are computationally demanding and require large numbers of (often 10 or more) input parameters, rendering the codes impractical for routine engineering applications. However, such simulations may be justified for important projects. Running site response simulations using these models has only recently become approachable as computing power has advanced.

The work described in Chapter 5 focus on identifying existing nonlinear ground response analysis codes suitable for prediction of ground motions in liquefied soil, including dilatancy effects.

1.2 PREVIOUS CENTRIFUGE SITE RESPONSE SIMULATIONS:

Lai et al. (2001) and Elgamal et al. (2005) performed site response simulations of stiff sand deposits using the UC Davis centrifuge, and calibrated constitutive models for nonlinear numerical simulations. Sand models were constructed in a flexible shear beam container (FSB2), various earthquake motions were imposed on the base of the models, and the centrifuge was spun at various g-levels to simulate different soil depths. Utilizing accelerometers that were embedded in the soil, stress-strain relations were obtained. For comparison purposes with relations derived from laboratory simple shear tests, modulus reduction and damping curves were computed from the stress-strain loops. Although the shapes of the curves were similar, the computed modulus reduction curves were generally slightly lower than those of Hardin and Drnevich (1972) and Seed and Idriss (1970). Especially for shear strains smaller than about 0.1% the observed damping ratios were larger than published relations. Elgamal et al. (2005) explained that the reason of the higher damping was unknown and that further studies are needed to characterize the influence of the soil container on site response.

Utilizing wavelet analysis to analyze the time-dependent frequency content of vertical array acceleration data, they observed that near the walls of the container the frequency content of the ground motion was spread over a larger band than the motions near the center of the model. Moreover, shear strains were larger near the walls of the shear beam container for saturated sand models. These observations were attributed in part to p-waves generated at the container boundary.

Brennan et al. (2005) published some data processing techniques that were used to develop stress-strain loops from measured accelerations. Also, they showed that filtering affects the stress strain loops, and identified the potential for spatial aliasing, wherein the accelerometers are spaced at distances larger than half of a wavelength. Since wavelength depends on the shear wave velocity and frequency, the most critical waves for aliasing would correspond to low shear wave velocity, hence low modulus. Based on their study, accelerometers were spaced at intervals of 100 mm, and they acknowledged the possibility that some waves were spatially aliased, with the effect expected to be larger at high shear strains where modulus reduction renders a softer material. At higher shear strains attributed to inherent variability in the measurements, modulus reduction curves computed from their study contained significant scatter, In the case of sand, damping showed significant scatter distributed about published trends. On the other hand, damping for clay was significantly higher than published trends. The high damping for clay corresponded to rate effects induced by the high shaking frequencies required by centrifuge scaling laws. Although much of the data from aforementioned studies are useful to design an effective instrumentation and data processing program, the scatter in the measurements was too large to validate one-dimensional site response codes. This is mostly pronounced in cases where large shear strain values are required for validation of nonlinear codes.

In this study I am pursuing to advance various factors that have been described as limitations in the past studies, such as the influence of the model container on wave propagation, characterization of damping of seismic waves through the base shaker, dense sensor arrays to minimize the influence of spatial aliasing on computation of stress-strain loops, and accurate measurements of shear wave velocity with better spatial coverage than previously possible.

1.3 ORGANIZATION OF THE THESIS

Chapter 2 presents the centrifuge models with subsections of the test configuration, soil properties, instrumentation, scale factors, shear wave velocity measurements, base motion sequence and the dynamic data presentation. Then, the process of the raw test data will be explained and limitations of the recorded data will be listed. Chapter 3 presents observations from the data, including the noise level, the container performance, filtering and data processing, stress-strain curves, modulus reduction and damping curves, response spectra and spectral amplification factors between the surface and base. Chapter 4 interprets the data with site response simulations in terms of influence of undrained shear strength, modeling platforms (DeepSoil versus OpenSees), modeling approaches (nonlinear versus equivalent linear) and importance of strain rate correction. Then, the residuals of some intensity measures are discussed. Chapter 5 focuses on the effective stress nonlinear site response analysis of centrifuge models to understand the liquefaction triggering and dilatancy. The chapter discusses the acceleration pulses in liquefied sites, presents some pore pressure and advanced constitutive models, finally introduces the effective stress site response models and compares the results of site response simulations. Chapter 6 presents the conclusion and possible future research topics.

2 CENTRIFUGE MODELS

This chapter presents the centrifuge models constructed at UC Davis. This work was performed by Alek Harounian, a UCLA BS and MS alumnus whose MS thesis work involved constructing and testing the centrifuge models. Interpretation of the test data was beyond the scope of Alek's work, and this effort constitutes a portion of my PhD efforts. First, the model configuration will be discussed and the soil properties and the instrumentation will be shown. The shear wave velocity measurements for the soil profile will be explained. Later, the base motions applied to the centrifuge container will be presented. Finally, the test data processing procedures will be explained and limitations of the recorded data will be listed.

Two centrifuge models were constructed from layers of soft San Francisco bay mud separated by thin layers of dense Nevada sand to provide drainage boundaries. San Francisco bay mud was selected for this study because it is naturally occurring clay from a seismically active region, its dynamic properties have been previously studied, and ground motion recordings are available for multiple sites that are underlain by bay mud from which prior work has evaluated site amplification that can be compared to the results of this study. Another reason is that bay mud has a high plasticity index and is not anticipated to lose significant strength during shearing.

Thus, ground motions can be generated in rapid succession without waiting for consolidation since there is no expectation of significant pore pressure.

Model AHA02 is discussed in detail herein. Details of model AHA01 can be found in Harounian et al. (2009). The models were very similar with the primary difference being that AHA02 had a thinner normally-consolidated clay layer and a thicker sand layer on top.

2.1 AHA02 CONFIGURATION

Figure 2.1 and Figure 2.2 show the soil profile for model AHA02. The model consisted of seven layers of clay, and the upper three layers were very lightly overconsolidated (nearly normally consolidated) and the lower four layers were overconsolidated. The high plasticity of bay mud renders low permeability and slow consolidation times, so thin layers of dense Monterey sand were placed between the clay layers to act as drainage boundaries to facilitate specimen construction. These thin sand layers likely introduced a small amount of phase shift as the waves propagated vertically through the soil profile, but are not anticipated to significantly alter site response considering that they are stiff, strong, and thin relative to the clay layers, and also thin relative to the wavelengths of the vertically propagating shear waves (e.g., Santamarina et al. 2001).

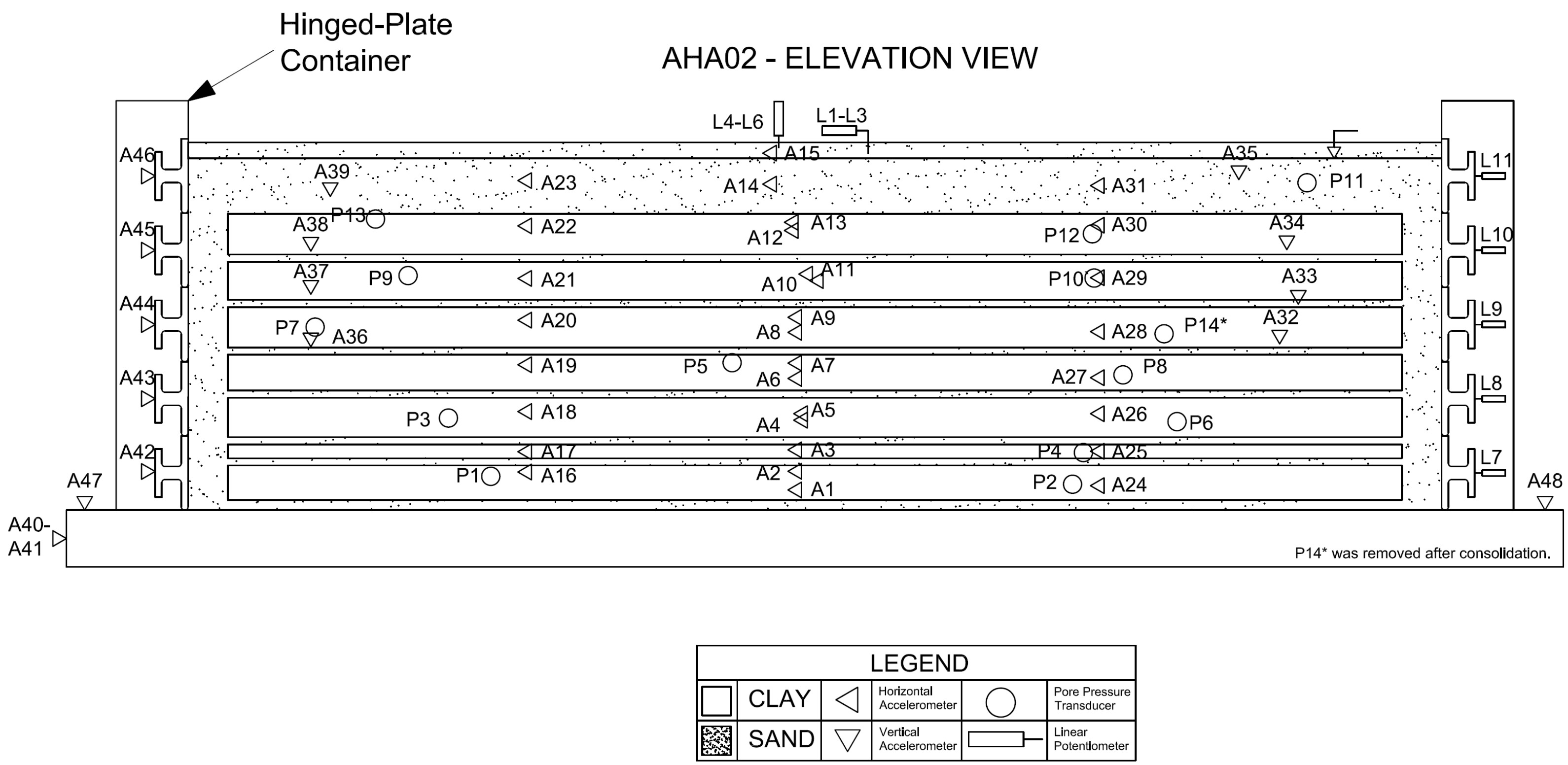

Figure 2.1 Elevation view of the model

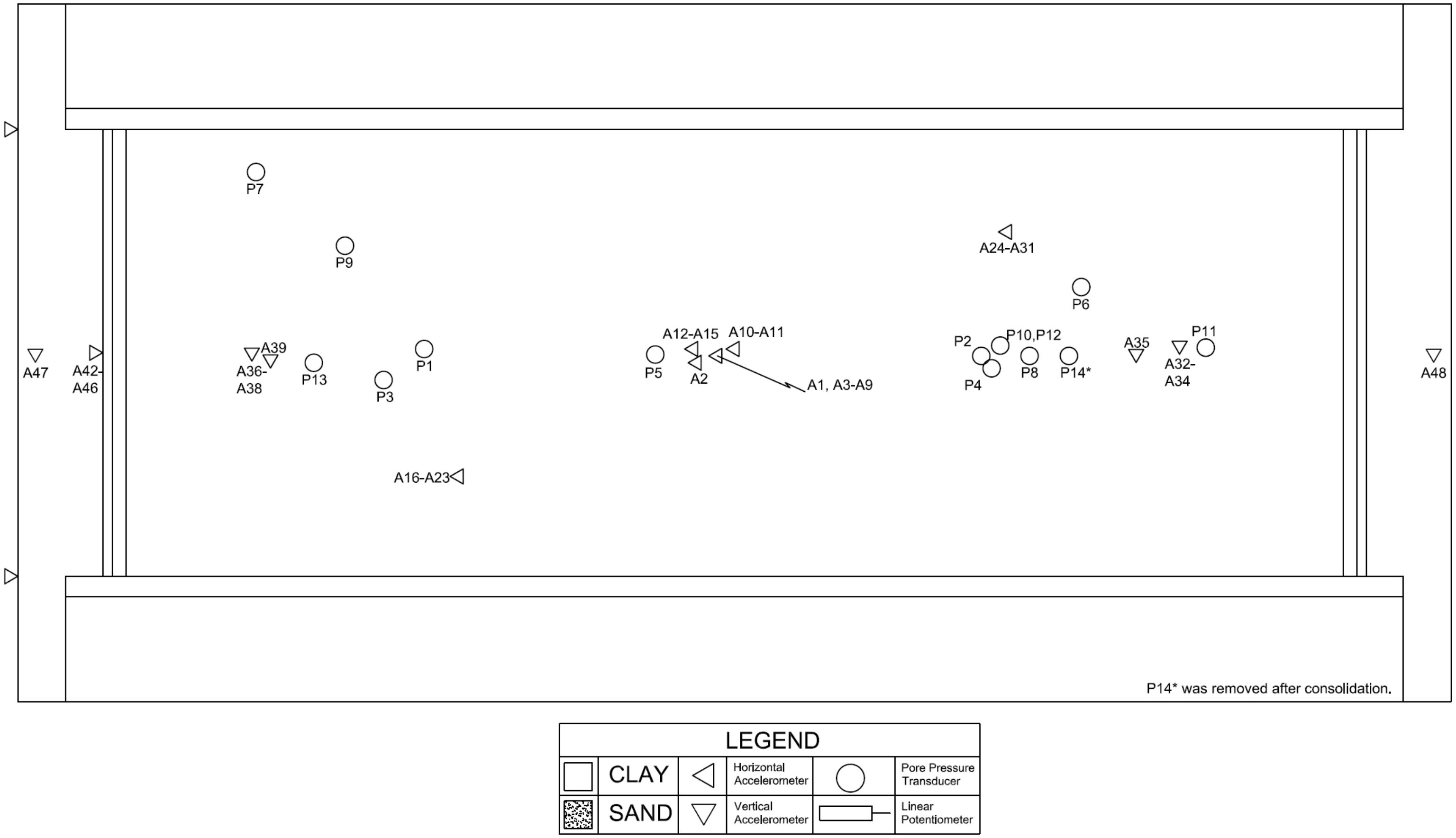

Figure 2.2 Plan View of the model

Figure 2.3 shows the hinged-plate model container that is well-suited for site response studies, and was utilized for the first time in this study. The container consists of five steel rings resting atop ball bearings, and the ends of the container are free to rotate. The container is extremely flexible in shear, and can easily be deformed by hand. Hence, the effects of container stiffness are essentially zero, and stiffness of the soil model is attributed entirely to the soil inside the container.

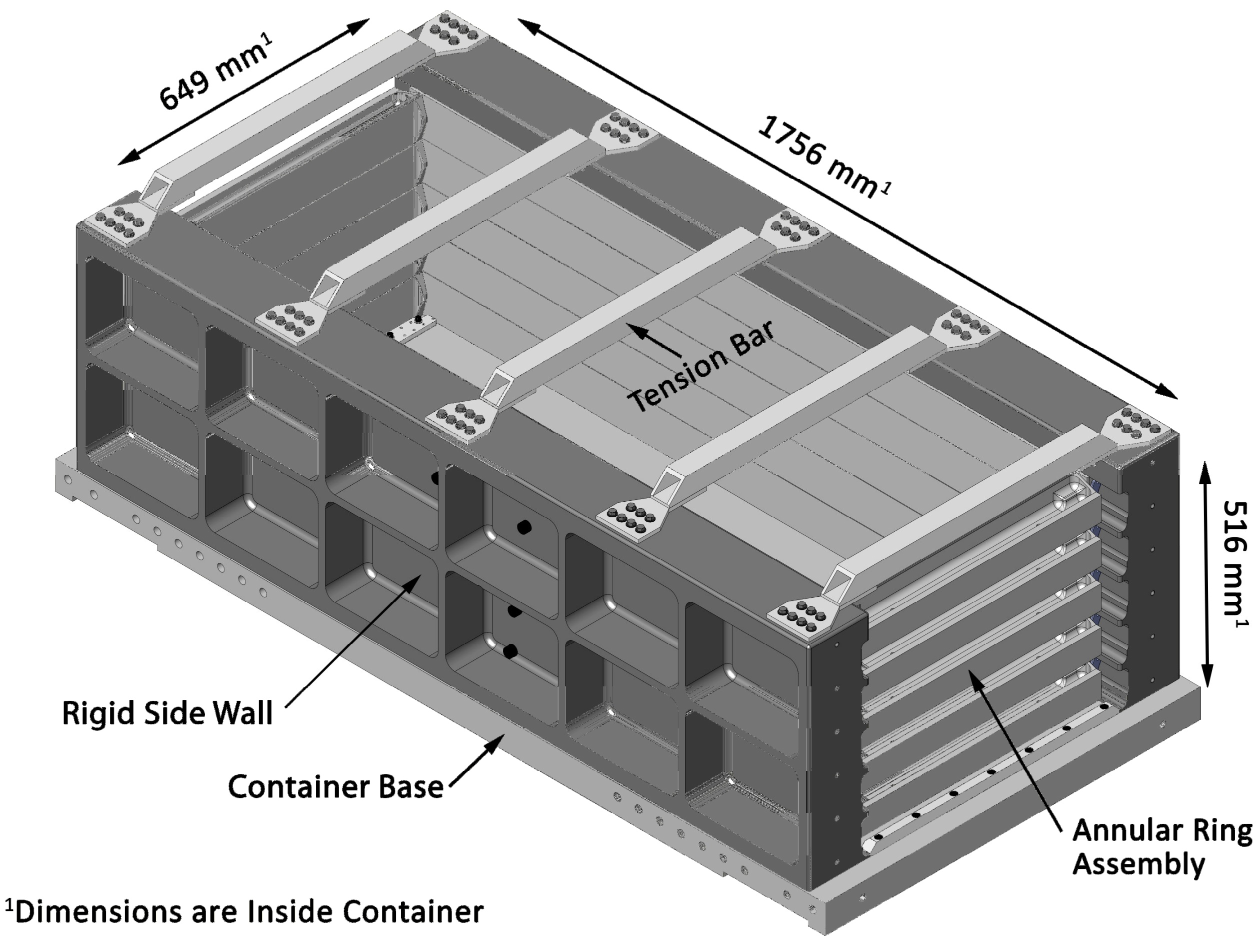

Figure 2.3 Hinged plate container used in this study

Figure 2.4 illustrates shear beam containers that had been widely utilized in previous centrifuge studies that consist of aluminum rings separated by flexible layers. The shear beam container is flexible relative to a stiff soil profile, but much stiffer than the hinged-plate container. The influence of container stiffness is particularly important for soft soils, where non one-dimensional boundary conditions could be significant. For instance, sloshing of liquefied sand has been observed in the shear beam containers.

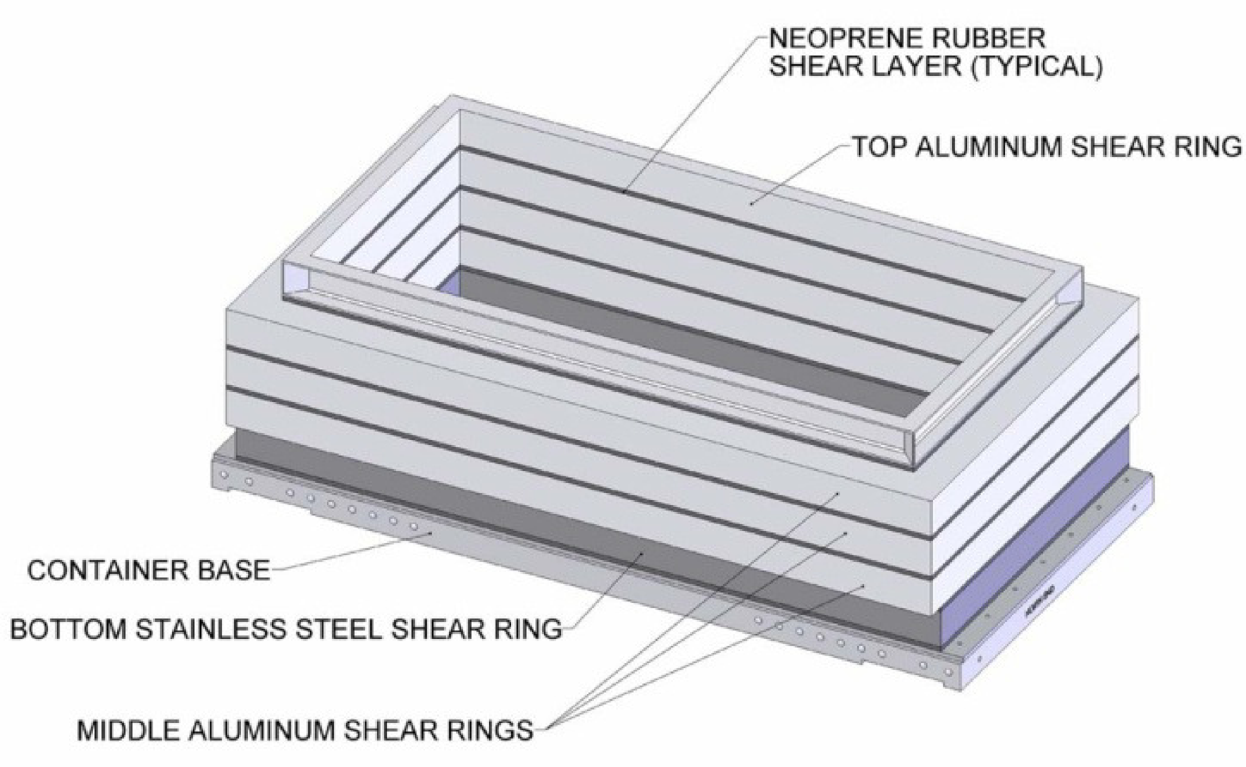

Figure 2.4 Shear beam container used in previous studies

The bay mud was mixed as a slurry to a water content of about 140% of its liquid limit for a period of at least 24 hours using a large electric mixing tank. The slurry was poured into the model container using buckets so that the final thickness of the clay after consolidation would be approximately 5 to 6 cm. Two piezometers were placed near the center of the slurry and a thick layer of Nevada sand was placed atop the slurry. A geotextile was placed atop the sand, and a steel plate attached to two vertical hydraulic pistons was lowered onto the surface of the geotextile. The purpose of the thick Nevada sand layer and geotextile was to provide a seal to prevent the slurry from oozing out of the model container during consolidation. Oil-based modeling clay was placed in the gap (approx. 1/4") between the model container walls and the press plate. A small increment of vertical stress was imposed on the clay slurry and the model was carefully monitored to make sure slurry was not oozing out under the imposed pressure. Displacement sensors were placed atop the press plate, and displacement and pore pressures were monitored over time. When pore pressure in the center of the clay slurry began to dissipate, the load increment was increased slightly, and the process was repeated until the consolidation stress had reached the desired level. The vertical total stress was then decreased in increments to prevent the suction water pressure from approaching -100kPa, at which point the pore fluid in the porous stone could cavitate and damage the strain gauge membrane in the piezometer. When the press plate was lifted from the model container, accelerometers and bender elements were placed in small excavations cut into the clay, and consolidated clay was pressed back into the excavation to embed the sensors. The consolidation process was repeated for each lift, and typically required about 3 days to a week per lift, depending on the final consolidation stress.

2.2 SOIL PROPERTIES

The characteristics of soil properties are shown in Table 2.1. The bay mud has a PI of 40-43% and USCS classification of MH. The sand material has no fines and a USCS classification of SP. Laboratory tests were performed as part of this study which included consolidation, specific gravity, Atterberg limits, and water content. Additionally, undrained shear strength was measured using a small hand vane shear device immediately after spinning down the centrifuge.

The consolidation tests performed on the bay mud are shown in Figure 2.5. In the first test, an undisturbed block sample of the clay was used whereas the second test was performed on a remolded portion of the same block of clay. The purpose of these tests was to provide some guidance on how the shear strains accumulated by the clay during simulated ground motions. This is anticipated to affect the clay's memory of its stress history. The consolidation curves indicate that $C_c = 0.43$ and $C_r = 0.04$.

Table 2.1 Properties of soils used in the centrifuge model

Parameter	**CLAY**	**SAND**
Soil Type	Bay Mud	Nevada Sand
USCS	MH	SP
Specific Gravity	2.65	2.64
Mean grain size, D_{50} (mm)	-	0.17
Coefficient of uniformity, C_u	-	1.64
Relative density (%)	-	80.00
Unit weight, γ(kN/m^3)[a]	16-17	19.80
Compression index, C_c	0.43	-
Recompression index, C_r	0.04	-
PL (%)	40-43	-
LL (%)	84-86	-
FC (%)	100	-
Friction angle, φ', (°)[b]	20	-

[a] $\gamma = \dfrac{\gamma_w G_s \left(1+w\right)}{1+wG_s}$

[b]Park(2011)

Figure 2.6 shows the values of coefficient of consolidation, c_v, that was computed using Casagrande's log-time method. The consolidation of the clay slurry is significantly nonlinear, and deviations from Terzaghi's one-dimensional consolidation theory (from which c_v is derived) are anticipated since permeability and compressibility are expected to change significantly throughout the profile of the slurry (e.g., Fox 1999).

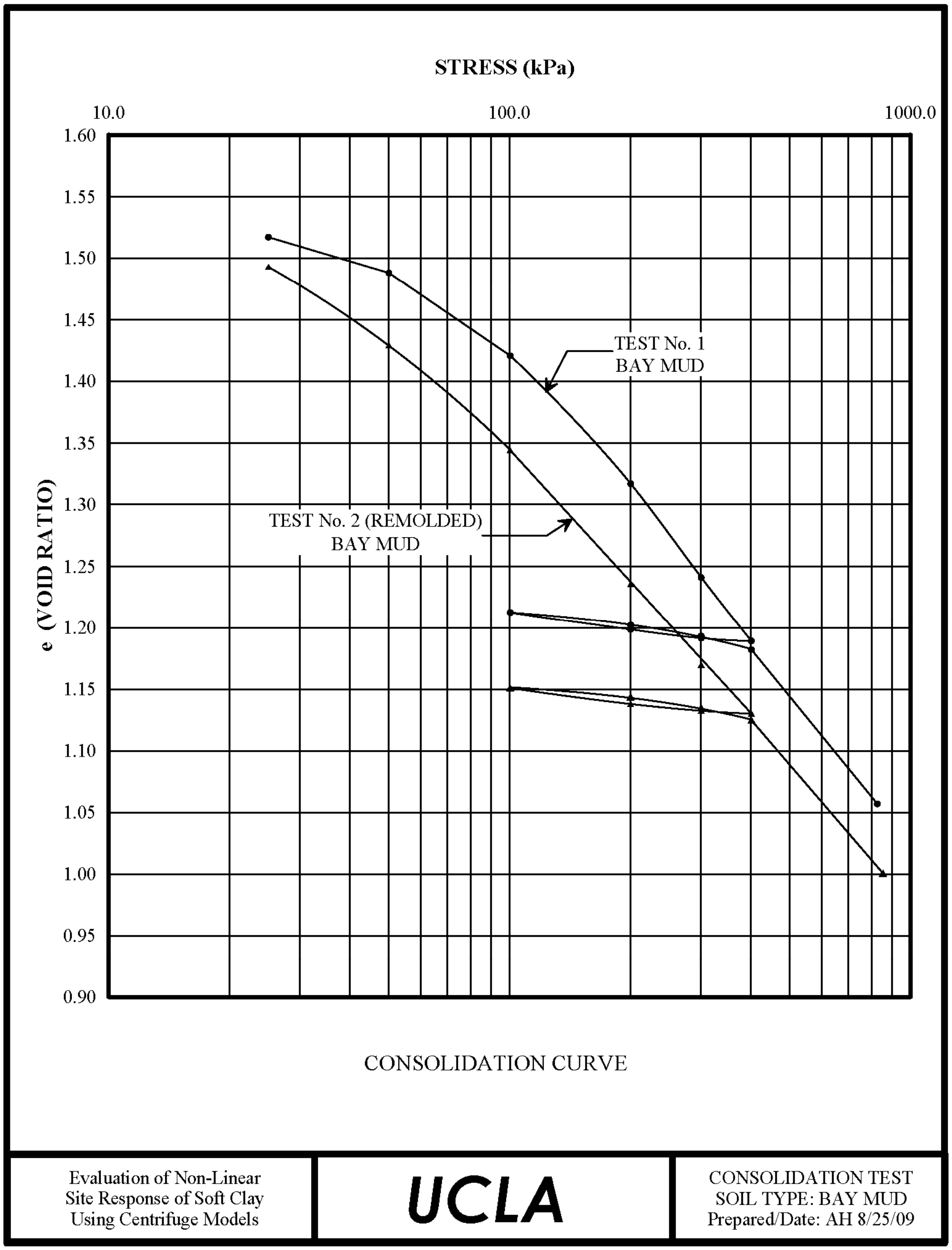

Figure 2.5 Consolidation test on clay slurry

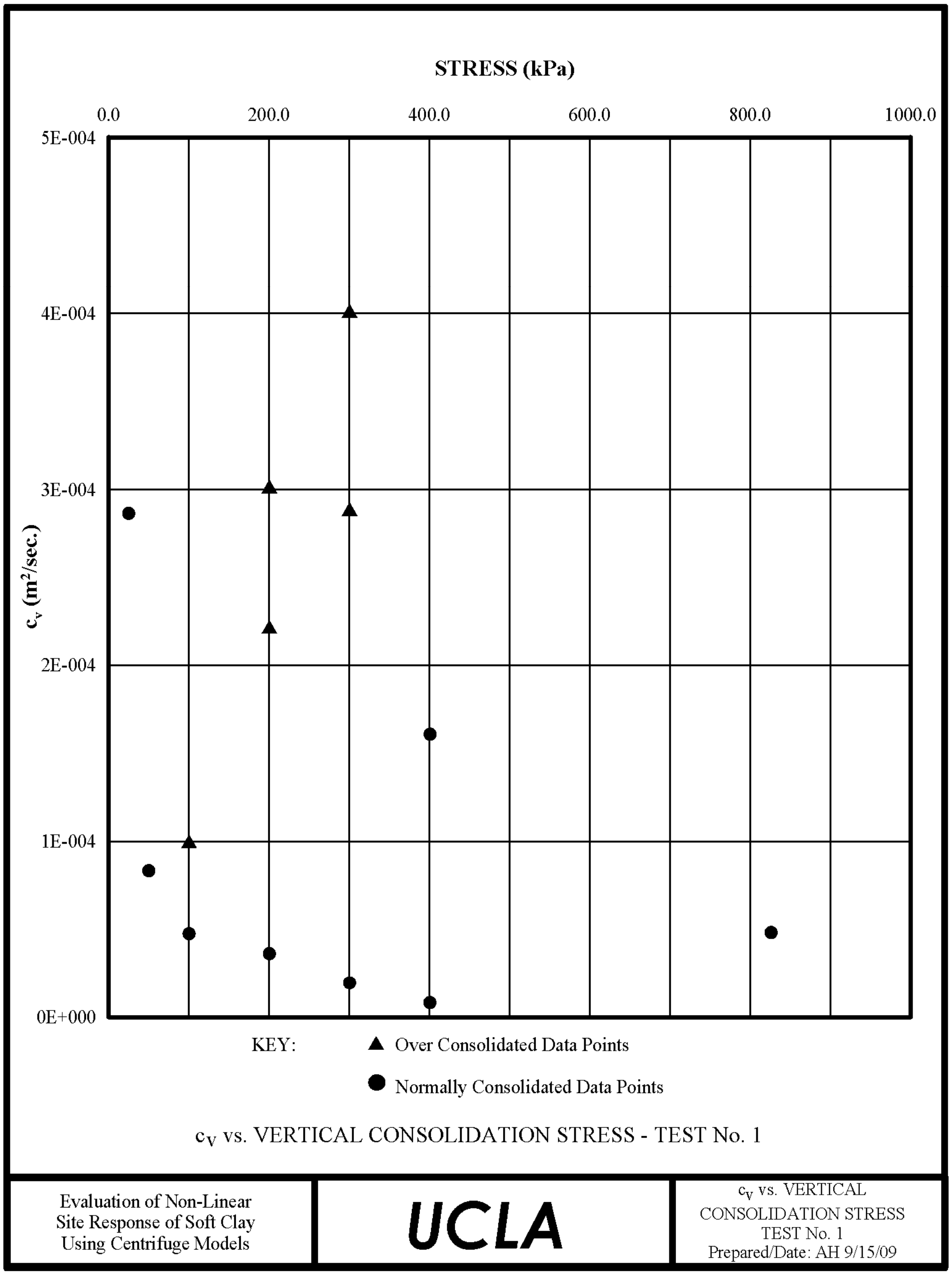

Figure 2.6 Coefficient of consolidation test No 1

The clay was placed as slurry and subsequently consolidated in seven lifts using a hydraulic press. Layers of 1 cm thick dense sand were placed at the top and bottom of each clay lift to provide drainage boundaries. During consolidation, the vertical effective stress and vertical displacements were continuously monitored using two pore pressure transducers in the center of the clay layer. Two linear potentiometers attached to the hydraulic press plate. Typically pore pressure in the center of the slurry would stay constant for about a day, and pressure increases could then proceed as the clay began gaining strength in the center. The vertical pressure was increased slowly until the target vertical stress was reached. Figure 2.7 shows an example data that was recorded during consolidation of lift 4.

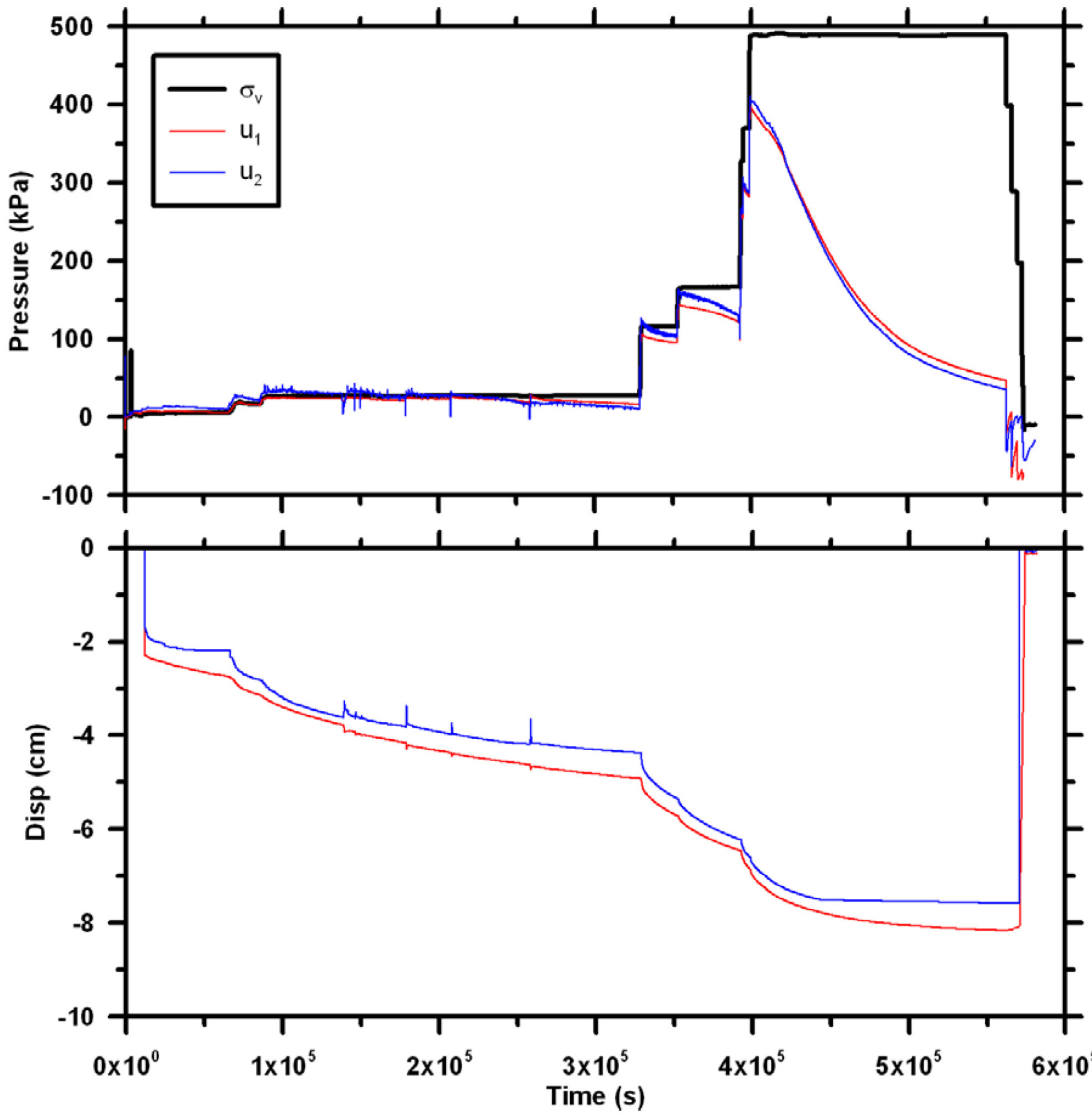

Figure 2.7 Vertical pressure, pore pressure and displacement time series for Lift 4

The initial pressure increment for lift 4 was close to 15 kPa. The pressure was initially set too high, and some clay began oozing from the model. This is also observed in sudden increase in displacement near the beginning of consolidation. This pressure increment was then reduced to 15 kPa, which prevented oozing of clay from the model, and this pressure was left constant on the clay for about 17 hours (0.6×10^5 seconds) before it was increased slightly. Then, after around

92 hours (3.3×10^5 seconds), the amount of pressure is increased after the pore pressure dissipation and associated gain in undrained shear strength were adequate to prevent oozing of clay. After 111 hours (4×10^5 seconds), the final vertical pressure of 470 kPa is applied and it remained on the clay until pore pressure at the center of the lift was reduced to nearly zero. In order to prevent cavitation of pore fluid inside the porous stone, the press was lifted off of the clay slowly maintaining a negative pore pressure of no more than -70 kPa. This step is important not to damage the pressure transducers. The vertical stresses applied to the lifts are shown below in Table 2.2.

Table 2.2 Vertical consolidation stresses applied to the lifts

Lift (#)	Vertical Stress (kPa)
1.Lift	470
2.Lift	470
3.Lift	470
4.Lift	470
5.Lift	132
6.Lift	111.2
7.Lift	82.4

The consolidation data for each lift has been archived on the NEEShub data repository for each lift. The consolidation test results provide a means of estimating the unit weight of the clay during spinning after reconsolidating to the in-flight effective stresses. It should be noted that water contents cannot be measured in flight to estimate unit weights since the clay consolidates following spin up and swells during spin-down. Hence, the analysis is required to estimate the in-flight unit weights and the resulting effective stress profile. The void ratio of the clay (e) can be computed using the consolidation curve and knowledge of the stress history as shown in Eq. (2.1):

$$e = e_{ref} - \left[C_c \log\left(\frac{\sigma'_{vc}}{\sigma'_{v,ref}} \right) - C_r \log\left(\frac{\sigma'_{v}}{\sigma'_{vc}} \right) \right] \tag{2.1}$$

The unit weight (i.e. γ) can then be computed using Eq. (2.2). (The clay is assumed to be fully saturated)

$$\gamma_{clay} = \frac{\gamma_w \left(G_s + e \right)}{1 + e} \tag{2.2}$$

Assuming γ_w = 10 kN/m^3, G_s = 2.65, C_c = 0.43, C_r = 0.04, e_{ref} = 1.46, and $\sigma_{v,ref}'$ = 240 kPa (e_{ref} and $\sigma_{v,ref}'$ are selected as any point on the virgin compression portion of the consolidation curve), the unit weights of the clay were computed and the distributions of vertical effective stress and overconsolidation ratio anticipated during spinning are plotted in Figure 2.8. The undrained shear strength was estimated from the vertical effective stress using strength normalization concepts (Ladd 1991). Shear wave velocity measurements were estimated by the travel times from a combination of bender element test data which will be presented in further sections, and low-amplitude high-frequency sine waves imposed on the base of the model. Additionally, knowledge of the dependence of V_s on consolidation stress was used to develop the profiles shown in Figure 2.8.

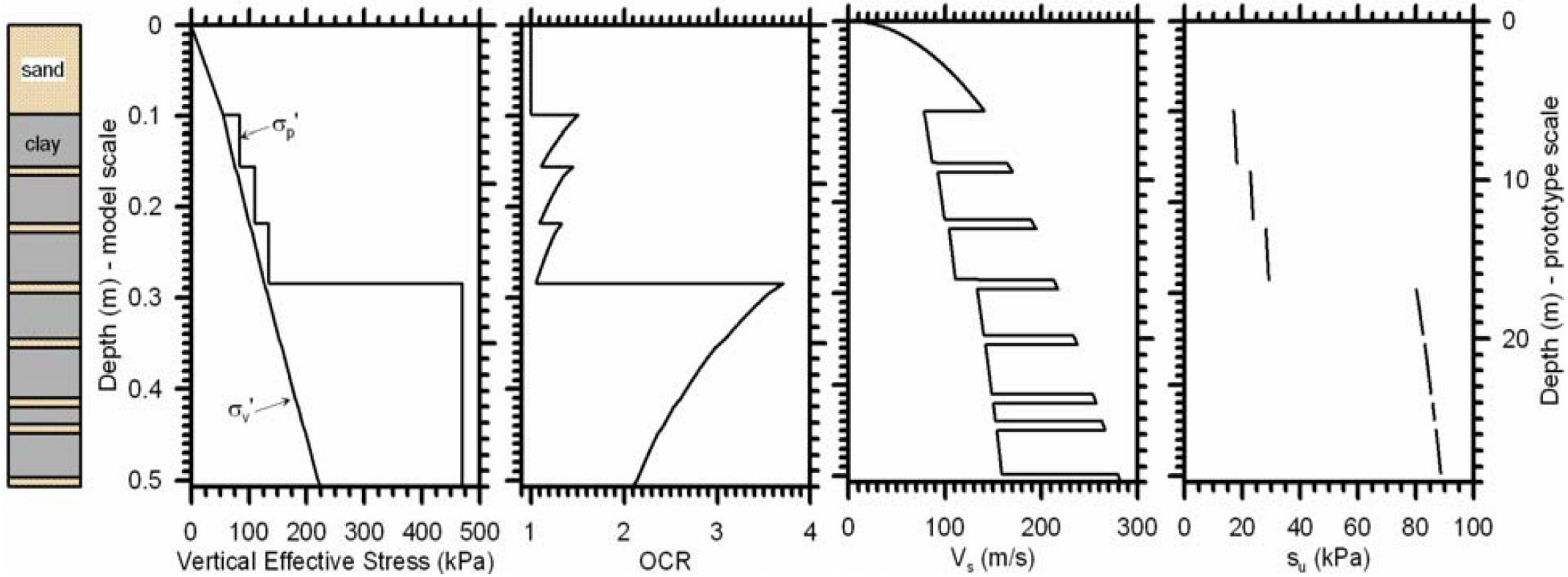

Figure 2.8 **Profile of vertical effective stress, over consolidation ratio, shear wave velocity and undrained shear strength**

2.3 INSTRUMENTATION

A total of 48 accelerometers (ACC's), 13 pore pressure transducers (PPT's), and 11 linear potentiometers (LPT's) were utilized to measure the response of the model to imposed ground motions. Additionally, 24 bender elements (8 sources and 16 receivers) were embedded in the soil layers to measure shear wave velocity (discussed later). Tables 2.3, 2.4 and 2.5 define the sensor list.

Table 2.3 Sensor List: Pore pressure transducers and linear potentiometers

Sensor ID	*Serial Number*	X_{bt}	Y_{bt}	Z_{bt}	X_{at}	Y_{at}	Z_{at}	*Range*	*Orientation*	*Direction*	*Amp Channel ID*	*Sensitivity (prototype)*	*Units*	*Amplifier Gain*	*Sensitivity (prototype with gain)*
P1	11158	45.5	32		42	33	4.7	200 psi	H	West	FGD-1	4104.8041	kPa/V	50	82.0961
P2	11821	45.5	32		122	31	3.6	100 psi	H	West	FGD-12	2005.7452	kPa/V	50	40.1149
P3	11827	45	32		35.1	28.5	12.8	100 psi	H	West	FGD-0	2066.8134	kPa/V	50	41.3363
P4	12050	120	32		123.5	29.2	8.9	100 psi	H	West	FGD-6	2066.8134	kPa/V	50	41.3363
P5	11149	84	32		87.5	32.2	22.9	100 psi	H	West	FGD-2	2111.3087	kPa/V	50	42.2262
P6	11830	120	32		136.5	41	12.3	100 psi	H	West	FGD-7	2157.7728	kPa/V	50	43.1555
P7	2963400	45	32		17.6	58.7	25.5	50 psi	H	West	FGD-3	889.6461	kPa/V	50	17.7929
P8	11822	120	32		129	31	18.8	100 psi	H	West	FGD-14	1974.3351	kPa/V	50	39.4867
P9	11139	45	32		30.5	48	32.6	50 psi	H	West	FGD-4	953.0559	kPa/V	50	19.0611
P10	2963406	120	32		125	33.5	32.5	50 psi	H	West	FGD-15	896.8785	kPa/V	50	17.9376
P11	2973226	150	32		155.3	32.2	45.5	50 psi	H	West	FGD-5	949.1681	kPa/V	50	18.9834
P12	11760	120	32		127.5	32.5	38.4	50 psi	H	West	FGD-17	1022.6284	kPa/V	50	20.4526
P13	11141	20	32		26	31	41.8	50 psi	H	West	FGD-13	927.0257	kPa/V	50	18.5405
L1	434	-	-	-	-	-	-	-	H	South	PT0	0.5812	m/V	1	0.5812
L2	430	-	-	-	-	-	-	-	H	South	PT1	0.5812	m/V	1	0.5812
L3	435	-	-	-	-	-	-	-	H	South	PT2	0.5812	m/V	1	0.5812
L4	303	-	-	-	-	-	-	-	V	Down	PT3	0.4359	m/V	1	0.4359
L5	302	-	-	-	-	-	-	-	V	Down	PT4	0.4359	m/V	1	0.4359
L6	300	-	-	-	-	-	-	-	V	Down	PT5	0.4359	m/V	1	0.4359
L7	492	-	-	-	-	-	-	-	V	Down	PT6	0.5812	m/V	1	0.5812
L8		-	-	-	-	-	-	-	V	Down	PT7	0.5812	m/V	1	0.5812
L9	430	-	-	-	-	-	-	-	V	Down	PT8	0.5812	m/V	1	0.5812
L10	490	-	-	-	-	-	-	-	V	Down	PT9	0.5812	m/V	1	0.5812
L11	422	-	-	-	-	-	-	-	V	Down	PT10	0.5812	m/V	1	0.5812

Table 2.4 Sensor List: Accelerometers

Sensor ID	*Serial Number*	X_{bt}	Y_{bt}	Z_{bt}	X_{at}	Y_{at}	Z_{at}	*Range*	*Orientation*	*Direction*	*Amp Channel ID*	*Sensitivity (prototype)*	*Units*	*Amplifier Gain*	*Sensitivity (prototype with gain)*
A1	99514	83	32	3.5	86.5	31	2.8	100 g	H	South	PCB1-1	0.3415	g/V	1	0.3415
A2	73964	83	32	5.9	83.5	31	5.4	100 g	H	South	PCB1-2	0.3286	g/V	1	0.3286
A3	5604	83	32	10.11	86.5	32	9.4	100 g	H	South	PCB1-5	0.3274	g/V	1	0.3274
A4	99516	83	32	12.7	87.3	32	12.5	100 g	H	South	PCB1-8	0.3490	g/V	1	0.3490
A5	99518	83	32	13.8	87.3	32.3	13.4	100 g	H	South	PCB1-9	0.3525	g/V	1	0.3525
A6	5607	83	32	28.2	86.5	32.5	18.3	100 g	H	South	PCB1-12	0.3232	g/V	1	0.3232
A7	99512	83	32	20.4	86.5	32.5	20.9	100 g	H	South	PCB1-13	0.3490	g/V	1	0.3490
A8	99517	83	32	24.8	86.5	32.2	24.7	100 g	H	South	PCB1-14	0.3362	g/V	1	0.3362
A9	73959	83	32	26.7	86.5	32.2	26.8	100 g	H	South	PCB2-1	0.3349	g/V	1	0.3349
A10	21044	77	32	32	89.5	32	31.9	100 g	H	South	PCB2-6	0.3256	g/V	1	0.3256
A11	21067	77	32	32	88	32	32.8	100 g	H	South	PCB2-7	0.3232	g/V	1	0.3232
A12	97115	83	32	38.5	85.8	33	38.86	50 g	H	South	PCB2-12	0.1754	g/V	1	0.1754
A13	96936	83	32	39.9	86	33	40	50 g	H	South	PCB2-13	0.1769	g/V	1	0.1769
A14	21323	45	14	5.9	49	14.5	45.3	100 g	H	South	PCB1-3	0.3720	g/V	1	0.3720
A15	21056	45	14	10.37	48.5	14	49.6	100 g	H	South	PCB1-6	0.3190	g/V	1	0.3190
A16	21051	45	14	14.14	49	14.8	13.7	100 g	H	South	PCB1-10	0.3356	g/V	1	0.3356
A17	99517	45	14	21.7	48	13.5	20.2	100 g	H	South	PCB1-14	0.3362	g/V	1	0.3362
A18	21071	45	14	25.7	48	13.1	26.4	100 g	H	South	PCB2-2	0.3292	g/V	1	0.3292
A19	3962	39	14	32	51	14	32.2	50 g	H	South	PCB2-8	0.1642	g/V	1	0.1642
A20	3162	45	14	39.5	48.5	14	39.5	50 g	H	South	PCB2-14	0.1617	g/V	1	0.1617
A21	4596	45	14	45.9	49.5	14.5	45.8	50 g	H	South	PCB3-4	0.1660	g/V	1	0.1660
A22	21070	126	50	4.27	128.5	49.5	3.4	100 g	H	South	PCB1-4	0.3784	g/V	1	0.3784
A23	73962	126	50	9.9	128.5	50.5	9.2	100 g	H	South	PCB1-7	0.3441	g/V	1	0.3441
A24	21048	126	50	13.4	126	56	13.8	100 g	H	South	PCB1-11	0.3408	g/V	1	0.3408
A25	5602	126	50	18.4	130	49.5	18.4	100 g	H	South	PCB1-15	0.3250	g/V	1	0.3250
A26	21061	126	50	25	129.5	50.5	24.8	100 g	H	South	PCB2-3	0.3532	g/V	1	0.3532
A27	96935	129	50	32	133	50.7	32.3	50 g	H	South	PCB2-9	0.1712	g/V	1	0.1712
A28	97114	126	50	39.5	130	50	39.6	50 g	H	South	PCB2-15	0.1745	g/V	1	0.1745
A29	3203	126	50	45.6	126.7	52	45.1	50 g	H	South	PCB3-5	0.1699	g/V	1	0.1699
A30	21046	150	32	23.3	153.5	33.5	23	100 g	V	Down	PCB2-5	0.3274	g/V	1	0.3274
A31	3955	144	32		156	32	28.6	50 g	V	Down	PCB2-11	0.1640	g/V	1	0.1640
A32	5276	150	32		154.5	32.5	36.2	50 g	V	Down	PCB3-1	0.1671	g/V	1	0.1671
A33	5272	140	32		147.2	32.3	46.1	50 g	V	Down	PCB3-7	0.1670	g/V	1	0.1670
A34	21319	16	32	23.2	19	32.5	22.7	100 g	V	Down	PCB2-4	0.3349	g/V	1	0.3349
A35	3157	10	32		21	32.5	30	50 g	V	Down	PCB2-10	0.1592	g/V	1	0.1592
A36	5270	16	32		19	32	36	50 g	V	Down	PCB2-16	0.1688	g/V	1	0.1688
A37	5274	16	32		21.7	31.5	43.6	50 g	V	Down	PCB3-6	0.1660	g/V	1	0.1660
A38	6023	-	-	-	-	-	-	100 g	H	North	PCB3-13	0.3349	g/V	1	0.3349
A39	6025	-	-	-	-	-	-	100 g	H	North	PCB3-14	0.3336	g/V	1	0.3336
A40	6022	-	-	-	-	-	-	100 g	H	South	PCB3-12	0.3274	g/V	1	0.3274
A41	6016	-	-	-	-	-	-	100 g	H	South	PCB3-11	0.3428	g/V	1	0.3428
A42	6019	-	-	-	-	-	-	100 g	H	South	PCB3-10	0.3356	g/V	1	0.3356
A43	6018	-	-	-	-	-	-	100 g	H	South	PCB3-9	0.3395	g/V	1	0.3395
A44	6015	-	-	-	-	-	-	100 g	H	South	PCB3-8	0.3190	g/V	1	0.3190
A45	107068	-	-	-	-	-	-	100 g	V	Down	PCB3-15	0.3532	g/V	1	0.3532
A46	107066	-	-	-	-	-	-	100 g	V	Down	PCB3-16	0.3462	g/V	1	0.3462

Three vertical arrays of horizontal accelerometers were embedded in the soil. The array in the center containing A1 - A15 is densely instrumented with very close sensor spacing with two accelerometers in each clay layer, and the other two arrays are less-densely instrumented. Shear strains in the clay are computed from the accelerometers at the top and bottom of each clay layer. The purpose of the less-heavily instrumented arrays is to provide redundancy and assess differences in wave propagation at different positions as an indication of non one-dimensional wave propagation due to undesired boundary conditions. Two vertical arrays of vertical accelerometers were also placed in the model to measure container rocking and any vertical deformations of the soil that occurred during rocking. Accelerometers were also placed on each of the five rings of the container at the center elevation to compare the motion of the container with the motion in the soil.

Table 2.5 The list of bender elements

Label	Channel Name	X	Y	Z	Lift #
S1	Source 1	54.8	20.5	3.1	1. Lift
R1	Bender 2	91.8	20.0	2.8	
R2	Bender 13	70.3	20.0	4.0	
S2	Source 3	64.1	20.5	12.0	3. Lift
R3	Bender 3	73.8	20.5	12.1	
R4	Bender 4	52.6	20.5	12.2	
S3	Source 4	72.8	20.0	18.0	4. Lift
R5	Bender 7	92.8	20.5	18.5	
R6	Bender 5	62.8	20.0	18.4	
R7	Bender 6	52.3	20.0	19.0	
S4	Source 5	52.8	20.0	25.5	5. Lift
R8	Bender 8	70.8	20.0	24.9	
R9	Bender 9	62.3	21.0	25.2	
R10	Bender 10	57.8	20.0	25.6	
S5	Source 6	54.8	20.5	30.6	6. Lift
R11	Bender 12	64.8	20.2	30.3	
R12	Bender 11	59.3	20.0	30.3	
S6	Source 7	58.0	20.5	38.8	7. Lift
R13	Bender 14	62.8	20.5	39.1	
R14	Bender 1	52.8	20.5	38.9	
S7	Source 8	48.8	20.0	-	Sand
R15	Bender 16	68.8	20.0	-	
R16	Bender 15	58.8	20.0	-	

2.4 SCALE FACTORS

Data are presented in prototype scale in this thesis unless otherwise noted. The scale factors used to convert the recorded data from model to prototype units are shown in the Table 2.6. The centrifugal acceleration was 57.2g during all of the shaking tests.

Table 2.6 Scale Factors

Quantity	Prototype Dimension/ Model Dimension
Time	57.2/1
Displacement, Length	57.2/1
Acceleration, Gravity	1/57.2
Force	$(57.2)^2/1$
Pressure, Stress	1/1
Permeability	57.2/1

2.5 SHEAR WAVE VELOCITY MEASUREMENTS

A total of 24 bender elements (8 source and 16 receiver) were embedded in the model to measure shear wave velocity. Bender elements can provide excellent measurements of shear wave velocity in centrifuge models because the wavelengths are short relative to the travel paths, hence high resolution travel time measurements can be made. Bender elements have provided excellent results in centrifuge models containing dry sand (e.g., Brandenberg et al. 2009), but have had problems in saturated models due to electrical isolation of the piezoelectric materials from the conductive pore water. The bender elements embedded in the first centrifuge model in this test sequence, AHA01, did not function properly because they shorted with the saturated soil. A new coating system was devices for AHA02, but unfortunately only two source/receiver pairs functioned properly. One measurement was made in the upper sand layer, and one from clay lift 5, which was the lowest normally consolidated lift of clay. Table 2.7 lists the properties of the bender elements that functioned.

Table 2.7 List of functioned bender elements

Label	Channel Name	X	Y	Z	Lift #
S4	Source 5	52.8	20.0	25.5	5. Lift
R8	Bender 8	70.8	20.0	24.9	
R9	Bender 9	62.3	21.0	25.2	
R10	Bender 10	57.8	20.0	25.6	
S7	Source 8	48.8	20.0	-	Sand
R15	Bender 16	68.8	20.0	-	
R16	Bender 15	58.8	20.0	-	

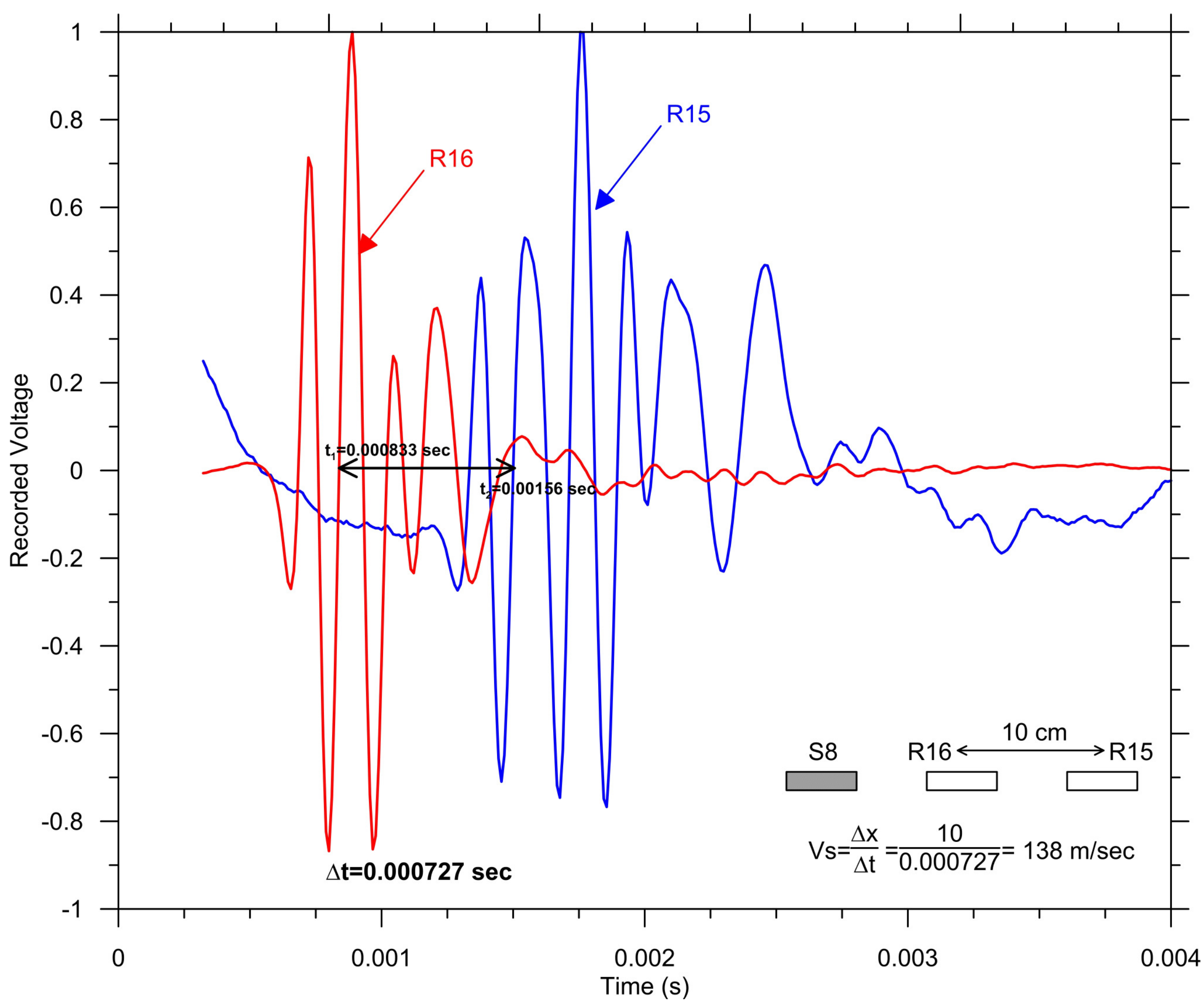

Figure 2.9 Example bender element signals from the center of the upper sand layer

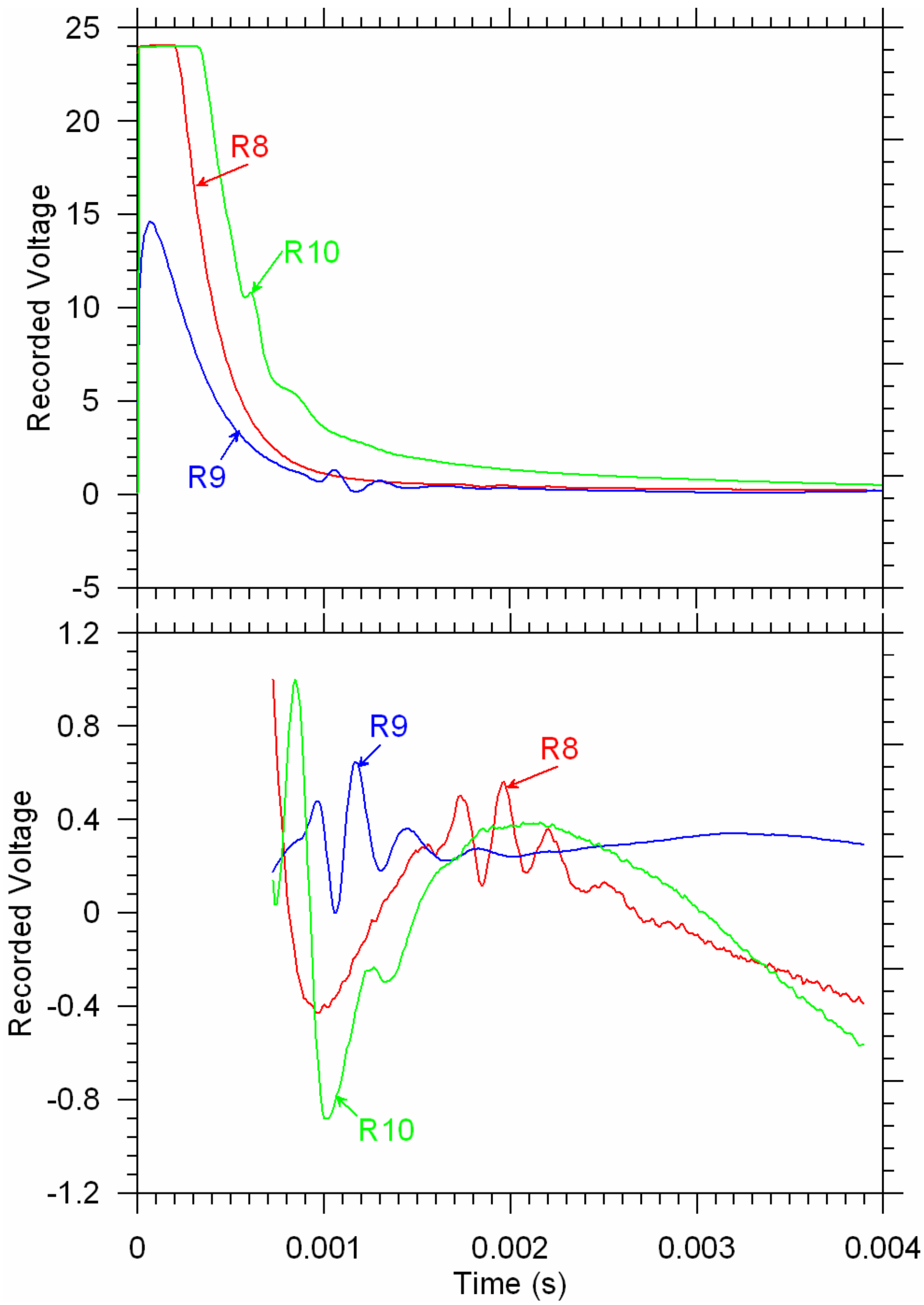

Figure 2.10 **Bender element records from S4 recorded at R8, R9 and R10. The upper figure shows the recorded data, and the lower figure shows the processed data used to make travel time picks.**

The bender elements in the sand layer provided the highest-quality data, and travel times could be measured quite accurately in the sand (Fig. 2.9). This configuration involves one source and two receivers, and receiver-to-receiver measurements were utilized to determine travel times. Figure 2.9 shows an example signal recorded while the centrifuge was spinning, and the signals have been scaled to a peak value of 1.0 to better show signal quality and make travel time picks. Similar portions of the signal were identified, and the travel time was found to be 0.000727s. The distance between the bender elements was 0.10m, and the resulting shear wave velocity is 138m/s. The depth of these bender elements could not be accurately measured because they were pushed down into uncemented dry sand. However, they were approximately located near the center of the sand layer, where σ_v' = 28 kPa. Assuming that shear wave velocity scales with the 0.25 power of effective stress (as is typical for uncemented sands), the overburden normalized shear wave velocity, V_{s1} can be computed as (138m/s)*(101.325kPa/28kPa) $^{0.25}$= 190m/s. The shear wave velocity of the sand can then be computed at any depth by assuming V_{s1} is constant using Eq. (2.3).

$$V_s = V_{s1}\left(\frac{\sigma_v'}{p_A}\right) \tag{2.3}$$

The process was repeated for several different trials conducted at various times during the tests, and very repeatable results were obtained (Table 2.8). This indicates that the stiffness of the sand did not change over time as a result of the sequence of ground motions imposed on the model.

The signals recorded in the clay layer were more difficult to interpret due to capacitive coupling between the bender elements. Figure 2.10 shows signals recorded by R8, R9 and R10 due to excitation of S4 in the center of clay lift 5. All three signals show to varying degrees, an initial spike in voltage followed by a slow decay. Unfortunately, the duration of this decay is long enough to interfere with the shear wave arrivals. However, the shear wave arrivals are apparent on top of these signals and travel times can be determined following some processing. The signals were processed by

(1) truncating the initial portion of data where the flat top portion of the signal is apparent, and the later part of the signal beyond the shear wave arrivals,

(2) fitting an exponential function to the data and subtracting this fit from the recorded data to reduce the capacitive decay portion of the signal, and

(3) scaling the data so that the shear wave arrival amplitudes were similar for making travel time picks.

Table 2.8 Results of bender element measurements in the upper sand lift from repeated trials.

#	Time Stamp	Source	Receiver	Receiver	Reading 1	Reading 2	Difference 1-2	Distance 1-2	Vs m/sec
1	3172010135812	8	15	16	0.001756	0.001033	0.000723	10	138
2	3182010114001	8	15	16	0.001878	0.001156	0.000722	10	139
3	3182010114041	8	15	16	0.001878	0.001156	0.000722	10	139
4	3182010125834	8	15	16	0.001867	0.001144	0.000723	10	138
5	3182010133251	8	15	16	0.001689	0.000967	0.000722	10	138
6	3182010142459	8	15	16	0.001667	0.000944	0.000723	10	138
7	3182010145210	8	15	16	0.001889	0.001167	0.000722	10	139
8	3182010154637	8	15	16	0.001744	0.001022	0.000722	10	138
9	3182010160434	8	15	16	0.001833	0.001111	0.000722	10	139
10	3182010161535	8	15	16	0.001744	0.001022	0.000722	10	139
11	3182010163244	8	15	16	0.001756	0.001033	0.000723	10	138
12	3182010165854	8	15	16	0.001744	0.001022	0.000722	10	139
13	3182010173840	8	15	16	0.001689	0.000967	0.000722	10	138
14	3182010175905	8	15	16	0.001560	0.000833	0.000727	10	138
15	3182010181507	8	15	16	0.001667	0.000944	0.000723	10	138

The resulting processed signals are shown in the lower half of Figure 2.10. The shear wave arrival at R8 was still obscured by the capacitive decay, but an accurate travel time pick can be made between R9 and R10. In this case, the travel time between R9 and R10 is 7.889x10-

4s, and the distance between the bender elements is 0.085m, hence the shear wave velocity is 108m/s. Measurements were repeated at various times during the testing sequence, and the shear wave velocity measurements were consistent (Table 2.9). This indicates that the stiffness of the clay did not change as a result of shear strains imposed on the models during shaking. This is also consistent with the observation that excess pore pressures generated during the shaking events tended to be relatively small.

Table 2.9 Results of bender element measurements in the center of the clay for lift 5

#	Time Stamp	Source	Rec.	Rec.	Rec.	Reading 1	Reading 2	Difference 1-2	Distance 1-2	Vs m/sec
1	3172010135634	5	8	9	10	-	-	-	8.5	-
2	3182010114216	5	8	9	10	-	-	-	8.5	-
3	3182010125727	5	8	9	10	0.0015330	0.0007444	0.0007886	8.5	108
4	3182010133150	5	8	9	10	0.0015000	0.0007111	0.0007889	8.5	108
5	3182010142353	5	8	9	10	0.0015000	0.0007222	0.0007778	8.5	109
6	3182010145052	5	8	9	10	0.0014890	0.0007111	0.0007779	8.5	109
7	3182010154527	5	8	9	10	0.0016560	0.0008667	0.0007893	8.5	108
8	3182010160336	5	8	9	10	0.0016670	0.0008778	0.0007892	8.5	108
9	3182010161442	5	8	9	10	0.0016780	0.0008889	0.0007891	8.5	108
10	3182010163155	5	8	9	10	0.0014890	0.0007111	0.0007779	8.5	109
11	3182010165701	5	8	9	10	0.0015110	0.0007330	0.0007780	8.5	109
12	3182010173727	5	8	9	10	0.0015220	0.0007330	0.0007890	8.5	108
13	3182010175735	5	8	9	10	0.0015110	0.0007222	0.0007888	8.5	108
14	3182010181349	5	8	9	10	0.0014330	0.0006444	0.0007886	8.5	108
15	3182010181410	5	8	9	10	0.0014440	0.0006556	0.0007884	8.5	108

Because the bender elements only provided a measurement of V_s in one lift of clay rather than all of the lifts as originally intended, we utilized the available measurement to calibrate relations from the literature between the maximum (small strain) shear modulus, G_{max}, confining pressure, and OCR. Yamada et al. (2008) provide the following general expression for the effective stress-dependence of G_{max} in normally consolidated soil (the equation is slightly modified here to become dimensionless):

$$\frac{G_{\max}}{p_a} = \alpha \left(\frac{\sigma'_{mc}}{p_a} \right)^n \tag{2.4}$$

where n=1.0 for clay, σ_{mc}' is the mean effectives stress, and α is dependent on soil type. Based on a similar relation by Hardin and Drnevich (1972), we expect G_{max} to be proportional to OCR^c(where c = 0.3 for clay with PI=40). We insert this term into Eq (2.4) and re-write the expression in terms of vertical effective consolidation stress σ_{vc}', as follows:

$$\frac{G_{\max}}{p_a} = \alpha \times \left(\frac{1+2K_0}{3} \right)^n \times OCR^c \left(\frac{\sigma'_{vc}}{p_a} \right)^n \tag{2.5}$$

where K_0 is the coefficient of lateral earth pressure at rest. The available bender element data is from a clay layer for which σ_{vc}' = 117 kPa, γ_{sat}=16.4 kN/m^3, and OCR=1.15; V_s=108m/s was measured in this layer. Converting V_s to G_{max} using the classical relation $V_s = \sqrt{G_{\max}/\rho}$ (where ρ is mass density) and applying $K_0 = (1-\sin\phi)\ \mathrm{OCR}^{\sin\phi} = 0.69$ [Jaky (1944) and Schmidt (1966)], we compute α=202, which is consistent with prior experience for similar materials (Yamada et al., 2008). Values of G_{max} are then obtained for other layers using α = 202 in Eq. (2.5), with the results shown in Fig. 2.8 following conversion to V_s.

We apply a similar approach for seismic velocities in sand. In this case, the overburden scaling coefficient is n=0.5 (Yamada et al., 2008) and the OCR scaling coefficient is c=0 (Hardin and Drnevich, 1972). A shear wave velocity measurement indicating V_s = 138 m/s was obtained from bender element data in the upper sand layer in AHA02 for which σ_{vc}'=28kPa.Using unit weight of 19.8kN/m^3, we compute α=821 for the sand materials. Values of G_{max} and V_s for all sand layers are then computed using Eq. (2.5) with the results shown in Figure 2.8. Using the profiles in Fig. 2.8, the values of V_{s30} and site period are 126m/s and 0.95s for AHA02.

The profiles in Figure 2.8 were tested by comparing their implied theoretical travel times from the base of the model container to each sensor position to those measured when the base of the model container was shaken with a high frequency (500 Hz model scale) low amplitude harmonic motion. The high frequency motion was selected to improve resolution in travel time measurements. Reasonable agreement was observed in a least-squares sense (details in Afacan et al. 2011), and the measured travel time values were within 10% of those predicted by Eq. (2.4). Example data resulting from this method are presented in Figure 2.11. This method is less precise than the bender element method since the wavelengths are longer, but it provides measurements at all depths in the model rather than just in one lift. The bender element data and the high frequency sine wave data were combined and used to regress parameters for the shear wave velocity profile using a common functional form.

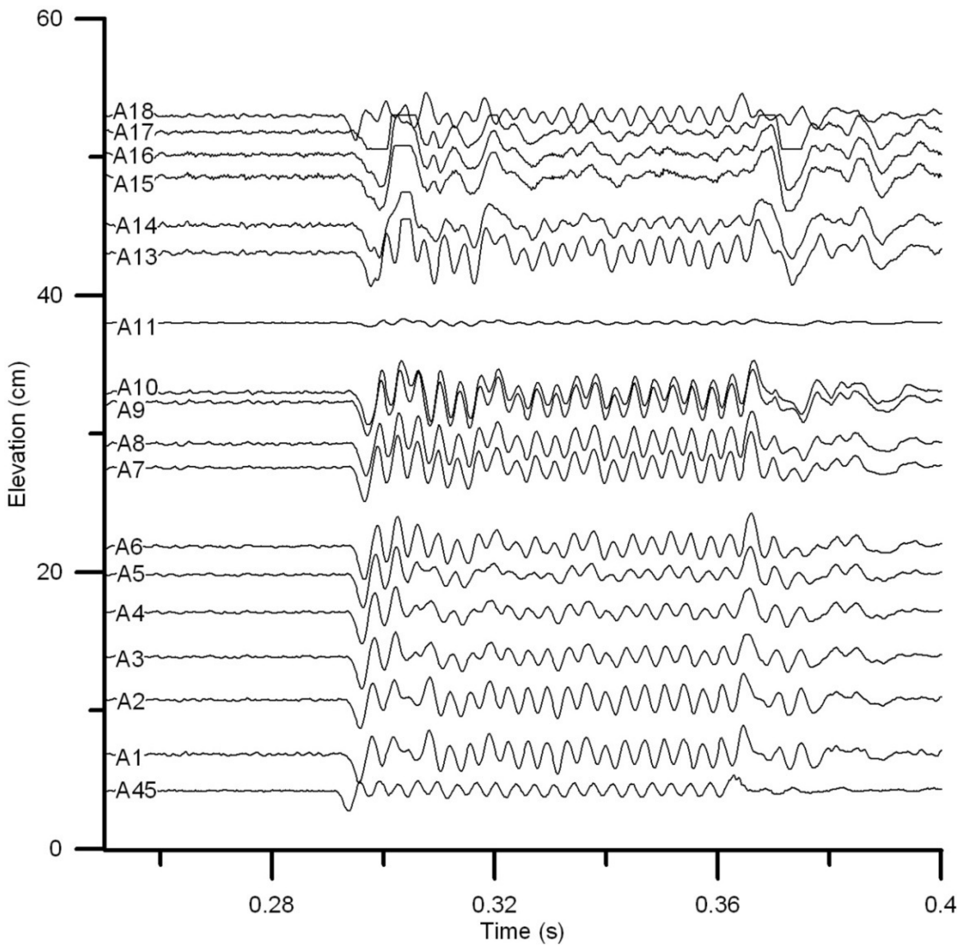

Figure 2.11 Data recorded for 500 Hz sine wave for an example sine event

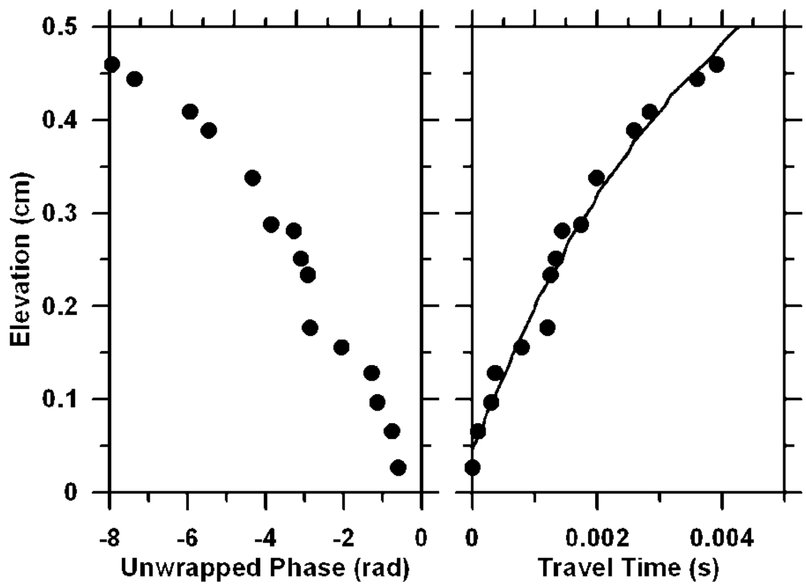

Figure 2.12 Profiles of unwrapped phase and travel time computed from high frequency sine waves shown in Figure 10 (solid circles), and travel time profile obtained from Eqs. (2.3) and (2.4).

The shear strength of the clay was measured using a small hand vane device following spin-down of the centrifuge, with the results in Figure 2.8 The measured shear strengths are potentially biased relative to those in effect under "in flight" conditions as a result of reduced effective stresses due to swelling of the clay during the gradual spin-down of the centrifuge which requires about 20 minutes. Changes in pore pressure due to swelling were observed in PPT readings in the overconsolidated clay layers. The in-flight shear strengths in Figure 2.8 were derived from strength normalization concepts (e.g., Ladd 1991):

$$\frac{S_u}{\sigma'_{vc}} = 0.22 \times OCR^{0.8} \tag{2.6}$$

where 0.22 is the undrained strength ratio of the same bay mud material measured in direct simple shear tests by Park (2011), and 0.8 = 0.88(1-C_r/C_c) is the recommended exponent from Ladd (1991) for homogenous sedimentary clays of low to moderate sensitivity. As shown in

Figure 2.8, this relation produces good agreement with measured vane shear strengths in low-OCR layers relatively unaffected by swelling during spin-down. Vane shear strengths in the deeper more heavily overconsolidated layers were lower than predicted in Eq. (2.6), which is likely due to a decrease in effective stress due to more rapid consolidation of these stiff layers during spin-down.

2.6 BASE MOTION SEQUENCE

The base of the model container was shaken by a sequence of ground motions that included

(i) scaled versions of earthquake recordings,

(ii) small amplitude sine sweeps for the purpose of identifying the small-strain properties of the soil model, and

(iii) small amplitude sine waves having approximately 20 cycles.

A total of 24 shaking events were applied to the base of model AHA02. The sequence of motions is shown in Table 2.10. Most of the ground motions used in this study were scaled versions of earthquake recordings. The selected ground motions are listed in Table 2.11, and response spectra are plotted in Figure 2.13.

Table 2.10 Motion Sequence

Event ID	Name of Motion	Time	Date	Shake Data	Amp	PCB Gain	Freq. (Hz)	CGL
Spin Up	-	5:30	3/18/2010	-	-	-	-	-
Consolidation	-	5:30 - 12:30	3/18/2010	-	-	-	-	-
AHA02-S1	Step	12:35	3/18/2010	03182010@053538@123550@78.3rpm	0.7	10	-	CGL_1
AHA02-S2	Sine Wave	12:55	3/18/2010	03182010@053538@125549@78.3rpm	0.3	10	500	CGL_1
AHA02-S3	SineSweep.shk	1:10	3/18/2010	03182010@053538@130923@78.2rpm	1	10	-	CGL_1
AHA02-S4	SineSweep.shk	1:30	3/18/2010	03182010@053538@132837@78.2rpm	5	10	-	CGL_1
AHA02-S5	NIS000_Command5.prn	2:10	3/18/2010	03182010@053538@141104@78.1rpm	1	10	-	CGL_1
AHA02-S6	SCS052_123_it3.shk	14:30	3/18/2010	03182010@053538@143130@78.3rpm	0.1	10	-	CGL_1
AHA02-S7	PRI090_it3.shk	14:47	3/18/2010	03182010@053538@144701@78.2rpm	0.1	1	-	CGL_0
AHA02-S8	RRS228_it3.shk	3:09	3/18/2010	03182010@053538@150852@78.4rpm	0.1	1	-	CGL_0
AHA02-S9	WPI046_it3.shk	3:19	3/18/2010	03182010@053538@152017@78.4rpm	0.1	1	-	CGL_0
AHA02-S10	LGPC090_it3.shk	3:29	3/18/2010	03182010@053538@152936@77.8rpm	0.1	1	-	CGL_0
AHA02-S11	NIS000_Command5.prn	3:39	3/18/2010	03182010@053538@153857@77.6rpm	6	1	-	CGL_0
AHA02-S12	SCS052_123_it3.shk	3:47	3/18/2010	03182010@053538@154946@77.2rpm	0.5	1	-	CGL_0
AHA02-S13	PRI090_it3.shk	4:05	3/18/2010	03182010@053538@160510@77.3rpm	0.3	1	-	CGL_0
AHA02-S14	RRS228_it3.shk	4:12	3/18/2010	03182010@053538@161240@77.6rpm	0.3	1	-	CGL_0
AHA02-S15	WPI046_it3.shk	4:18	3/18/2010	03182010@053538@161845@77.7rpm	0.3	1	-	CGL_0
AHA02-S16	LGPC090_it3.shk	4:24	3/18/2010	03182010@053538@162600@77.2rpm	0.3	1	-	CGL_0
AHA02-S17	NIS000_Command5.prn	4:34	3/18/2010	03182010@053538@163403@77.5rpm	13	1	-	CGL_0
AHA02-S18	SCS052_123_it3.shk	4:51	3/18/2010	03182010@053538@165115@77.7rpm	1	1	-	CGL_0
AHA02-S19	PRI090_it3.shk	5:31	3/18/2010	03182010@053538@173148@77.9rpm	1	1	-	CGL_0
AHA02-S20	RRS228_it3.shk	5:53	3/18/2010	03182010@053538@175314@77.6rpm	1	1	-	CGL_0
AHA02-S21	WPI046_it3.shk	6:08	3/18/2010	03182010@053538@180808@77.8rpm	1	1	-	CGL_0
AHA02-S22	LGPC090_it3.shk	6:20	3/18/2010	03182010@053538@182151@77.9rpm	1	1	-	CGL_0
AHA02-S23	Sine Wave	6:32	3/18/2010	03182010@053538@183434@77.5rpm	0.3	10	-	CGL_1
AHA02-S24	Kobe0807.shk	6:40	3/18/2010	03182010@053538@184308@77.5rpm	7	1	-	CGL_0
Spin Down	-		3/18/2010	-	-	-	-	-

The digital ground motion records and the metadata were obtained from the PEER-NGA ground motion database (Chiou et al, 2008), and subsequently conditioned for use on the centrifuge. The selected motions cover a range of site conditions likely to exist beneath soft clay deposits (V_{s30} = 198 to 705 m/s), and to cover a range of magnitudes that contribute significantly to seismic hazard in many seismically active crustal regions. Furthermore, the peaks in the response spectra range from approximately 0.3s to 2s, which straddles the site period. In some cases, multiple scaled versions of the same ground motion were imposed on the model to observe effects of amplitude for the same motion, while in other cases a large amplitude motion was only applied once to mobilize large shear strains in the model. Excess pore pressures mobilized in the clay layers during shaking were small, and sufficient time was permitted between each sequential shake to permit these small excess pore pressures to dissipate.

Table 2.11 Characteristics of recorded earthquake ground motions adapted in this study

Motion	Earthquake	Station	Mw	R_{jb} (km)	Vs_{30} (m/s)	PGA (g)	PGV (cm/s)	PGD (cm)
CYC160	1979 Coyote Lake	Coyote Lake Dam (SW abutment)	5.7	5.3	597	0.218	15.09	1.84
HEC000	1999 Hector Mine	Hector	7.1	10.4	685	0.306	34.21	17.71
NIS000	1995 Kobe Nishi-Akashi	Nishi-Akashi	6.9	7.1	609	0.486	35.73	10.75
TCU045	1999 Chi Chi	TCU045	7.6	26	705	0.473	38.89	25.52
PRI090	1995 Kobe	Port Island (0m)	6.9	3.31	198	0.278	54.2	24.72
RRS228	1994 Northridge	Rinaldi Receiving Station	6.7	0	282	0.634	109.24	28.26
WPI046	1994 Northridge	Newhall W Pico Canyon. Rd.	6.7	2.11	286	0.385	79.07	30.21
LGPC090	1989 Loma Prieta	LGPC	6.9	0	478	0.784	77.15	42.67
SCS052	1994 Northridge	74 Sylmar - Converter	6.7	5.4	251	0.75	109.4	45.8

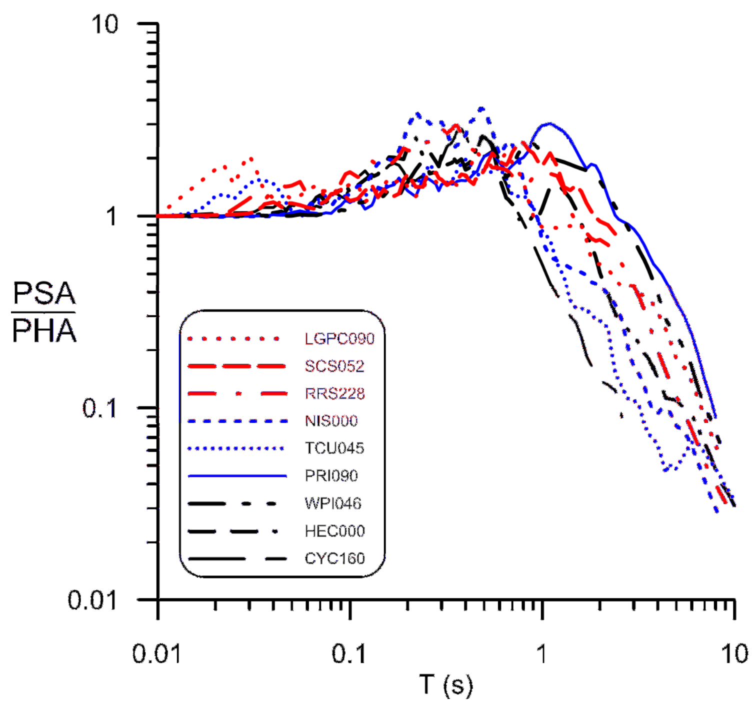

Figure 2.13 Response spectra of the ground motions used in this study

Figure 2.14 shows the peak horizontal acceleration recorded in the soil near the base of the centrifuge models (PHA_b) and recorded at the position of the shallowest accelerometer

(PHA_0). We generally see amplification for $PHA_b \leq 0.2$g and de-amplification for $PHA_b \geq 0.3$g, with mixed results at intermediate amplitudes. These varying levels of site amplification indicate nonlinearity.

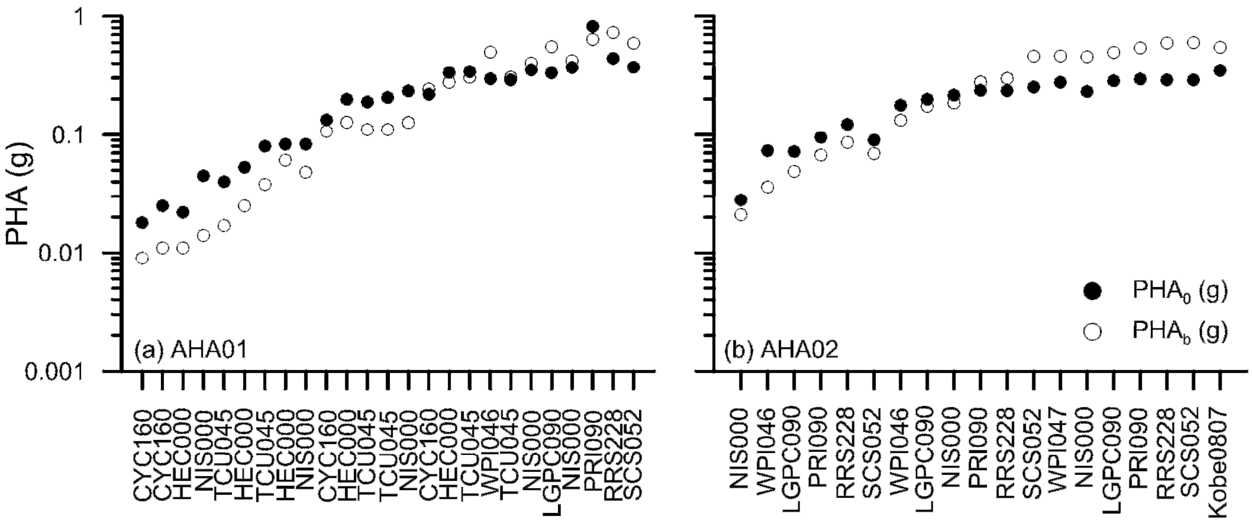

Figure 2.14 Peak base acceleration PHA_b and surface acceleration PHA_0 recorded in centrifuge models for test involving earthquake ground motion excitation

The centrifuge shaking table is able to replicate key features of the earthquake motions, although some differences arise from imperfections in the feedback control loop, particularly at high frequencies. Therefore, the recorded base motions should always be used in lieu of the command motions when analyzing the model response. Some of the motions utilized herein were conditioned for use on the centrifuge prior to the present work by Mason et al. (2010). Furthermore, the motions on the base plate of the model container are different from the motions within the soil near the base of the model container. This is likely caused by slip between the latex membrane and container base. For this reason, we herein interpret the most deeply embedded ground motion recording as being representative of the base motion.

2.7 DYNAMIC TEST DATA

A sequence of 24 ground motions was imposed on the centrifuge models, and the accelerometers, pore pressure transducers, and linear potentiometers were sampled at a frequency of approximately 4096 Hz during each event. Table 2.10 summarizes the sequence of motions imposed on the models. The ground motions were calibrated for use on the centrifuge by Mason et al. (2010). The raw data recorded during each motion was saved in a binary bit format. The data were converted to ASCII text files in prototype engineering units using a custom Lab View program. The unprocessed binary data files can be found in NEEShub under the appropriate Experiment, Trial and Repetition in the Unprocessed_Data folder, and the processed ASCII files can be found in NEEShub as Converted_Data. An executable version of the LabView program used to convert the data is also included on NEEShub. The program requests as input a raw data file and a channel gain list text file for the conversion. Two different channel gain list files were used to process the data (Table 2.10), and are also uploaded to NEEShub. The steps used to process the data are (a) truncation of recorded data, (b) sorting of data columns, and (c) offset and calibration. The details of each procedure are discussed below.

a. Truncation of recorded data

Each motion lasted for less than one second, but about 10 seconds of data was recorded to ensure that the shaking was captured. To reduce file size, about one second of the data was desired. The LabView is used to convert the data to prototype units that permit truncation of the beginning and end portions of the data to save only the desired portion in the ASCII files. Typically, 4096 data points were saved to the ASCII files. The motivation for storing 2^N data points is to facilitate easy frequency domain analysis using the fast Fourier transform.

Screenshots in Figure 2.15 and Figure 2.16 show how the truncation was performed for motion AHA02-S1.

b. Sorting of data columns

The order in which the data columns were saved in the raw binary files corresponded to the amplifier channels to which each sensor was connected, which did not correspond to the sensor numbering scheme adopted in Tables 2.3 and 2.4. Hence, the data columns were sorted such that the first column contains the time vector, the next 48 columns contain accelerometers A1-A48, the next 13 columns contain pore pressure transducers P1-P13, and the final 11 columns contain linear potentiometers L1-L11.

c. Offset and Calibration

The sorted data were converted to the engineering units from the recorded voltage values by applying the calibration factors summarized in the channel gain list. Instruments were calibrated before and after the test to verify the consistency of the calibration factors. The recorded data was adjusted to follow the sign conventions established for measuring model coordinates. The sign conventions were set to the global coordinate system; horizontal motion is positive from north to south, vertical motion is positive downward.

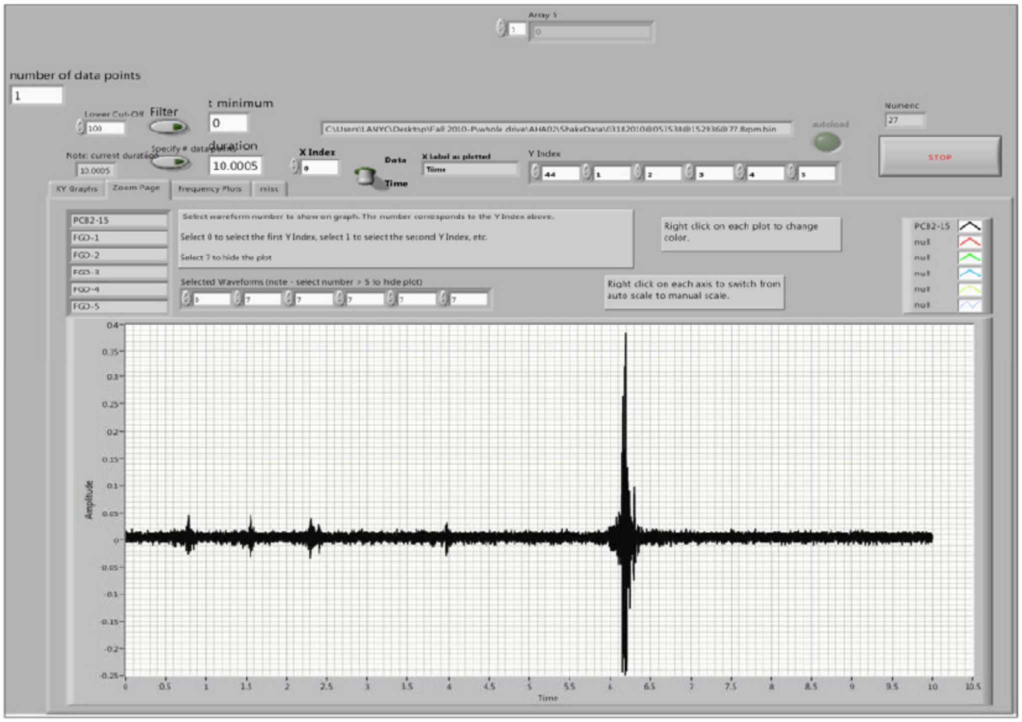

Figure 2.15 Screenshot of LabView processing for motion AHA02-S1 showing the raw data without truncation with duration of over 12 seconds.

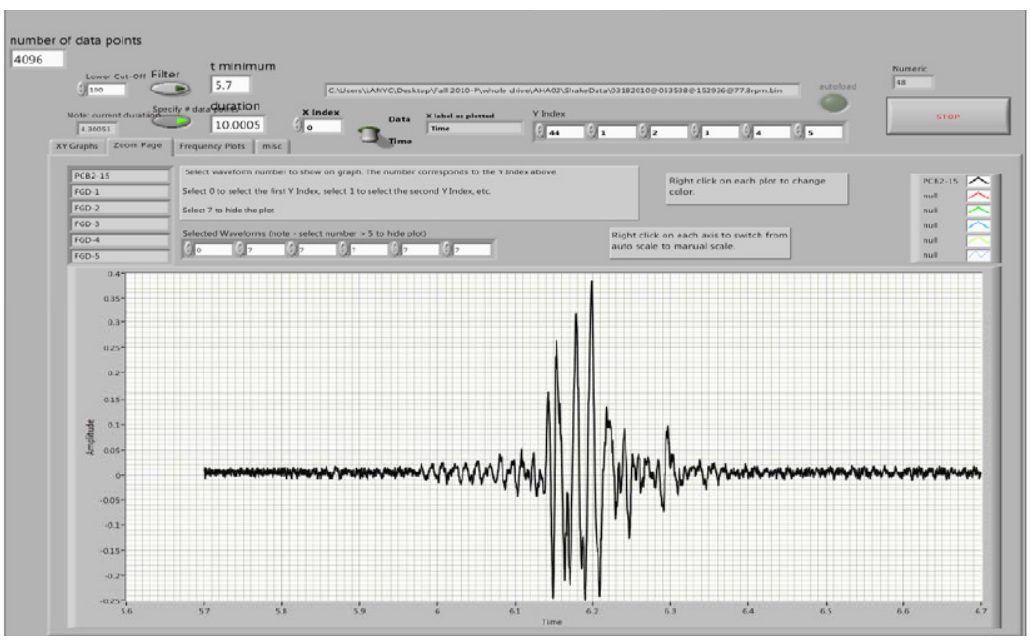

Figure 2.16 Screenshot of the truncated motion between 5.7 and 6.7 seconds.

Offsets were also applied to the recorded data to represent a logical physical starting point since voltage zero does not always correspond to physical zero. The average value of each acceleration record was subtracted from the acceleration vector so that the average acceleration is zero for every record. The acceleration records were not filtered or baseline corrected, and therefore cannot be directly integrated in time to obtain reasonable velocity or displacement records due to the unavoidable presence of low frequency noise. The pore pressure transducers were adjusted such that zero would correspond to zero gauge pressure. The offset value for each pore pressure transducer was obtained by computing the slope of the pore pressure voltage versus centrifugal acceleration as the centrifuge spun up, and taking the intercept at a centrifugal acceleration of zero. These values were slightly smaller than the voltages at 1-g since the water table generates some small hydrostatic pressures in the model. The initial value from the beginning of the very first ground motion was subtracted from all of the linear potentiometer recordings such that displacements are measured with respect to the undeformed geometry of the model container at the time the first shaking event was applied. The truncated, sorted, converted, offset data vectors were written to ASCII text files.

Example data are shown in Figures 2.17, 2.18 and 2.19 for selected sensors.

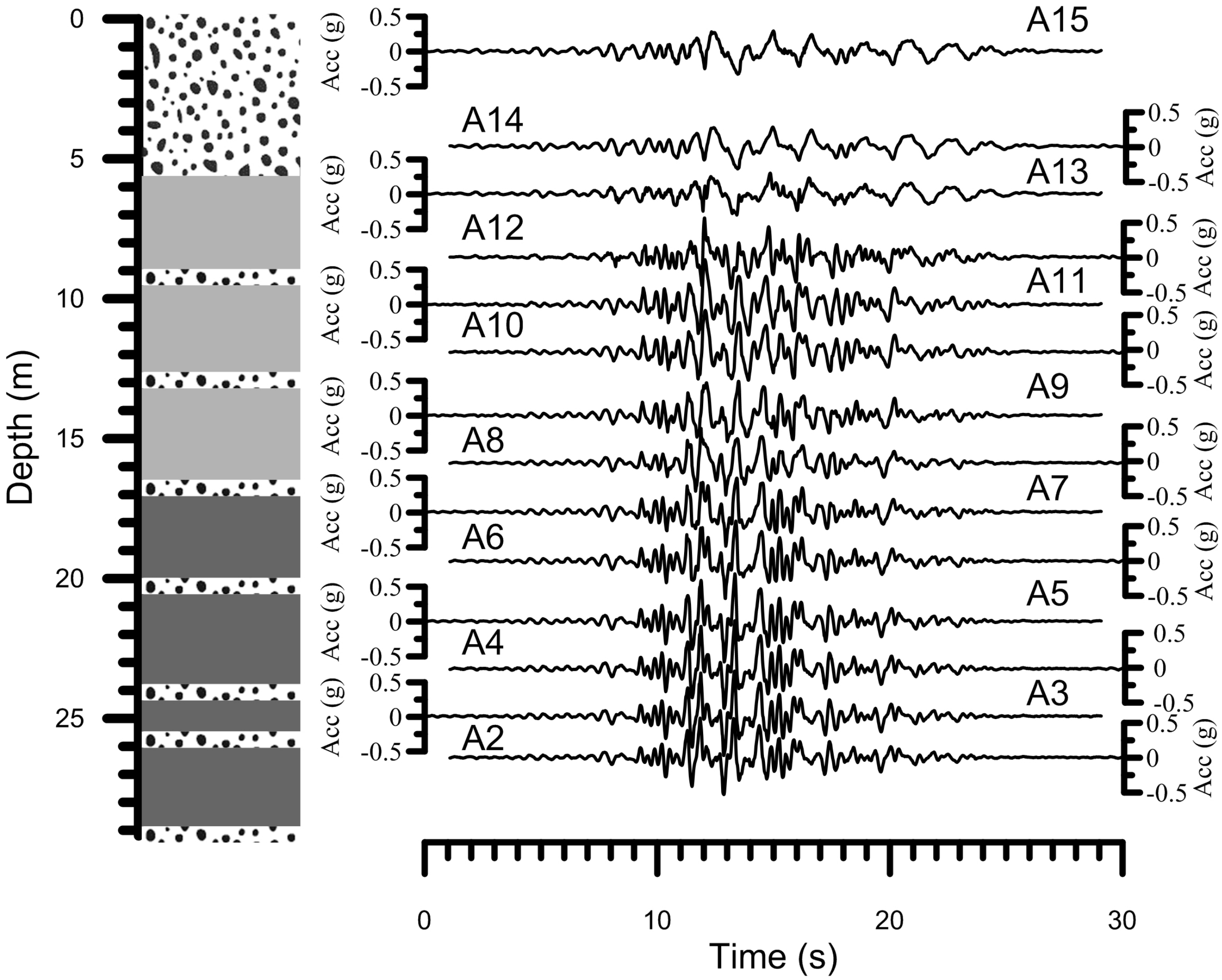

Figure 2.17 Acceleration time series for motion LGPC090

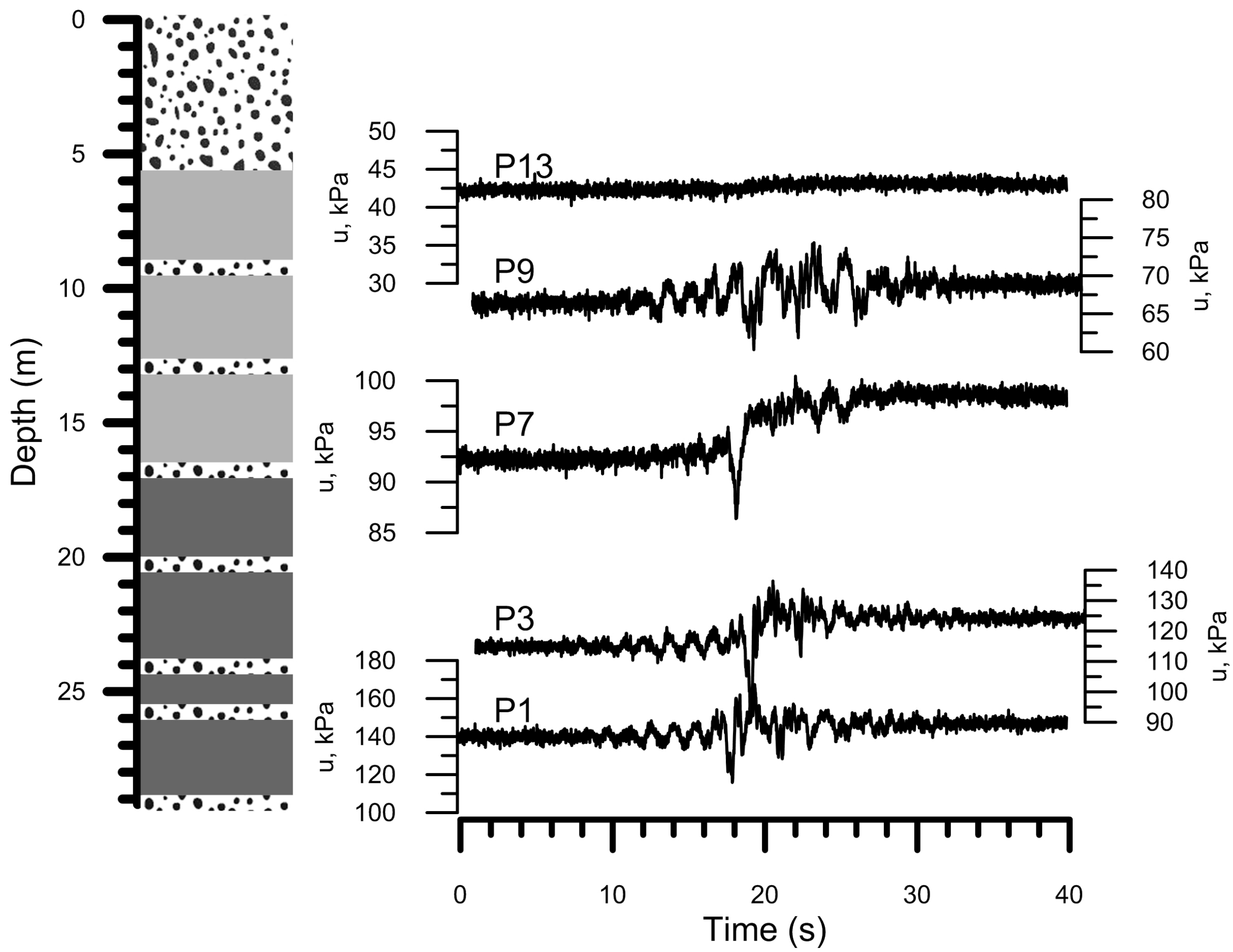

Figure 2.18 Pore pressure time series for motion LGPC090

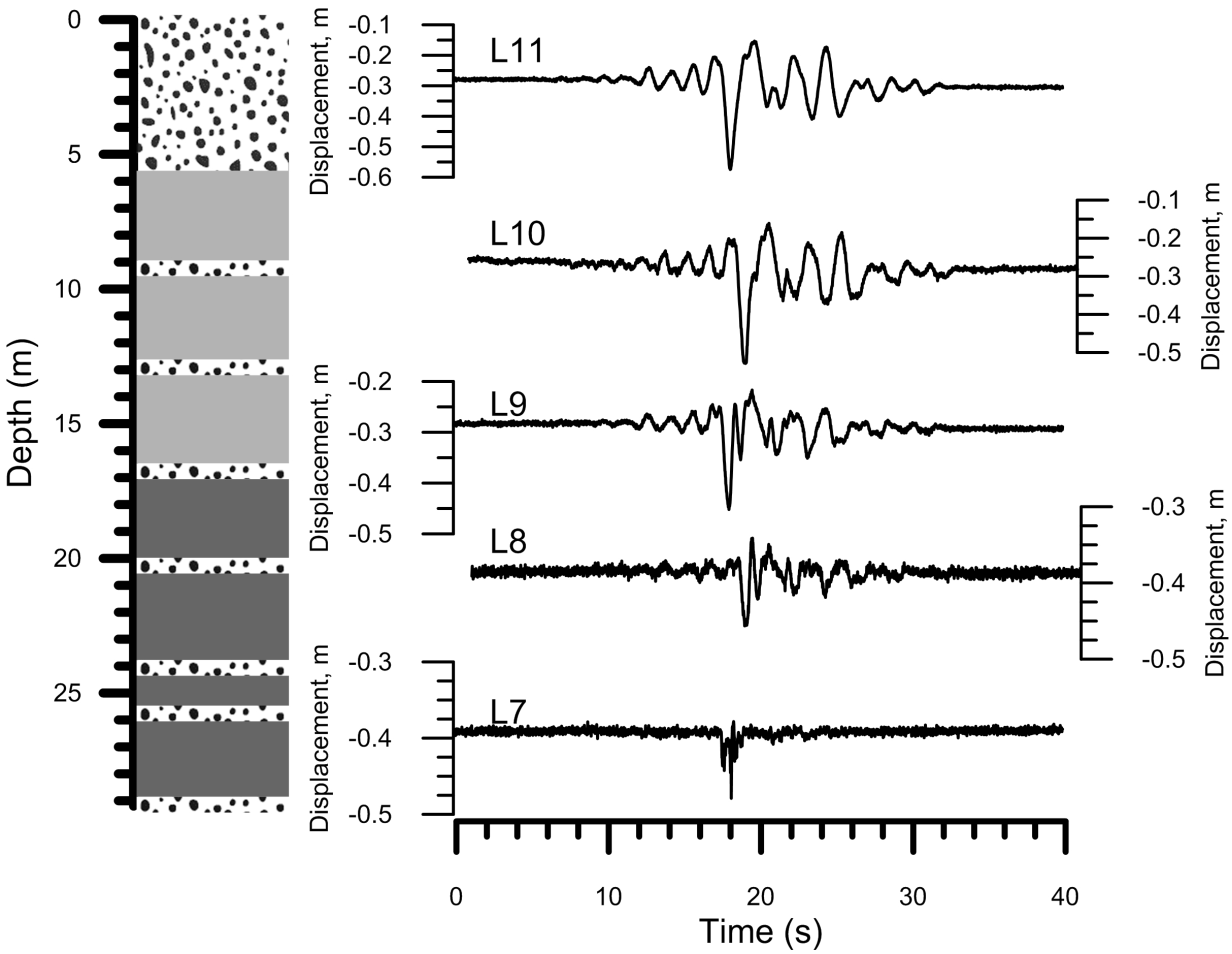

Figure 2.19 Displacement time series of linear potentiometers for motion LGPC090

2.8 KNOWN LIMITATIONS OF THE RECORDED DATA

Sensor malfunction is an unfortunate part of centrifuge testing that is fairly common due to the difficulty environment in the high g-field. Table 2.12 indicates sensors that functioned properly (shaded green) and those that malfunctioned (shaded red). The causes of sensor malfunction were often not known, but typical indications of sensor malfunction include a ±5V constant signal that is insensitive to physical stimulus.

Table 2.12 List of sensors that functioned properly and malfunctioned during AHA02

Sensor ID	Serial Number	Amp Channel ID	Step	Sine Wave	SineSweep.shk	SineSweep.shk	NIS000_Command5.prn	SCS052_123_it3.shk	PRI090_it3.shk	RRS228_it3.shk	WPI046_it3.shk	LGPC090_it3.shk	NIS000_Command5.prn	SCS052_123_it3.shk	PRI090_it3.shk	RRS228_it3.shk	WPI046_it3.shk	LGPC090_it3.shk	NIS000_Command5.prn	SCS052_123_it3.shk	PRI090_it3.shk	RRS228_it3.shk	WPI046_it3.shk	LGPC090_it3.shk	Sine Wave	Kobe0807.shk
A1	99514	PCB1-1	B	B	B	B	B	B	B	B	B	B	B	B	B	B	B	B	B	B	B	B	B	B	B	B
A2	73964	PCB1-2	B	B	B	G	B	G	G	G	G	G	G	G	G	G	G	G	G	G	G	G	G	G	G	G
A3	5604	PCB1-5	G	G	G	G	G	G	G	G	G	G	G	G	G	G	G	G	G	G	G	G	G	G	G	G
A4	99516	PCB1-8	G	G	G	G	G	G	G	G	G	G	G	G	G	G	G	G	G	G	G	G	G	G	G	G
A5	99518	PCB1-9	G	G	G	G	G	G	G	G	G	G	G	G	G	G	G	G	G	G	G	G	G	G	G	G
A6	5607	PCB1-12	G	G	G	G	G	G	G	G	G	G	G	G	G	G	G	G	G	G	G	G	G	G	G	G
A7	99512	PCB1-13	G	G	G	G	G	G	G	G	G	G	G	G	G	G	G	G	G	G	G	G	G	G	G	G
A8	99517	PCB1-14	G	G	G	G	G	G	G	G	G	G	G	G	G	G	G	G	G	G	G	G	G	G	G	G
A9	73959	PCB2-1	G	G	G	G	G	G	G	G	G	G	G	G	G	G	G	G	G	G	G	G	G	G	G	G
A10	21044	PCB2-6	G	G	G	G	G	G	G	G	G	G	G	G	G	G	G	G	G	G	G	G	G	G	G	G
A11	21067	PCB2-7	G	G	G	G	G	G	G	G	G	G	G	G	G	G	G	G	G	G	G	G	G	G	G	G
A12	97115	PCB2-12	G	G	G	G	G	G	G	G	G	G	G	G	G	G	G	G	G	G	G	G	G	G	G	G
A13	96936	PCB2-13	G	G	G	G	G	G	G	G	G	G	G	G	G	G	G	G	G	G	G	G	G	G	G	G
A14	97116	PCB3-2	G	G	G	G	G	G	G	G	G	G	G	G	G	G	G	G	G	G	G	G	G	G	G	G
A15	96939	PCB3-3	G	G	G	G	G	G	G	G	G	G	G	G	G	G	G	G	G	G	G	G	G	G	G	G
A16	21323	PCB1-3	G	G	G	G	G	G	G	G	G	G	G	G	G	G	G	G	G	G	G	G	G	G	G	G
A17	21056	PCB1-6	G	G	G	G	G	G	G	G	G	G	G	G	G	G	G	G	G	G	G	G	G	G	G	G
A18	21051	PCB1-10	B	B	B	B	B	B	B	B	B	B	B	B	B	B	B	B	B	B	B	B	B	B	B	B
A19	99517	PCB1-14	G	G	G	G	G	G	G	G	G	G	G	G	G	G	G	G	G	G	G	G	G	G	G	G
A20	21071	PCB2-2	G	G	G	G	G	G	G	G	G	G	G	G	G	G	G	G	G	G	G	G	G	G	G	G
A21	3962	PCB2-8	G	G	G	G	G	G	G	G	G	G	G	G	G	G	G	G	G	G	G	G	G	G	G	G
A22	3162	PCB2-14	G	G	G	G	G	G	G	G	G	G	G	G	G	G	G	G	G	G	G	G	G	G	G	G
A23	4596	PCB3-4	G	G	G	G	G	G	G	G	G	G	G	G	G	G	G	G	G	G	G	G	G	G	G	G
A24	21070	PCB1-4	G	G	G	G	G	G	G	G	G	G	G	G	B	B	B	B	G	B	B	B	B	B	G	B
A25	73962	PCB1-7	G	G	G	G	G	G	G	G	G	G	G	G	G	G	G	G	G	G	G	G	G	G	G	G
A26	21048	PCB1-11	G	G	G	G	G	G	G	G	G	G	G	G	G	G	G	G	G	G	G	G	G	G	G	G
A27	5602	PCB1-15	G	G	G	G	G	G	G	G	G	G	G	G	G	G	G	G	G	G	G	G	G	G	G	G
A28	21061	PCB2-3	G	G	G	G	G	G	G	G	G	G	G	G	G	G	G	G	G	G	G	G	G	G	G	G
A29	96935	PCB2-9	G	G	G	G	G	G	G	G	G	G	G	G	G	G	G	G	G	G	G	G	G	G	G	G
A30	97114	PCB2-15	G	G	G	G	G	G	G	G	G	G	G	G	G	G	G	G	G	G	G	G	G	G	G	G
A31	3203	PCB3-5	B	B	B	G	G	G	G	G	G	G	G	G	G	G	G	G	G	G	G	G	G	G	G	G
A32	21046	PCB2-5	G	G	G	B	B	G	G	G	G	G	G	G	G	G	G	G	G	G	G	G	G	G	G	G
A33	3955	PCB2-11	G	G	G	G	G	G	G	G	G	G	G	G	G	G	G	G	G	G	G	G	G	G	G	G
A34	5276	PCB3-1	G	G	G	G	G	G	G	G	G	G	G	G	G	G	G	G	G	G	G	G	G	G	G	G
A35	5272	PCB3-7	G	G	G	G	G	G	G	G	G	G	G	G	G	G	G	G	G	G	G	G	G	G	G	G
A36	21319	PCB2-4	G	G	G	B	G	G	G	G	G	G	G	G	G	G	G	G	G	G	G	G	G	G	G	G
A37	3157	PCB2-10	G	G	G	G	G	G	G	G	G	G	G	G	G	G	G	G	G	G	G	G	G	G	G	G
A38	5270	PCB2-16	B	B	B	B	B	B	B	B	B	B	B	B	B	B	B	B	B	B	B	B	B	B	B	B
A39	5274	PCB3-6	G	G	G	G	G	G	G	G	G	G	G	G	G	G	G	G	G	G	G	G	G	G	G	G
A40	6023	PCB3-13	G	B	B	G	G	G	G	G	G	G	G	G	G	G	G	G	G	G	G	G	G	G	G	G
A41	6025	PCB3-14	G	B	B	G	G	G	G	G	G	G	G	G	G	G	G	G	G	G	G	G	G	G	G	G
A42	6022	PCB3-12	G	G	G	G	G	G	G	G	G	G	G	G	G	G	G	G	G	G	G	G	G	G	G	G
A43	6016	PCB3-11	G	G	G	G	G	G	G	G	G	G	G	G	G	G	G	G	G	G	G	G	G	G	G	G
A44	6019	PCB3-10	G	G	G	G	G	G	G	G	G	G	G	G	G	G	G	G	G	G	G	G	G	G	G	G
A45	6018	PCB3-9	G	G	G	G	G	G	G	G	G	G	G	G	G	G	G	G	G	G	G	G	G	G	G	G
A46	6015	PCB3-8	G	G	G	G	G	G	G	G	G	G	G	G	G	G	G	G	G	G	G	G	G	G	G	G
A47	107068	PCB3-15	G	G	G	G	G	G	G	G	G	G	G	G	G	G	G	G	G	G	G	G	G	G	G	G
A48	107066	PCB3-16	G	G	G	G	G	G	G	G	G	G	G	G	G	G	G	G	G	G	G	G	G	G	G	G

P1	11158	FGD-1	G	G	G	G	G	G	G	G	G	G	G	G	G	G	G	G	G	G	G	G	G	G	G	G
P2	11821	FGD-12	5	-5	-5	-5	5	5	5	5	5	5	5	5	5	5	5	5	5	5	5	5	5	5	5	5
P3	11827	FGD-0	G	G	G	G	G	G	G	G	G	B	B	B	B	G	G	G	G	B	B	B	G	G	G	G
P4	12050	FGD-6	G	G	G	G	G	G	G	G	G	G	G	G	G	G	G	G	G	G	G	G	G	G	G	G
P5	11149	FGD-2	G	G	G	G	G	G	G	G	G	G	G	G	G	G	G	G	G	G	G	G	G	G	G	G
P6	11830	FGD-7	G	G	G	G	G	G	G	G	G	G	G	G	G	G	G	G	G	G	G	G	G	G	G	G
P7	2963400	FGD-3	G	G	G	G	G	G	G	G	G	G	G	G	G	G	G	G	G	G	G	G	G	G	B	G
P8	11822	FGD-14	5	5	5	5	5	5	5	5	5	5	5	5	5	5	5	5	5	B	B	B	B	B	5	B
P9	11139	FGD-4	G	G	G	G	G	G	G	G	G	G	G	B	G	G	G	G	G	B	B	B	G	G	G	B
P10	2963406	FGD-15	G	G	G	G	G	G	G	G	G	G	G	B	G	B	G	G	G	B	B	B	G	G	G	G
P11	2973226	FGD-5	G	G	G	G	G	G	G	G	G	G	G	G	G	G	G	G	G	G	G	G	G	G	G	G
P12	11760	FGD-17	G	G	G	G	G	G	G	G	G	G	G	G	G	G	G	G	G	G	G	G	G	G	G	G
P13	11141	FGD-13	G	G	G	G	G	G	G	G	G	G	G	G	G	G	G	G	G	G	G	G	G	G	G	G
L1	434	PT0	G	G	G	G	G	G	G	G	G	G	G	G	B	G	G	G	B	B	B	B	B	G	G	G
L2	430	PT1	G	G	G	G	G	G	G	G	G	G	G	G	G	G	G	G	G	B	B	G	B	G	G	G
L3	435	PT2	G	G	G	G	G	G	G	G	G	G	G	G	B	G	G	G	G	G	G	B	B	B	G	G
L4	303	PT3	G	G	G	G	G	G	G	G	G	G	G	G	G	G	G	G	G	G	G	G	G	G	G	G
L5	302	PT4	G	G	G	G	G	G	G	G	G	G	G	G	G	G	G	G	G	G	G	G	G	G	G	G
L6	300	PT5	G	G	G	G	G	G	G	G	G	G	G	G	G	G	G	G	G	G	G	G	G	G	G	G
L7	492	PT6	G	G	G	G	G	G	G	G	G	G	G	G	G	G	G	G	G	G	G	G	G	G	G	G
L8	431	PT7	G	G	G	G	G	G	G	G	G	G	G	G	G	G	G	G	G	G	G	G	G	G	G	G
L9	430	PT8	G	G	G	G	G	G	G	G	G	G	G	G	G	G	G	G	G	G	G	G	G	G	G	G
L10	490	PT9	G	G	G	G	G	G	G	G	G	G	G	G	G	G	G	G	G	G	G	G	G	G	G	G
L11	422	PT10	G	G	G	G	G	G	G	G	G	G	G	G	G	G	G	G	G	G	G	G	G	G	G	G

During consolidation of the centrifuge model the press plate caused a tear in the latex membrane inside the container. The tear had to be repaired to maintain the water table at the desired height, and some of the clay on the north end of the model container had to be removed to access the tear in the membrane. The clay that was cut away from the model was subsequently placed back in its original position, but the cut made in the clay did not heal fully and could have affected wave propagation near the edges of the model container. The influence of this at the center of the model container is believed to be small.

3 DATA INTERPRETATION

In this chapter, the test data discussed in Chapter 2 is interpreted to learn about the nonlinear site response behavior of model AHA02. First, noise level is investigated and high-pass filtering of the acceleration time series is explained. High-pass filtering is required to remove low-frequency noise to obtain reasonable velocity and displacement records by integration of the recorded accelerations in time. Fourier amplitude spectra of the data are presented and an example of the velocity and displacement time series that were derived from the acceleration time series is demonstrated. Second, the container performance is discussed by comparing ground motions measured at various horizontal spatial positions in the model, from the container rings to the center. Then, stress and strain curves are computed from the acceleration arrays, and stress-strain data are presented. Modulus reduction and damping behavior are computed from the stress-strain curves. The influence of strain rate is then explored. Finally, response spectra are computed from the motions and spectral amplification factors between the surface and base input motions are presented as a function of input ground motion intensity.

3.1 NOISE LEVEL

Noise in recorded signals is unavoidable. Integration of acceleration records in time to obtain velocity and displacement records is very sensitive to low-frequency noise, so signal processing is required prior to integrating. The smallest amount of signal processing possible should be performed to avoid removing desired portions of the signal. Noise in the recorded signals is explored by studying the noise during pre-event and post event recordings. As explained earlier in the chapter 2.7, every recording lasted in 10 seconds and only one second of the recording was desired. Pre-event noise was truncated from the 10 second recording before the actual motion and post event noise was extracted sometime after the actual desired motion. An example acceleration time series and corresponding noise recorded at a specific accelerometer is shown in Figure 3.1a. The Fourier amplitude spectra are presented in Figure 3.1b.

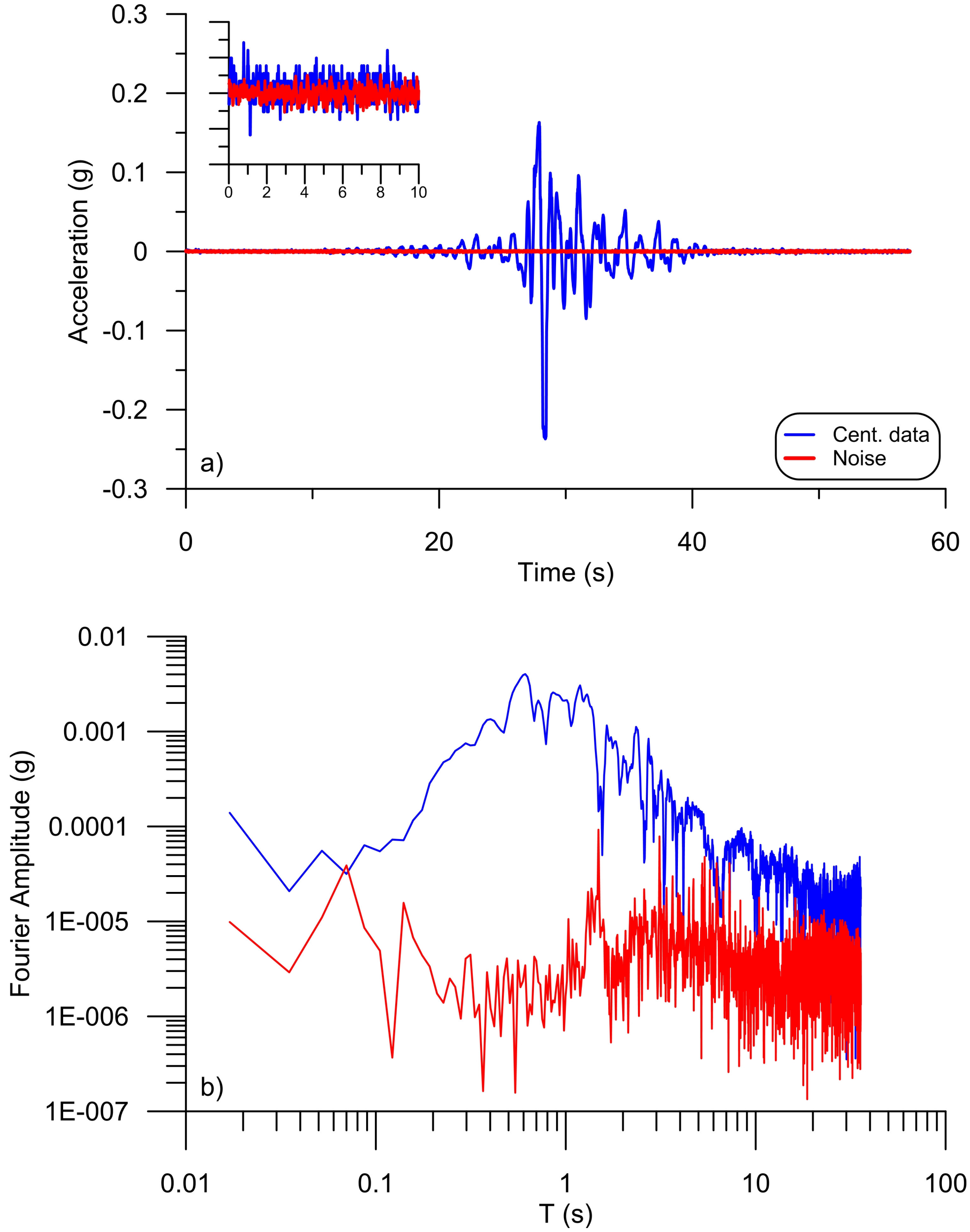

Figure 3.1 a) An example acceleration time series and noise recorded at accelerometer A15 and b) corresponding fourier amplitudes

The signal from the earthquake record exhibits significantly higher amplitude than the noise signal in the range from about 0.08 Hz to about 10 Hz. Having 48 accelerometers and 24 different motions, the maximum noise amplitude of pre-event and post event for gain 1 and gain

10, which were used to convert the raw data to engineering units, are calculated for every recording and they are plotted with their standard deviations in Figure 3.2. The max noise is calculated as 0.006g and 0.0065g for pre event and post event respectively.

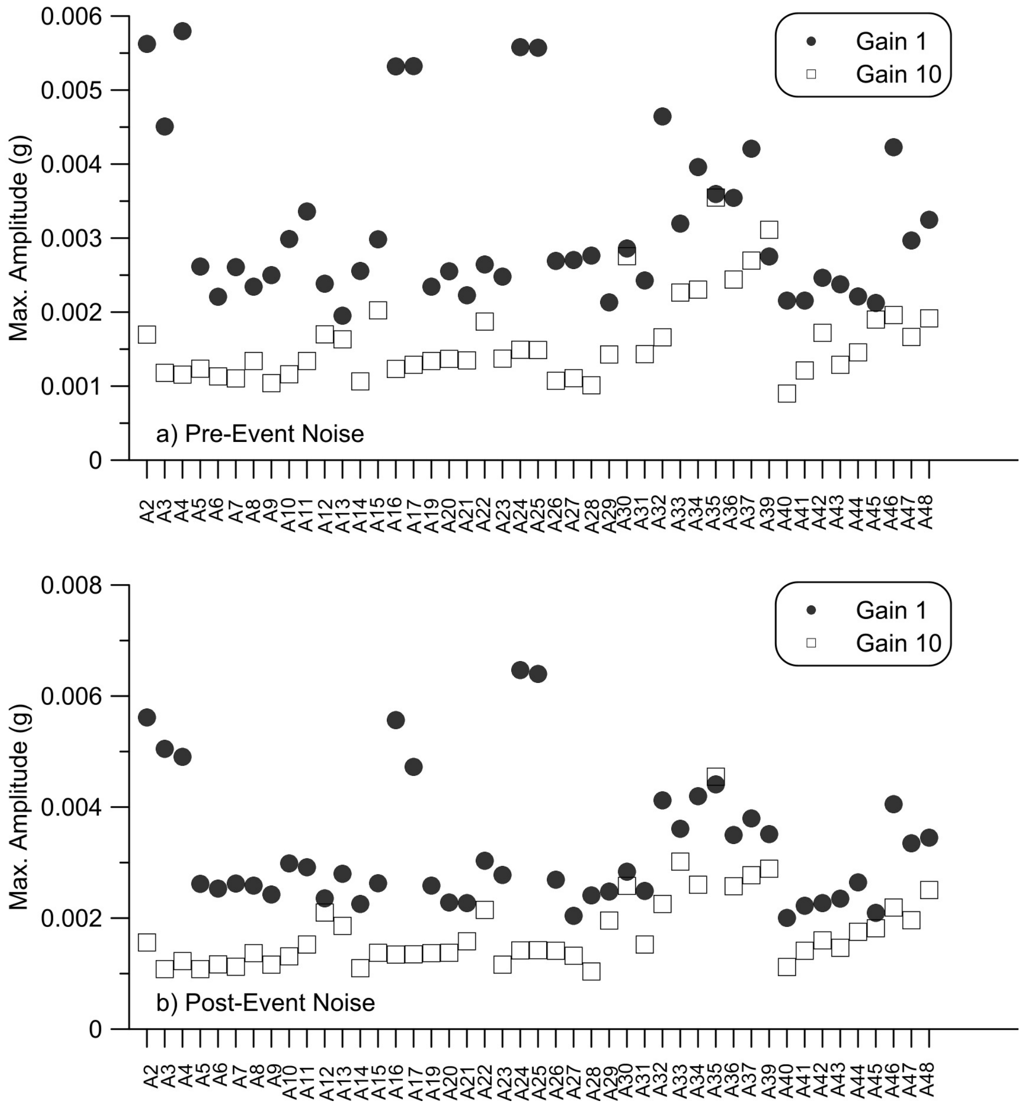

Figure 3.2 **Max noise amplitude of pre-event and post event for different accelerometers**

3.2 FILTERING THE DATA

The dynamic data were high-pass filtered before any interpretation because low-frequency noise inherent in the signals obscured the ground motions signals on low frequency bands, and accurate displacement and velocity time series cannot be derived by integration of the raw recorded data. The velocity and displacement time series are calculated by the integrating and double integrating the acceleration time series respectively. The low-frequency noise is often not readily apparent upon observation of the acceleration time series, but manifests itself as unrealistic and non-physical permanent drift in the computed velocity and displacement series.

A high pass Butterworth filter is used to remove the low-frequency noise, and is defined by Eq. (3.1).

$$G = \frac{1}{\sqrt{1+\left(\frac{f_c}{f}\right)^{2n}}} \tag{3.1}$$

In the equation shown above, f_c is defined as the cutoff frequency and n is the order of the filter. The Fourier spectrum for a ground motion is computed, and multiplied by the Butterworth filter. This process modifies the Fourier amplitude spectrum, but not the phase spectrum since the real and imaginary parts of the Fourier spectrum are both multiplied by the same scalar (i.e., the filter is acausal). The filtered time series is then recovered by applying an inverse Fourier transform.

An example Fourier amplitude spectrum is shown in Figure 3.3 for the raw data, and filtered data using the same corner frequency of f_c = 0.15Hz and filter orders of n=1 and n=5. The substantial difference between filtered and non-filtered motions occurs at low frequencies on the left side of the Fourier amplitude spectrum. Filtering the motion has the desired effect of reducing low frequency noise, but also has the undesired effect of reducing signal amplitude. Hence, it is important to adjust the filter parameters to perform the least amount of filtering necessary to provide stable integrated displacement records without removing too much of the desired portion of the signal.

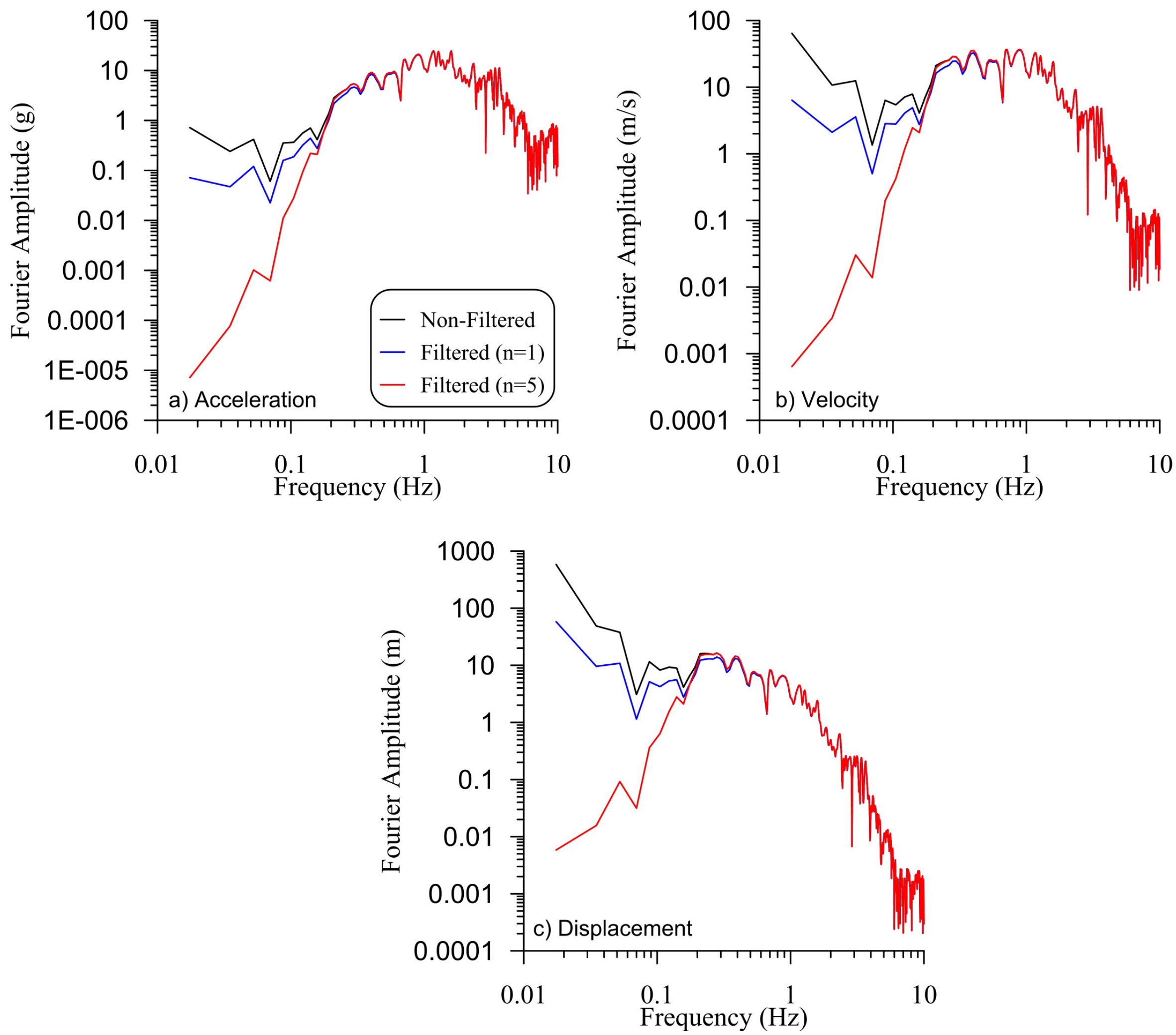

Figure 3.3 Fourier amplitudes for non-filtered and filtered data

For cases where significant low-frequency ground motion occurs (e.g., when permanent strains accrue), but is obscured by noise in the acceleration records, alternative measurement methods that accurately measure low frequencies (e.g., linear variable differential transformers) can be used to supplement the high-frequency portion of the displacement measured with the accelerometers. The LVDT data from the container rings indicate that permanent displacements were negligible for this test program, so low-frequency displacements were not added to the transient displacements obtained from the filtered acceleration records.

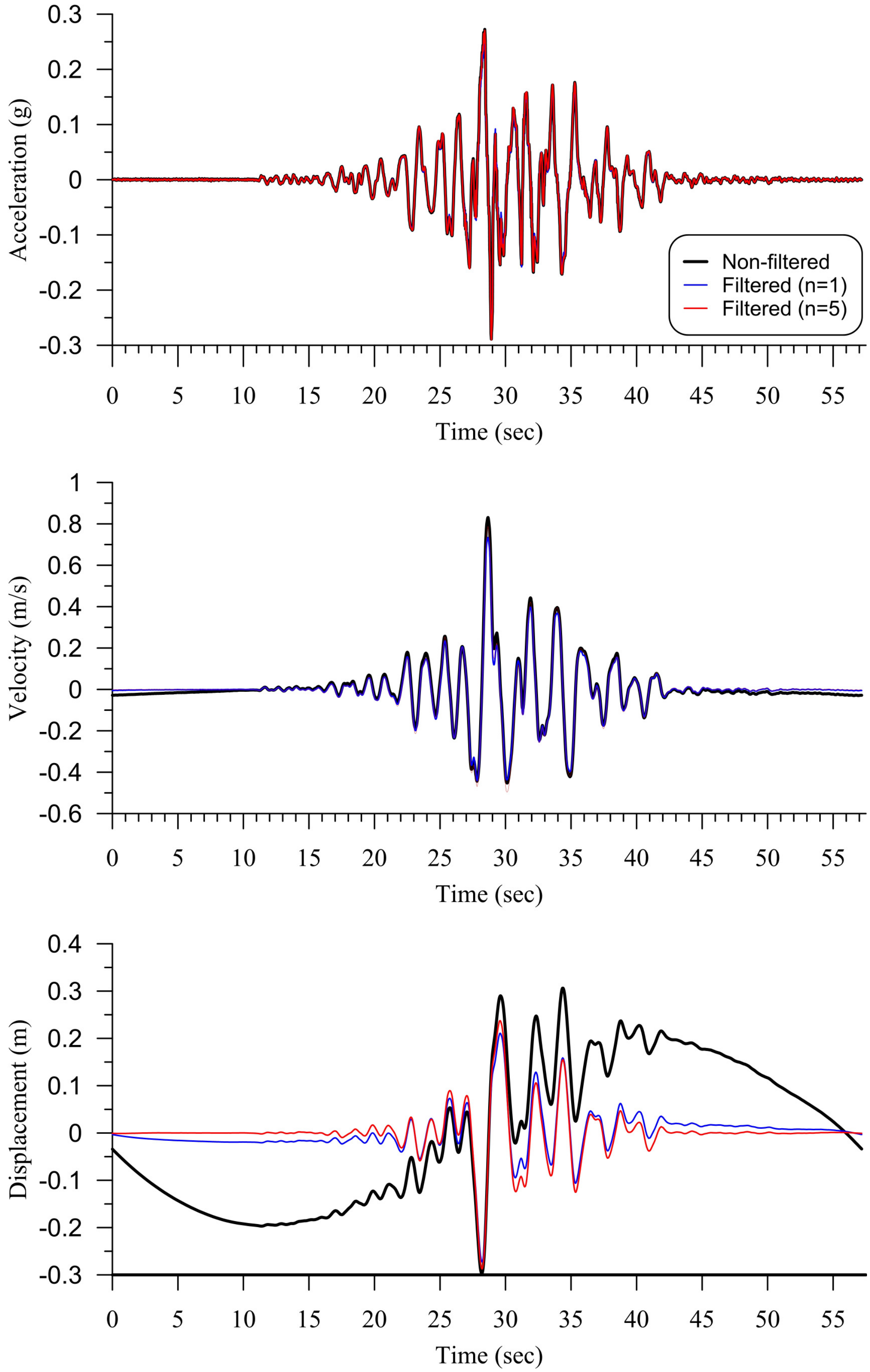

Figure 3.4 Time series for different order of filter

As seen in Figure 3.4, the filter order of 1 is too low because there is some unrealistic low-frequency drift in the displacement record. Therefore the filter of 5 is chosen to filter the data along the corner frequency of 0.15Hz.

3.3 CONTAINER PERFORMANCE

3.3.1 Container performance by comparison of the recordings

Container performance is observed by comparing ground motion records from various horizontal spatial positions at the same elevation within the model container. Sensors A20, A8, and A28 were embedded at the same elevation in lift 4, and sensor A40 was attached to the container ring at nearly the same elevation as the embedded accelerometers. Figure 3.5 shows recorded acceleration records from an input motion with peak acceleration of 0.29g. The peak accelerations recorded from these sensors are very similar. Had the container influenced the soil column, differences in these ground motions would be anticipated. Hence, the data indicate that the container performed well at reproducing one-dimensional site response conditions.

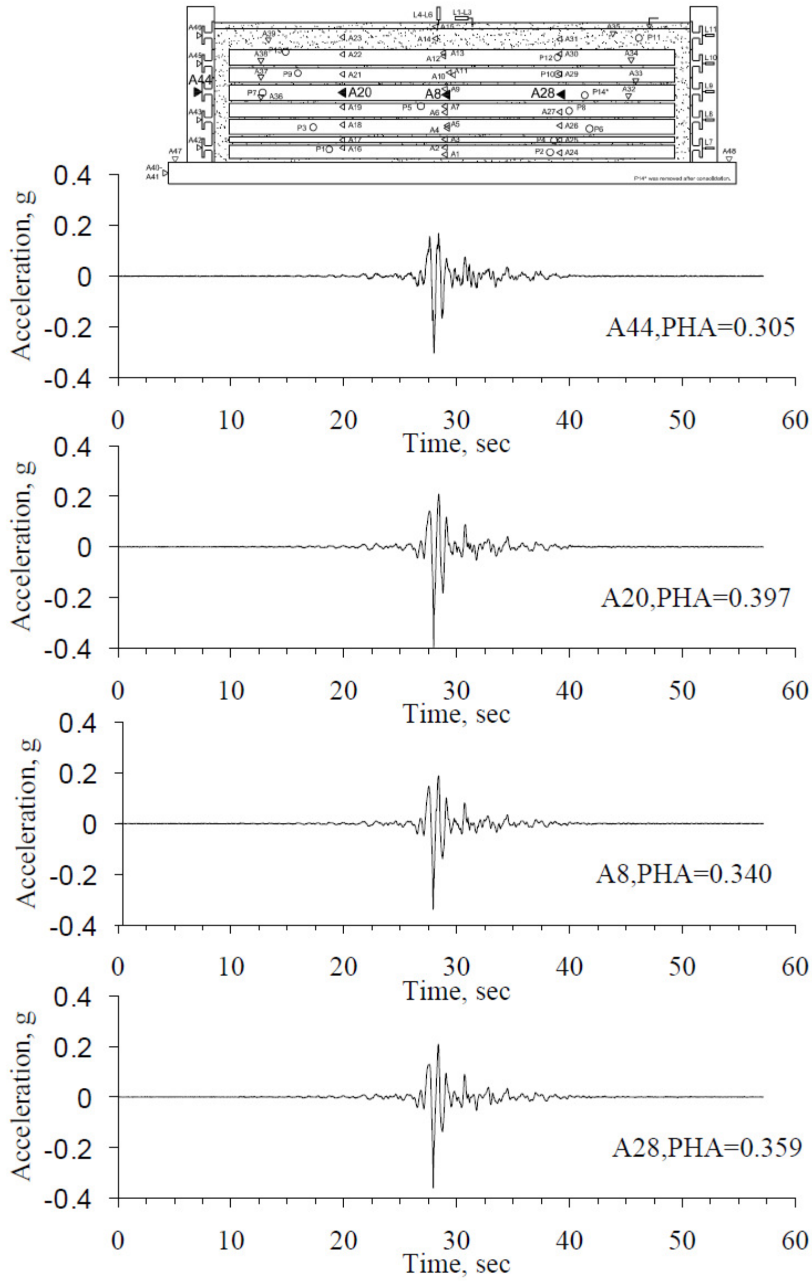

Figure 3.5 **Horizontal acceleration time series for lift 4: Horizontal variation of ground motion**

Figure 3.6 shows the recorded accelerations on each ring of the container. Flexibility of the container is clearly indicated in the time lag of the ground motion from bottom to top. The motion first arrives at the bottom ring, and then in each overlying ring in sequence. A rigid container would respond identically at all elevations.

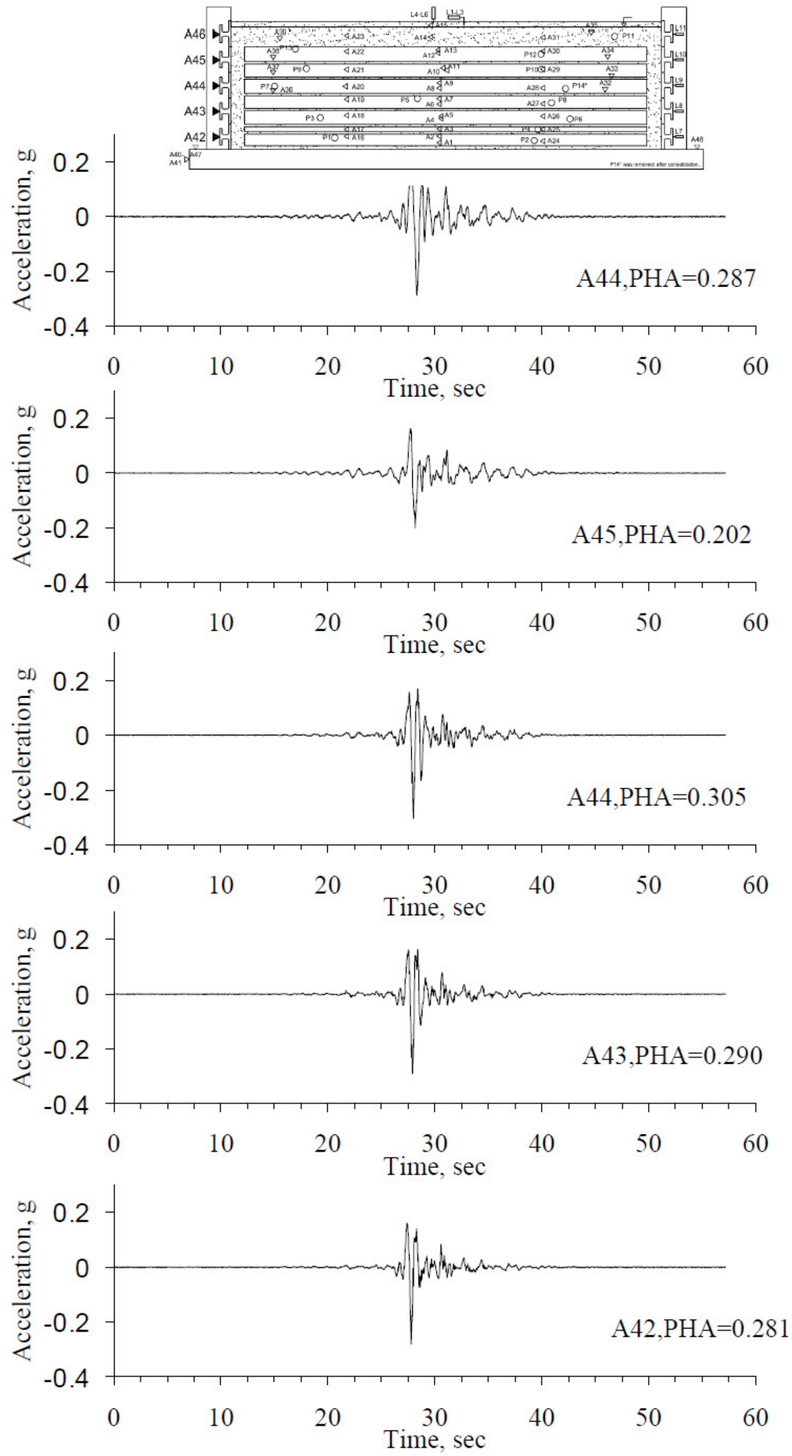

Figure 3.6 Acceleration records for rings of model container

Figure 3.7 shows Fourier amplitude spectra for the four motions from Figure 3.5. The motions are very similar in the frequency band from 0.1Hz to 10Hz, which is an indication that the container performed well in the frequency band of interest. The motion on the ring of the container recorded by sensor A44 had a bit more content at low and high frequency, below 0.15 Hz and above 15 Hz. However, these frequencies are outside of the primary frequency content of the input motion and the differences are deemed inconsequential.

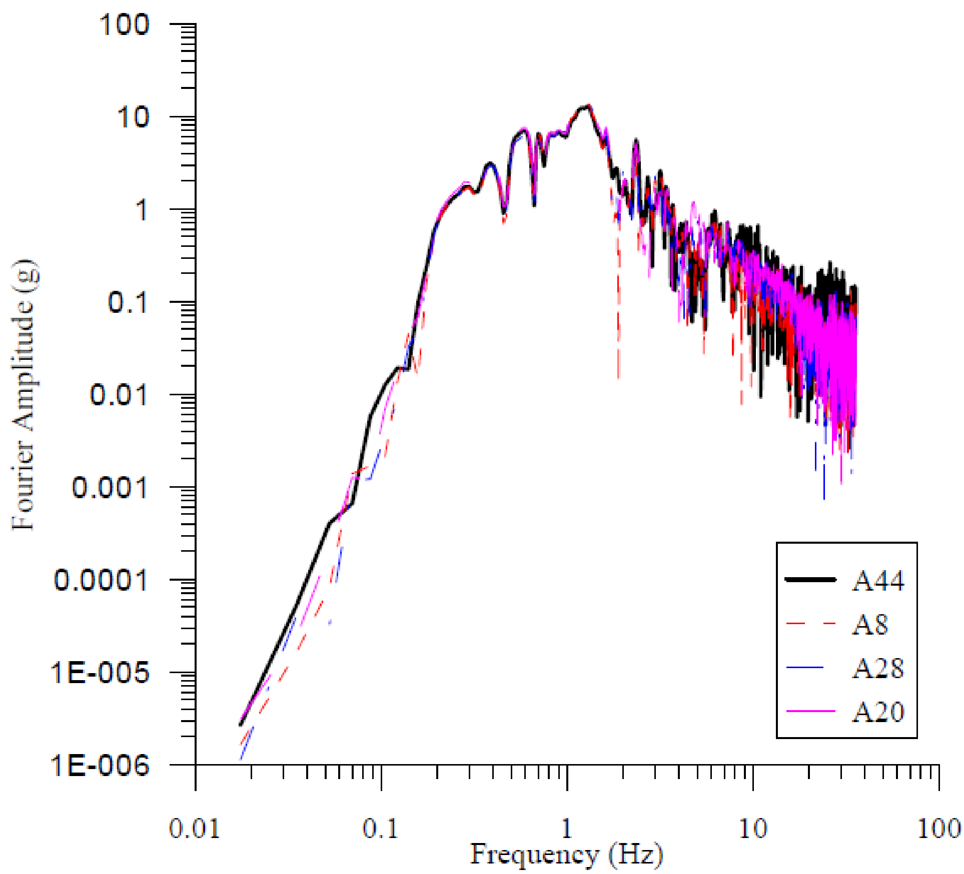

Figure 3.7 Fourier amplitude spectra for motions in Fig. 3.3

3.3.2 Container performance by comparison of previous models

A number of previous centrifuge modeling studies utilized flexible shear beam (FSB) containers consisting of aluminum or steel rings separated by rubber layers that allow the container to deform in a step-wise manner. Container shear stiffness introduces an undesired boundary condition for 1-D site response modeling due to reflections of seismic energy from the container walls. These undesired boundary conditions cause horizontal spatial variation in the ground motions, with the largest effects near the container rings and smaller effects near the center of the soil model. The effects are anticipated to be largest for soft soil conditions, and may be negligible for stiff soil profiles for which the finite container stiffness is a smaller fraction of the system stiffness. Similarly, the effects are anticipated to increase with shaking intensity due to reduction in the shear modulus of the soil at large shear strains.

Undesirable performance of shear beam containers is likely to have affected measured responses in previous studies. For example, Lai et al. (2001) and Elgamal et al. (2005) presented a test program on dense sand constructed in an FSB container. They found that damping values back-calculated from acceleration array data were higher than empirical curves. Utilizing wavelet analysis to analyze the time-dependent frequency content of vertical array acceleration data, they observed that near the walls of the container the frequency content of the ground motion was spread over a larger band than the motions near the center of the model. Moreover, shear strains were larger near the walls of the shear beam container for saturated sand models. These observations were attributed in part to p-waves generated at the container boundary. They acknowledged that container performance might contribute to the high damping values, but indicated that further investigation was needed to explain the experimental finding. Fiegel (1995) implemented a hinged-plate container on the small 1m diameter Schaevitz centrifuge at UC

Davis, and found that the ground motions near the center of the container were very similar to those offset from the centerline at the same elevation. Furthermore, significantly more ground motion amplification was observed in a rigid container compared with the hinged-plate container for high intensity input motions.

We examine the influence of container stiffness by comparing data from test CSP5 (Wilson et al. 1997) with test AHA01. This comparison was chosen because

i. CSP5 utilized a FSB container whereas AHA01 utilized the HPC container,

ii. both models contained layers of lightly overconsolidated San Francisco Bay mud, and

iii. the same ground motion recorded at Port Island during the 1995 Kobe earthquake was input to the base of both models.

Furthermore, a high intensity ground motion is selected because large strains were induced in the clay thereby reducing its shear stiffness, exacerbating any undesired container effects. Acceleration response spectra (5% damping) for a ground motion recorded from an accelerometer embedded near the surface of the soft clay deposit, and on the container ring at the same elevation are shown in Figure 3.8. The ground motion in the clay layer should be identical to the motion on the container at the same elevation if 1-D site response conditions were achieved during the tests. The two response spectra for CSP5 exhibit significant differences at short periods, with the container ground motion approximately twice as large as the soil ground motion. On the other hand, the two response spectra for AHA01 are essentially identical at all periods. This indicates that the HPC container produced better 1-D boundary conditions than the FSB container, and is therefore better suited for site response modeling.

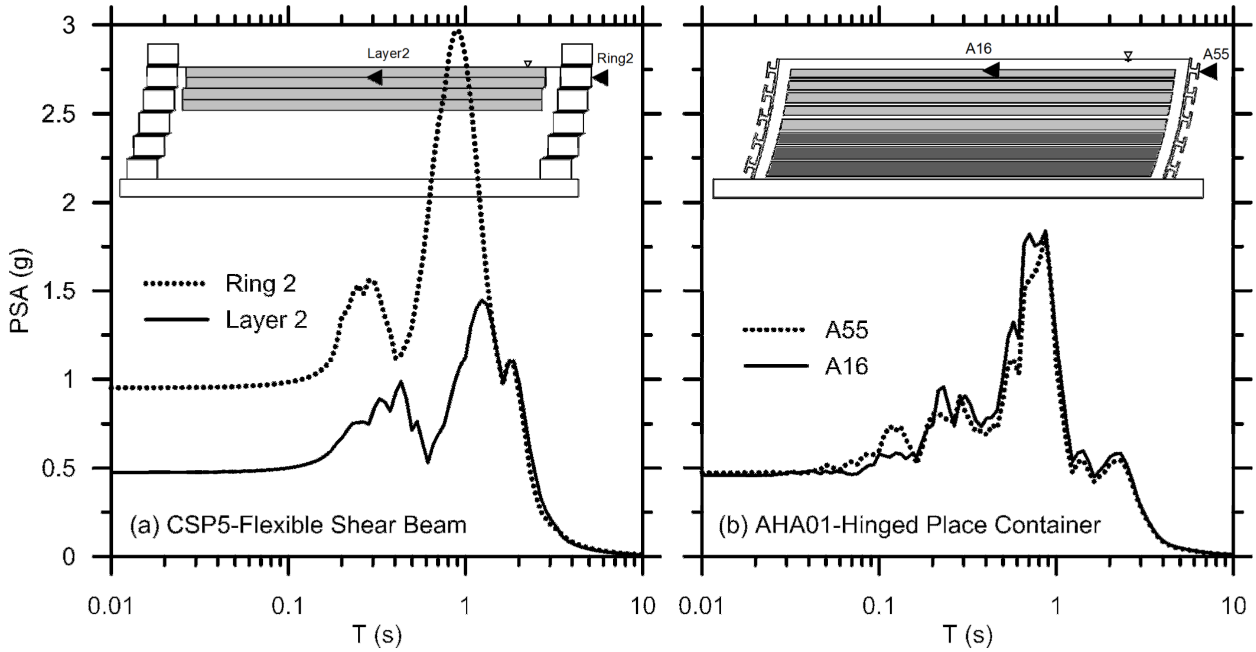

Figure 3.8 Acceleration response spectra (5% damping) near the top of a soft clay layer and on the container ring at the same elevation for (a) test CSP5 tested in a flexible shear beam container (Wilson et al., 1997), and (b) test AHA01 tested in a hinged-plate

3.4 DERIVATION OF SHEAR STRESS AND STRAINS

Stress-strain behavior is the most fundamental feature of nonlinear site response behavior, and is therefore very important to characterize. In this section, stress-strain loops are computed from the recorded data assuming one-dimensional wave propagation. Shear stresses and shear strains was evaluated at selected depths within clay layers from acceleration and displacement data using the procedure of Zeghal and Elgamal (1994). Referring to Figure 3.9, shear stress at depth z and time t was computed by summing the inertia of overlying soil as:

$$\tau_z(t) = \sum_{i=1}^{N(z)} \rho_i \cdot \ddot{u}_i(t) \cdot \Delta z_i \tag{3.2}$$

where index i denotes discrete depth intervals above depth z, each of which has an accelerometer at the middle of the depth interval (i.e., depth z occurs at the boundary between intervals i and

i+1); $N(z)$ is the number of such depth intervals; ρ_i is mass density for depth interval i; $\ddot{u}_i(t)$ is the horizontal acceleration for depth interval i at time t (from the corrected acceleration time series), and Δz_i is the tributary depth associated with interval i.

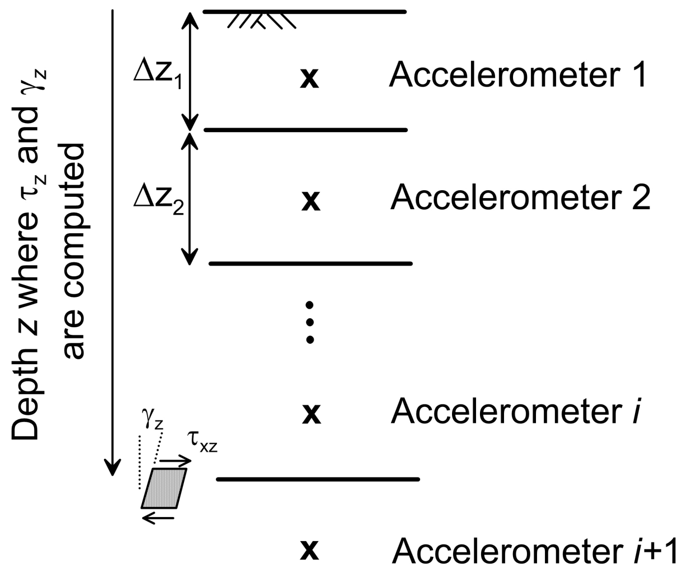

Figure 3.9 Schematic illustration of profile layering used for stress and strain computations

The average shear strain at depth z was computed from the displacement gradient between adjacent accelerometers (i.e., $\gamma = \partial u/\partial z$) as:

$$\gamma_z(t) = \frac{u_i - u_{i+1}}{0.5 \cdot (\Delta z_i + \Delta z_{i+1})} \tag{3.3}$$

The numerator in Eq. (3.3) represents the differential horizontal displacement between the accelerometers immediately above and below depth z, and the denominator represents the vertical distance between those accelerometers.

An example set of stress histories, strain histories, and normalized stress-strain curves at two depths are shown in Figure 3.10. Shear stresses are normalized by the undrained monotonic shear strength computed using Eq. (2.6). The stress and strain histories are shown for the RRS228 motion with various base motion intensities (PHA_b = 0.069g, 0.29g and 0.60g). The normalized stress-strain curves span approximately one loading cycle at the time interval in the strain history when the peak strain occurs.

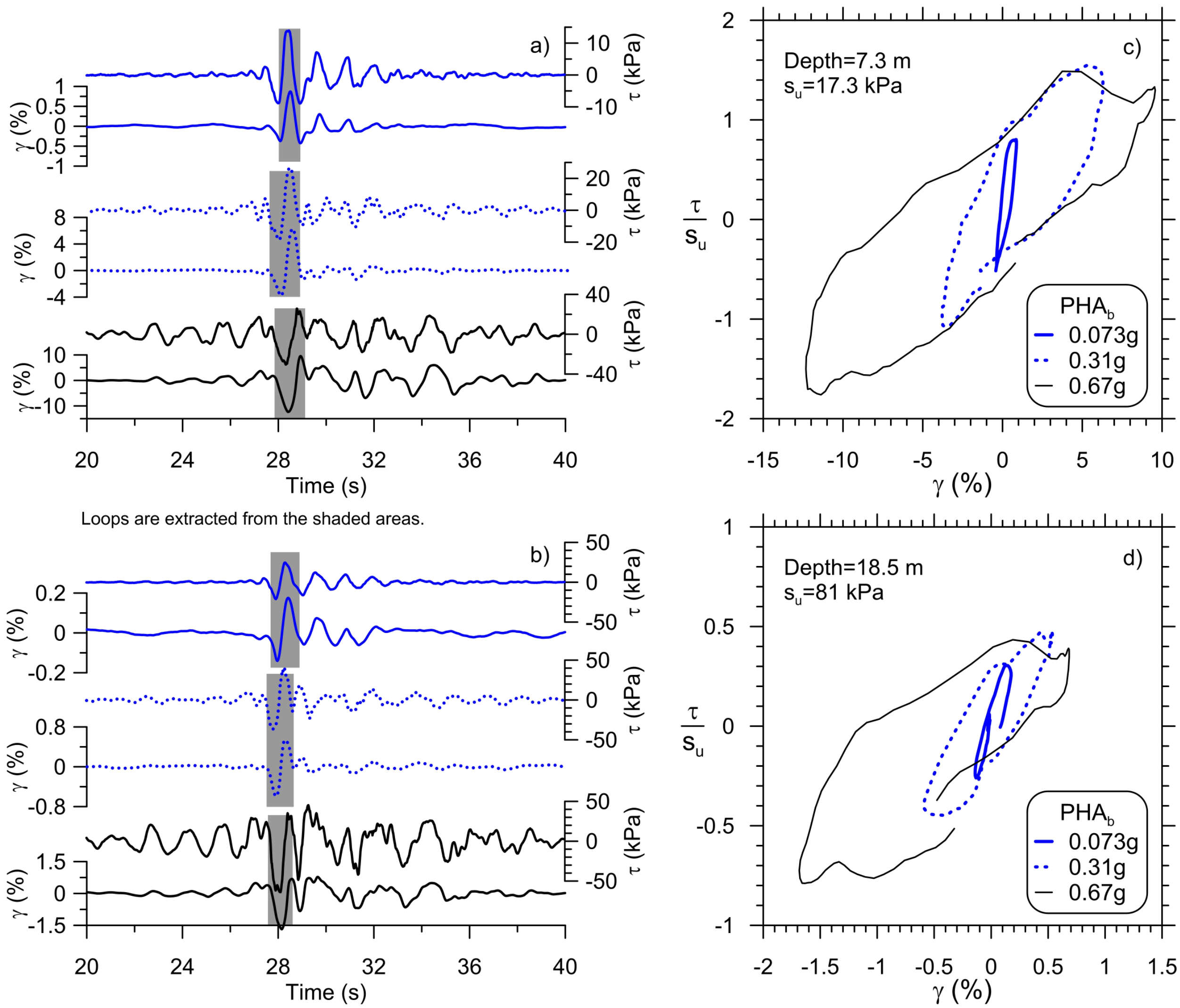

Figure 3.10 Stress and strain histories and stress-strain loops evaluated in relatively soft and firm clay layers when subjected to motion RRS228at various intensities.

The lowest-amplitude stress and strain histories (for PHA_b=0.069g in Figure 3.10a-b) have similar waveforms, which is generally compatible with the assumption of linear (or equivalent-linear) analyses in which the strain history scaled by a constant shear modulus produces the stress history (along with some phase shift from damping). This similarity of waveforms breaks down at larger strains (e.g.,PHA_b=0.60g in Figure 3.10a), where the stress/strain ratio is higher for the small cycles between 20 and 27s than for the large cycle at 28s. The different stress/strain ratios with time for the large intensity motion is caused by the significant reduction in shear modulus associated with such large shear strains. Equivalent linear analysis, in which the shear modulus is independent of time, cannot capture this type of behavior.

Turning next to the stress-strain loops, secant shear modulus decreases as cyclic strain increases in a manner that is similar to traditional cyclic laboratory tests. However, the stress-strain loops are not smooth due to the broadband nature of the input motions. At a depth of 7.3m near the center of the uppermost lift of clay, the shear strain for the motion with PHA_b=0.60g exceeds 10%, while the shear stress exceeds the monotonic undrained shear strength by more than 50%. Strain rate effects explain why the mobilized shear stress exceeded the monotonic undrained strength, as demonstrated later. At a depth of 18.5m, where the clay was overconsolidated, the shear strains are lower (near 1%), and mobilized shear stresses do not reach the monotonic undrained strength.

3.5 MODULUS REDUCTION AND DAMPING BEHAVIOR

Published modulus reduction and damping curves are generally empirically verified to shear strains up to approximately 0.3 to 0.5%, and are often fit with hyperbolic functions that provide a good match with data in this range of strains (e.g., Darendeli, 2001). In practice, these functional forms are often extrapolated to higher shear strains beyond the calibration range, and can provide implied shear strengths that can be significantly different from the soil shear strength (e.g., Stewart and Kwok 2008). It is of interest to compare the modulus reduction and damping behavior evaluated from the centrifuge test data against these published curves, especially in regard to large strain behavior.

Referring to the schematic stress-strain loop in Figure 3.11, we apply the approach of Zeghal and Elgamal (1994) to compute secant shear modulus, G_{sec}, and damping, D. Stress-strain loops like those shown in Fig. 3.10 were generated for each ground motion imposed on the models, and G_{sec} and D were computed. The area of each loop required to obtain D was computed using trapezoidal integration.

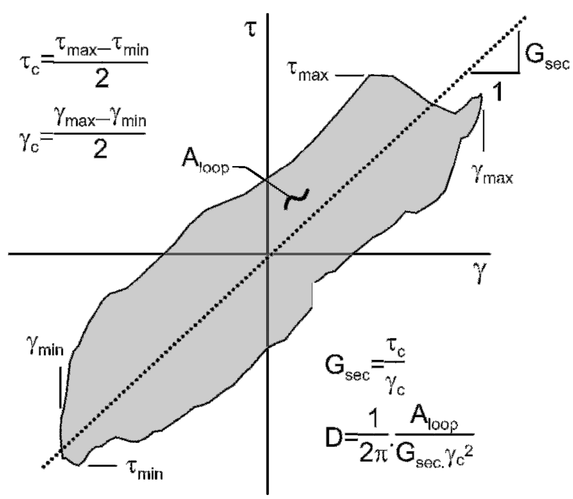

Figure 3.11 Schematic illustration of non-symmetric stress strain loop and quantities used for evaluation of secant modulus G_{sec} and hysteretic damping D

The small strain shear modulus was computed as $G_{max} = \rho V_s^2$, and normalized shear modulus G_{sec}/G_{max} and D were plotted versus shear strain in Figures 3.12a-b. Extracting G_{sec} and

D from the centrifuge data is more complicated than with strain-controlled harmonic laboratory tests because the broadband excitation in the centrifuge models caused asymmetric stress-strain loops that sometimes did not close (e.g., Figure 3.10). Furthermore, shear strains smaller than about 0.02% could not be accurately measured in the centrifuge because the signal-to-noise ratio in the acceleration records is too low at small shaking levels, and because of A/D conversion resolution. Therefore, the data in Figure 3.12 are plotted only for γ_c>0.02%.

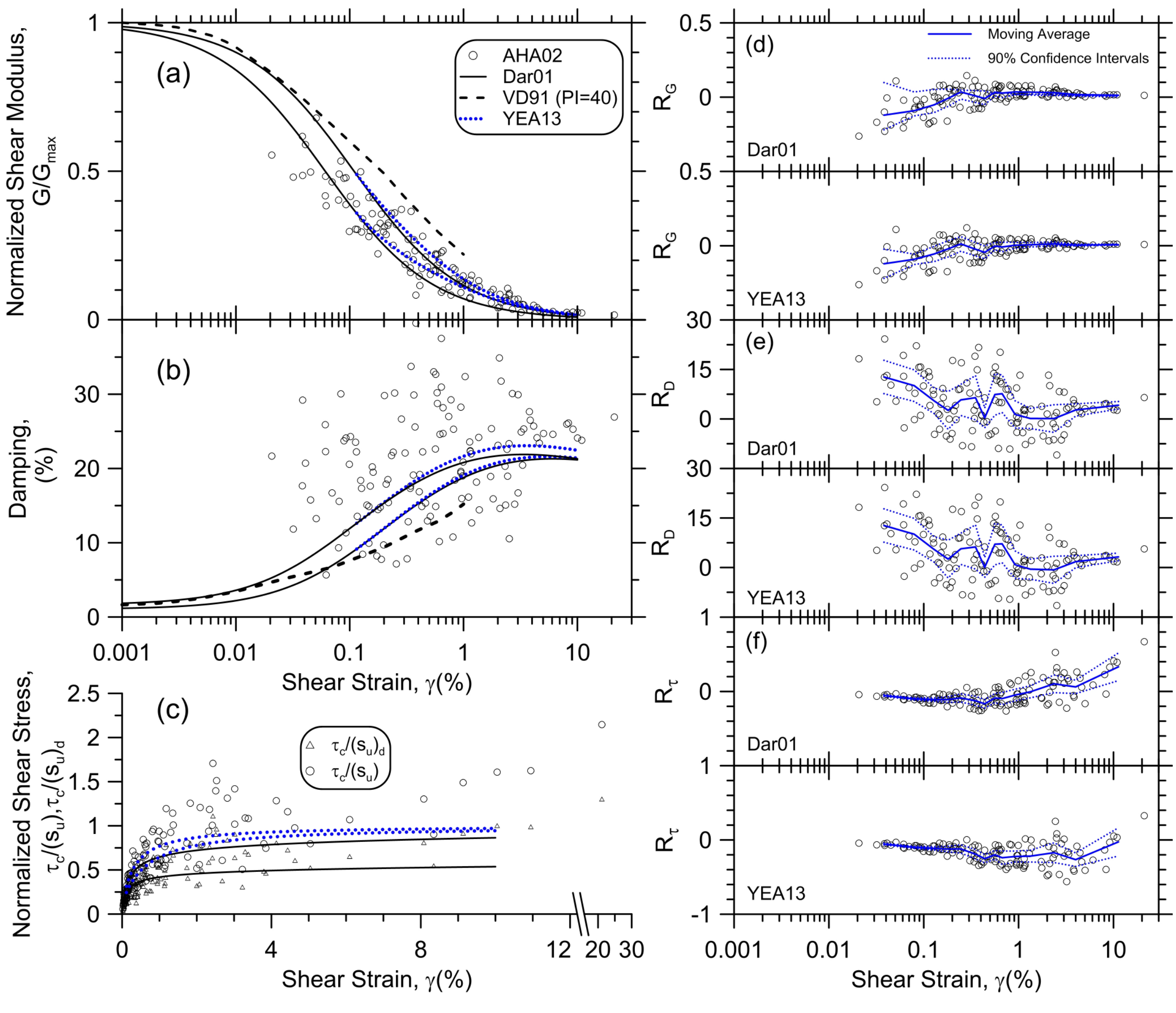

Figure 3.12 Normalized shear modulus, damping and normalized shear stressvs shear strain curves for AHA02 and modulus reduction curves proposed by Vucetic and Dobry(1991), Darendeli (2001) and Yee et al. (2013). Parameter $(s_u)_d$ is the strain rate compatible shear

Also shown in Figure 3.12a are the recommended modulus reduction relations from Vucetic and Dobry (1991) and Darendeli (2001). Two curves are plotted for the Darendeli relation to bound the range of consolidation stress and overconsolidation ratio for the clay in the centrifuge models (the Vucetic and Dobry relation is independent of confining pressure).The Darendeli model is extended to 10% (beyond the upper bound of experimental validation) for the purpose of comparing with the centrifuge test data. In general, Darendeli's functional form appears to provide a reasonable characterization of the observed modulus reduction behavior in the centrifuge models, although a more formal assessment of bias is given below.

Damping values computed from the centrifuge test data (Figure 3.10b) exhibit significant scatter, and tend to be higher than the published trends. This observation is similar to several studies that have utilized 1-D array data to characterize stress-strain behavior for centrifuge models and field arrays (e.g., Elgamal et al. 2001, Tsai and Hashash 2009).

Figure 3.12c shows backbone stress-strain data in which shear stress is normalized by the undrained monotonic shear strength (s_u) and a higher, strain rate-compatible shear strength, $(s_u)_d$. According to Sheahan et al. (1996), undrained shear strength increases approximately 9% per log cycle increase of strain rate, $\dot{\gamma}$. The monotonic undrained strength was measured in the laboratory at a traditional $\dot{\gamma}$ (e.g., 0.006%/s to reach 10% strain in 30 minutes), whereas $\dot{\gamma}$ as high as 6000%/s (model scale) was observed during the centrifuge tests. Strain rate was computed from the centrifuge test data by first computing strain time series, and subsequently differentiating in time by frequency-domain operations. This six order of magnitude increase in $\dot{\gamma}$ corresponds to $\left(s_u\right)_d / s_u = 1.09^6 = 1.67$. Values of $(s_u)_d$ were obtained for each motion by computing the peak strain rate mobilized during each motion, and correcting as demonstrated above. This is admittedly an extrapolation of Sheahan's findings because strain rates mobilized in the centrifuge were much higher than those imposed in laboratory studies. In Figure 3.12c, the $\tau_c/(s_u)_d$ values approach unity at high strain values, whereas τ_c/s_u values significantly exceed unity. This shows that strain-rate corrections should be applied to shear strengths for site response problems. Strain rates mobilized in centrifuge models are approximately two orders of magnitude larger than those anticipated for prototype conditions due to the centrifuge time scaling, but the increase in shear strength is nevertheless significant for anticipated prototype strain rates. We recognize that rate effects may also be present for shear stiffness (i.e., V_s or G_{max}), but in this case the geophysical measurements were made at strain rates that were not significantly different from those mobilized during shaking since we used bender element measurements and high frequency harmonic motions to measure the V_s profile. Therefore we did not correct shear stiffness for rate effects.

Along with the data, Figure 3.12c also shows stress-strain curves implied by Darendeli's functional form. The shear strength implied by extrapolating the function to high strain is significantly smaller than the monotonic undrained strength of the clay, which is clear from the stress-strain curves (Figure 3.12c) but not evident from the modulus reduction plots (Figure 3.10a). Yee et al. (2013) proposed a procedure to adjust the modulus reduction curve to provide the desired undrained shear strength [taken as $(s_u)_d$]at high strains. The resulting modulus reduction, damping, and stress-strain curves are shown with dotted lines in Figures 3.12a-c. The modified stress-strain relation asymptotically approaches $(s_u)_d$ as shear strain goes to infinity, which provides a better match to the $\tau_c/(s_u)_d$ data. The improved fit is not visible from the modulus reduction curves, which are poorly suited to visualization of large-strain behavior (i.e., very small variations in modulus reduction at high strain cause large variations in implied shear stress).

The data points in Figures 3.12a-c correspond to a variety of σ_v' and OCR values, complicating the data-model comparison. To facilitate a more formal evaluation of model performance, we compute residuals defined as the difference between the recorded data and the models (Sheather, 2009) for modulus reduction (R_G), damping (R_D), and normalized stress (R_τ) as follows:

$$R_G = \left(\frac{G_{\sec}}{G_{\max}}\right)_{data} - \left(\frac{G_{\sec}}{G_{\max}}\right)_{Model} \tag{3.4a}$$

$$R_D = D_{data} - D_{Model} \tag{3.4b}$$

$$R_\tau = \frac{\tau_{data} - \tau_{Model}}{(s_u)_d} \tag{3.4c}$$

Model equations are omitted for brevity (they can be found in the references), but include effects of consolidation stress, OCR, and plasticity index. The equations for Yee et al. (2013) will be presented in the following chapter where the modulus reduction and damping curves are derived for the nonlinear site response simulations Within the strain range of range of applicability of the Darendeli model ($\gamma_c \leq \sim 0.3\%$), modulus reduction residuals (Figure 3.12d) generally indicate negative bias (i.e., model too linear) whereas damping residuals indicate positive residuals (model damping too low).The dispersion of modulus reduction and damping results can be represented by standard deviations of the residuals in Figures 3.10d-e, which are 0.083 and 8.33%, respectively, for γ=0.3%. These can be compared to standard deviations of 0.065 and 2.04% over a comparable strain range for the data used to develop the Darendeli model.

At large strains, the most relevant results are the stress residuals (Figure 3.12f), which are significantly positive for Darendeli (model underpredicts stress) and close to zero for Yee et al.

These differences in large strain soil properties have been shown to significantly affect the results of nonlinear ground response analyses, as shown for example in comparisons to vertical array data by Yee et al. (2013).

3.6 SPECTRAL AMPLIFICATION OF GROUND MOTIONS

Having described dynamic properties of the clay during the centrifuge tests, we now turn our attention to spectral amplification. The term 'spectral amplification' refers to the ratio of the 5% damped pseudo acceleration (*PSA*) response spectra of the recorded ground surface and container base motions:

$$F(T) = \frac{PSA_0(T)}{PSA_b(T)} \tag{3.5}$$

Response spectra for the LGPC090 motion at three intensity levels are shown in Figure 3.13a, while Figure 3.13b shows the period-dependent spectral amplification values, *F*. Several trends are evident from the spectra and amplification plots:

i. Amplification levels are relatively flat for T<~ 0.5s and are strongly variable with the level of input motion (weak motions producing amplification near 2 and strong motions producing amplification near 0.5).

ii. Relatively narrow-band and substantial amplification up to a factor of 3occurs near the elastic site period (near 1.0s) for the weakest motion, whereas stronger motions both lengthen the period to as much as 3sand broaden the spectral peak. These effects are expected because of the modulus decrease and damping increase when the soil is subjected to increased shaking intensities.

iii. Lastly, for periods beyond the site period, amplification levels are larger than 1.0, with the relative levels of amplification being the inverse of the short period trends (amplification increasing with strength of input motion). This apparent reversal of traditionally understood nonlinear effects appears to result from the transfer of energy to increasingly long periods as the soil softens.

The response spectra extend to periods of only 5s because low frequency noise in the acceleration records rendered poor signal-to-noise ratio at longer periods.

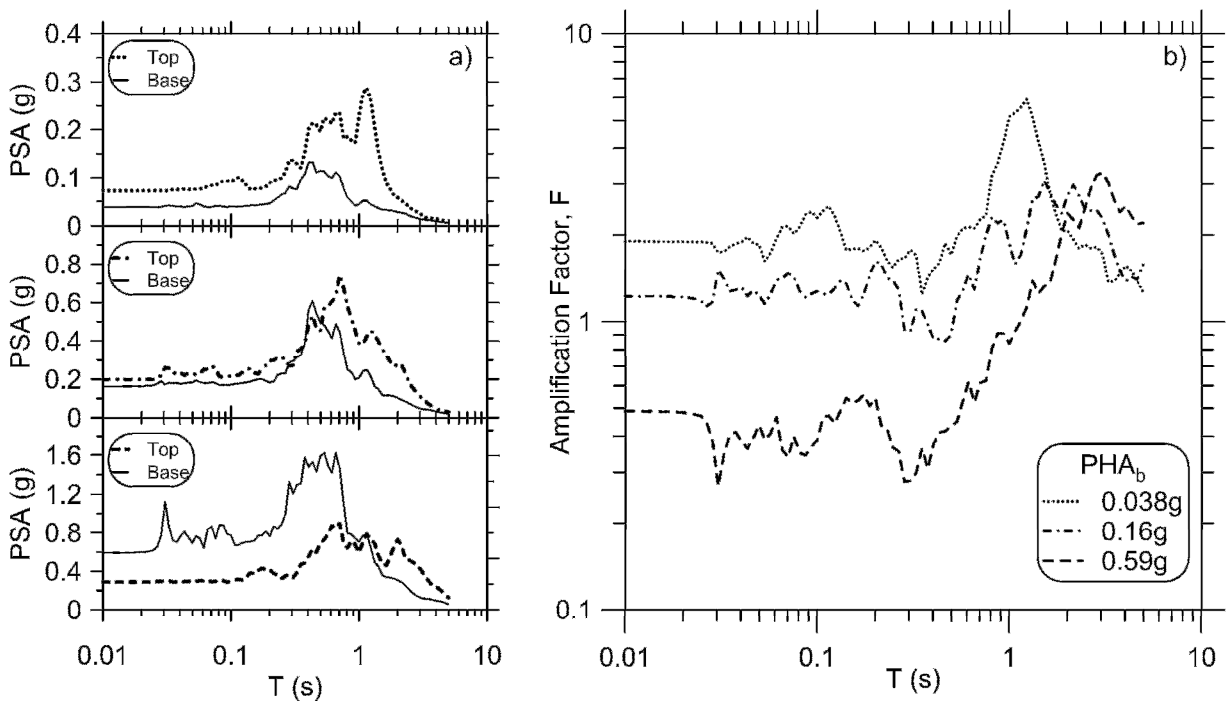

Figure 3.13 (a) Acceleration response spectra for base and top of the model for the LGPC090 ground motion and (b) Amplification Factors for the LGPC090 ground motion.

Spectral amplification is parameterized as a function of V_{s30} in the site terms used in the Next Generation Attenuation (NGA) ground motion prediction equations (GMPEs). GMPE site terms represent the ratio of mean ground motion for a given V_{s30} to that for a reference velocity

(V_{ref}), with both motions corresponding to outcropping (ground surface) conditions. The functional form of the site terms includes a linear amplification term that captures the scaling of ground motion with V_{s30} and a nonlinear term that captures the variation of F with PHA_b (or a reference PSA term) for the given V_{s30}. The centrifuge models have a strong impedance contrast at the base of the clay (the container base is essentially rigid), which is atypical of field conditions. Moreover, spectral amplification from Eq. (3.5) is defined as surface-to-base rather than surface-to-surface for two different site conditions. Accordingly, we do not expect a perfect match to the overall level of site amplification (represented by the linear component of site terms) but we consider the test data to be useful for checking the nonlinear terms in the GMPEs.

To investigate the nonlinearity implied by the test results, we plot in Figure 3.14 spectral amplification factors (F) for T = 0.01s, 0.1s, 1.0s, and 3.0s versus PHA_b. Also shown for comparison are the predictions of the site term in the Seyhan and Stewart (2014) GMPE, which is adapted from the model of Choi and Stewart (2005). There are several interesting features in these plots.

i. The slopes of the ln(F) vs. ln($\mathrm{PHA_b}$) relations for large PHA_b, which are denoted as F_2 values and effectively parameterize the nonlinearity, are similar between the GMPE and data. This is not necessarily expected, because the GMPE site term was derived for sites generally significantly stiffer than those in the centrifuge tests (even the NEHRP Class E sites used in the model development), so the comparison here represents an extrapolation of the model.

ii. We do not see clear evidence of an inflection point in the ln(F) vs.ln($\mathrm{PHA_b}$) data for very strong PHA_b, where soil failure is occurring. This suggest that amplification models with a simple linear representation of the ln(F)-ln(PHA_b) relationship at large PHA_b may be acceptable.

iii. The data for T = 0.1s and 1.0s indicate a clear break from relatively linear site response (roughly independent of PHA_b) for low input motion levels to nonlinear at transitional PHA_b values ranging from about 0.01g to 0.1g. Roughly similar transitional PHA_b values are reflected in the GMPE site terms, as shown in Fig. 2.13.

iv. Lastly, the data for T = 3.0s indicate a generally flat trend with PHA_b, potentially even trending upward (positive F_2) for high values of PHA_b. This effect is not captured by the model, which retains a reduced level of nonlinearity at long period.

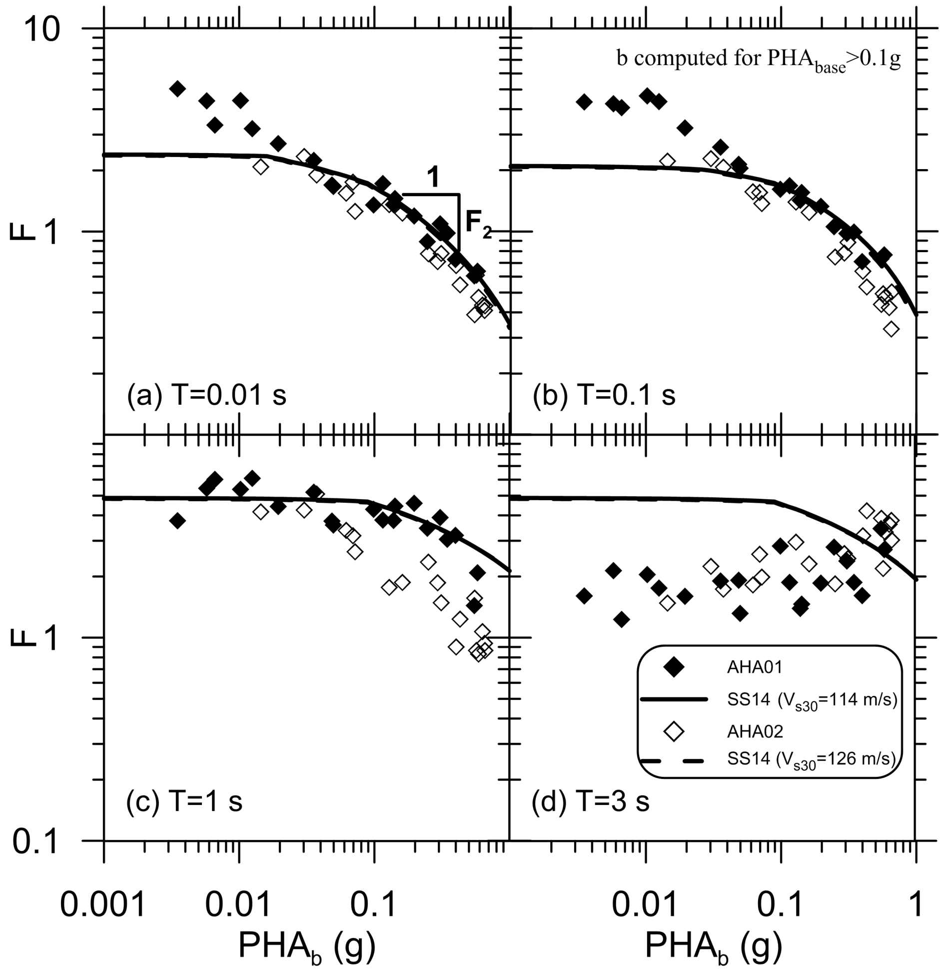

Figure 3.14 Amplification factor versus peak horizontal acceleration at (a) T=0.01 s, (b) T=0.1 s, (c) T=1 s and (d) T=3 s for all of the ground motions recorded in this study.

In Figure 3.15 plots the period-dependence of slope parameter F_2 computed from the test data using results with $PHA_b \geq 0.1$g. Also shown in Figure 3.15 are the trends of slope identified in previous models derived from ground motion data (Boore and Atkinson, 2008 and Seyhan and Stewart, 2014) and equivalent-linear simulations (Walling et al. 2008). The principal difference between *b* value trends in the two prior models is the significant dip between 0.1s and 1.0s in the simulation-based results (Walling et al.2008). Interestingly, the centrifuge data are more consistent with the relatively flat trend of the model derived from data (Boore and Atkinson, 2008 and Seyhan and Stewart, 2014).

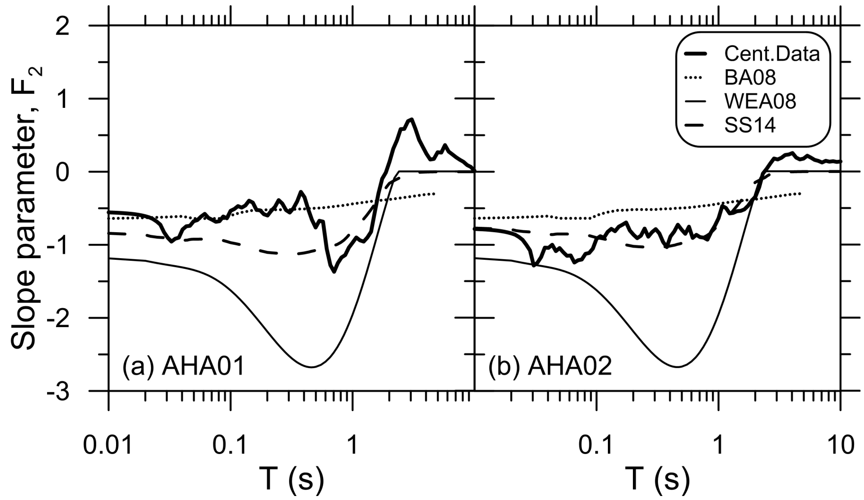

Figure 3.15 Slope of the amplification factors from centrifuge test data compared with similar slopes from data- and simulation-driven models used in GMPE's

4 TOTAL STRESS SITE RESPONSE MODELING OF SOFT CLAY CENTRIFUGE MODELS

Having interpreted the data, the next step is to understand how well nonlinear site response simulations can model the observed soil behavior. This chapter presents total stress site response modeling using DeepSoil and OpenSees. First, corrections to the large-strain portion of a modulus reduction curve to provide the desired strength is explained. The correction depends on the particular modeling platform being used. Second, corrections for strain rate effects are explored. Then, the details of the site response models will are presented. Finally, results are compared in terms of

i. influence of undrained shear strength,
ii. modeling platforms (DeepSoil versus OpenSees)
iii. modeling approaches (nonlinear versus equivalent linear)
iv. importance of strain rate correction

Errors are quantified in terms of the residuals of various intensity measures.

4.1 INTRODUCTION

Nonlinear site response simulations were performed using DeepSoil and OpenSees, and equivalent linear simulations were performed using DeepSoil. Ground motions recorded from an accelerometer embedded in the clay near the base of the centrifuge modeling container were imposed as "within" motions following the guidance of Kwok et al. (2007). The motion of the base plate was not used in these simulations because slip between the base plate and latex membrane containing the soil was observed during shaking.

The site response modeling focuses on two fundamental issues:

i. proper modeling of shear strength, and

ii. correction of shear strength to account for strain rate effects.

Each of these topics is discussed in detail, and we then present seven different models that utilize different modeling approaches (nonlinear vs. equivalent linear, OpenSees vs. DeepSoil), and shear strength profiles. Comparisons between predicted and measured ground motions are presented in the form of residuals of spectral accelerations versus period, and Arias intensity and cumulative absolute velocity versus peak base acceleration.

4.2 ADJUSTING MODULUS REDUCTION CURVE TO PROVIDE DESIRED SHEAR STRENGTH

Modulus reduction curves are commonly derived from cyclic laboratory tests that extend to strain amplitudes as high as about 0.3%. Many combinations of earthquake ground motions and soil conditions will result in peak strains that are lower than 0.3%, in which case analyses can be performed within the range of experimental validation of the modulus reduction curves. However, strong ground motions imposed at the base of soft soil layers may result in shear strains that exceed 0.3%, possibly mobilizing shear failure in extreme conditions. This is precisely the scenario for which nonlinear site response analysis is anticipated to provide the largest benefit relative to equivalent linear methods. However, such analyses require extrapolation beyond the range of experimental validation. Often, the equations defining the modulus reduction curves at small strains are simply extrapolated to large strains. This procedure can result in significant under-prediction or over-prediction of shear strength depending on the ratio of shear strength to small strain shear modulus.

To demonstrate this issue, the Darendeli (2001) modulus reduction curve equation (Eq. 4.1) is defined for the bay mud using a=1.05, and γ_r=(0.035+0.001·PI·OCR$^{0.25}$)·(σ_o')$^{0.5}$. The value of G_{max} was obtained from the V_s profile in Figure 2.8.

$$\frac{G}{G_{\max}} = \frac{1}{1+\left(\frac{\gamma}{\gamma_r}\right)^a} \tag{4.1}$$

A stress-strain curve can be computed from a modulus reduction curve as $\tau = G\gamma$. A true shear strength, defined as a horizontal asymptote for the stress-strain curve, does not exist for Darendeli's modeling equation for values of a unequal to 1.0. Therefore an implied shear strength τ_{imp} is taken as the value of shear stress corresponding to a shear strain of 10%. The values of τ_{imp} are plotted along with measured monotonic undrained strengths in Figure 4.1. Additionally, strain-rate-corrected shear strength profiles, described later in the report, are also shown in Figure 4.1. The shear strengths implied by Darendeli's equation are significantly lower than the measured monotonic undrained shear strengths in this case. The fact that Darendeli's equation does not accurately capture shear strength is not surprising considering the equation is valid only up to 0.3%. However, this exercise clearly illustrates that the high strain portion of modulus reduction curves should be altered to obtain a desired shear strength. The under-prediction of shear strength in this case is not a general observation; depending on the ratio of s_u/G_{max}, extrapolating the modulus reduction curve may produce a shear strength that is lower or higher than desired.

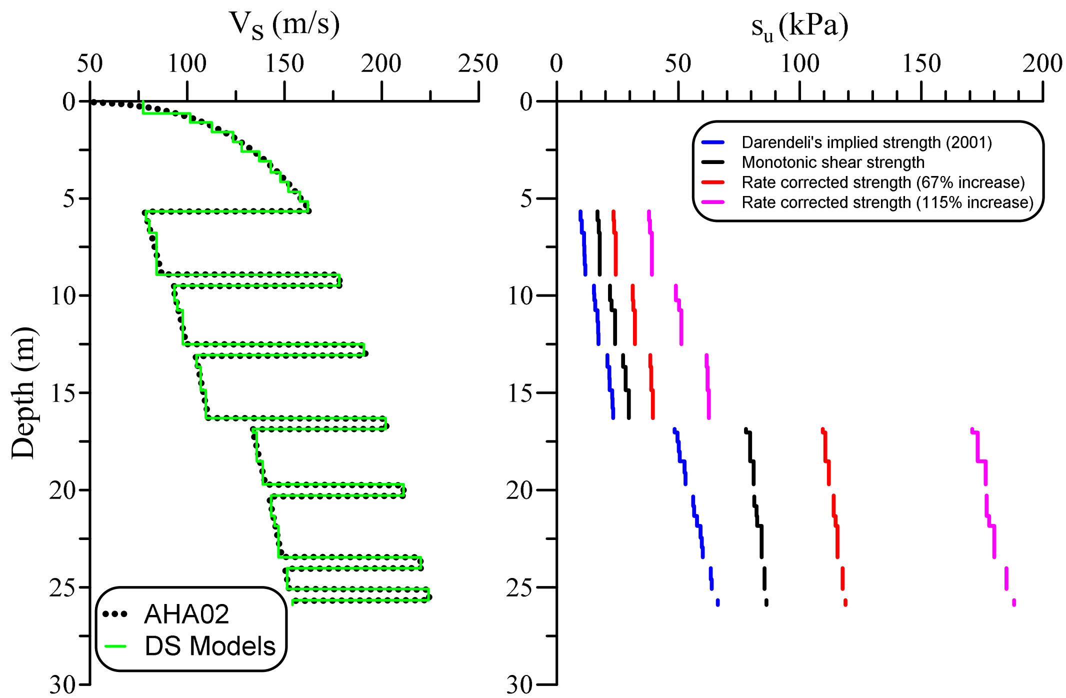

Figure 4.1 Shear wave velocity profile and shear strength profile.

Yee et al. (2013) developed a procedure that correctly captures a desired shear strength by extrapolating a modulus reduction to high strains using a hyperbolic function that asymptotically approaches the desired shear strength. The procedure involves the following steps:

(1) select a transition shear strain, γ_t, at which to transition from the modulus reduction curve to the hyperbolic function,

(2) compute the tangent stiffness of the stress-strain curve, G_{tan}, at this strain level based on the modulus reduction curve equation (Eq. 4.2) for Darendeli functional form),

(3) compute the shear stress associated with the transition strain, τ_t, (Eq. 4.3),

(4) compute a reference shear strain for the hyperbolic portion of the stress-strain curve (Eq. 4.4), and

(5) compute the stress strain curve using the modulus reduction curve if $\gamma < \gamma_t$ and the hyperbolic curve if $\gamma \geq \gamma_t$ (Eq. (4.5)). This procedure results in a stress-strain backbone curve that is continuous, and whose slope is continuous, and approaches the desired shear strength.

$$G_{\tan} = \frac{G_{\max}\left[\left(\frac{\gamma_t}{\gamma_r}\right)^a - a\left(\frac{\gamma_t}{\gamma_r}\right)^a + 1\right]}{\left[1+\left(\frac{\gamma}{\gamma_r}\right)^a\right]^2} \tag{4.2}$$

$$\tau_t = \frac{G_{\max}\cdot\gamma_t}{1+\left(\frac{\gamma_t}{\gamma_r}\right)^a} \tag{4.3}$$

$$\gamma_{ref} = \frac{s_u - \tau_t}{G_{\tan}} \tag{4.4}$$

$$
\begin{aligned}
\tau &= \frac{G_{\max}\cdot\gamma}{1+\left(\dfrac{\gamma}{\gamma_r}\right)^{a}} && if \quad \gamma<\gamma_t \\
\tau &= \tau_t + \frac{G_{\tan}\cdot(\gamma-\gamma_t)}{1+\left(\dfrac{\gamma-\gamma_t}{\gamma_{ref}}\right)} && if \quad \gamma\geq\gamma_t
\end{aligned}
\tag{4.5}
$$

An example calculation demonstrating the Yee et al. correction is performed for the upper lift of clay from AHA02 for which PI = 40, OCR = 1.15, σ_o' = 48 kPa, s_u = 17 kPa, and V_s = 80 m/s. Three different values of γ_t are plotted for reference, along with the extrapolated Darendeli curve. As the value of γ_t increases, the Yee et al. modulus reduction curve more closely resembles the Darendeli curve. Despite very minor differences in the modulus reduction curve at large strains, the stress-strain curves are significantly different, and the Darendeli curve approaches a strength that is less than 60% of the monotonic undrained shear strength, whereas the Yee et al. curves all approach the undrained strength. This is a clear indication that very minor adjustments to the large-strain portion of the modulus reduction curve cause very significant changes in the implied strength, and care must be taken to adjust the tail of the modulus reduction curve to accurately reproduce a target strength.

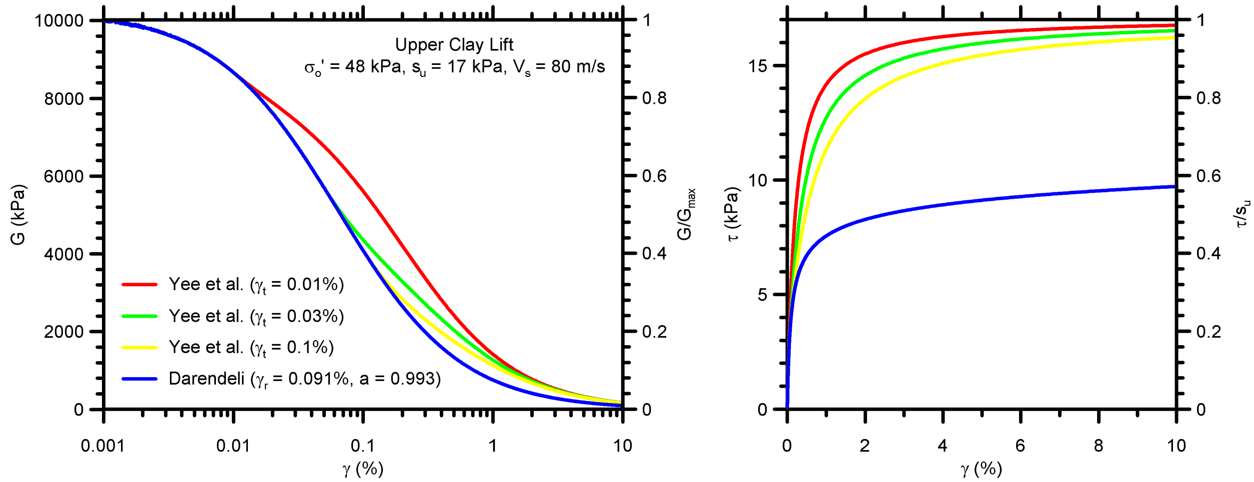

Figure 4.2 Illustration of Yee et al. (2013) curve-fitting procedure to obtain a desired shear strength.

DeepSoil utilizes a hyperbolic backbone curve that can be curve fit to a target modulus reduction curve using a least-squares regression algorithm. However, the algorithm attempts to fit the entire modulus reduction curve, and very small misfits at large strain can result in significant deviations from the desired shear strength, as demonstrated in Figure 4.2. In general, the hyperbolic fit resulted in an under-prediction of the desired shear strength for the clay soils in this study. To solve this problem, we adopted an iterative procedure in which the "target" modulus reduction curve was seeded with erroneously high values at high strain until the resulting stress-strain curve fit the target strength (Hashash, personal communication). This increased the misfit at small strain, but this is a compromise that must be made in the current DeepSoil implementation. Such corrections are not required in OpenSees since the PressureIndependMultiYield model permits direct specification of the undrained strength, which is controlled by the size of the largest nested yield surface.

4.3 CORRECTION OF SHEAR STRENGTH FOR STRAIN RATE EFFECTS

The shear strength of soil is known to depend upon strain rate. Sheahan et al. (1996) performed laboratory tests on clay specimens and found that the undrained shear strength increased approximately 9% per log cycle increase in strain rate for a range of strain rates from 0.05%/hr to 50%/hr. The centrifuge tests mobilized strain rates as high as 6000%/s, which exceeds the range of the Sheahan et al. study by a factor of 36,000. Yong and Japp (1969) performed tests on clays at much higher strain rates consistent with blast loading, and found that the increase in shear strength is a nonlinear function of strain rate. Strength increases at a rate consistent with that proposed by Sheahan et al. at rates lower than about 100%/s, whereas shear strength increases more rapidly at rates higher than 100%/s.

Figure 4.3 shows stress-strain pairs recorded at stress peaks mobilized during the centrifuge test for the upper clay layer in AHA02. The undrained shear strength of the clay measured at a typical laboratory strain rate (assumed to be 20%/hr) is about 17 kPa for this soil. The peak mobilized shear stress is approximately 37 kPa, which is a 115% increase in undrained strength. Backbone stress-strain curves obtained using the Darendeli (2001) modulus reduction curve equation combined with the Yee et al. (2013) procedure are superposed on the data. These backbone curves correspond to the monotonic undrained strength, a strength increase of 67% (consistent with the Sheahan et al. finding), and a strength increase of 115%. The highest curve envelopes the measured data, which we consider to be the most appropriate backbone since the recorded data points should reside within the region bounded by the backbone curve (we do not necessarily anticipate the data points to lie on the backbone curve due to the broadband nature of the input motion and the strain history developed during shaking; a previous cycle may introduce permanent strain in a particular direction prior to the peak stress being recorded).

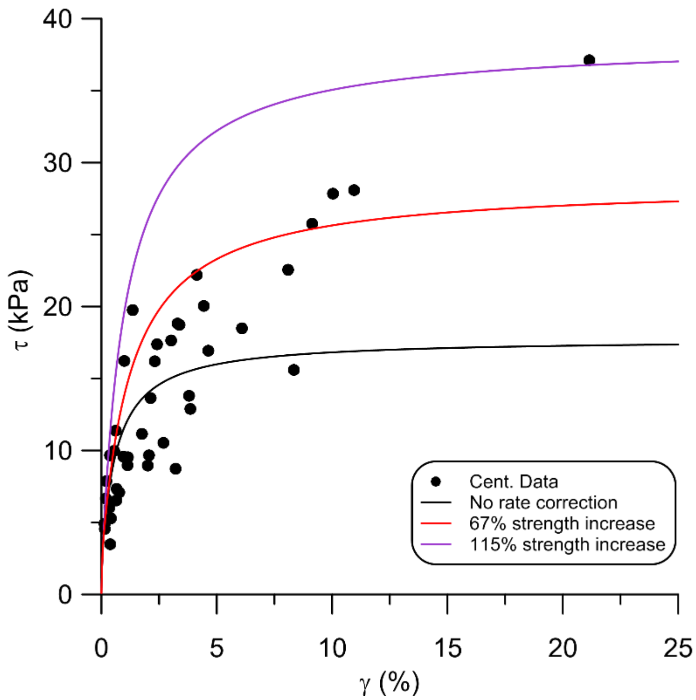

Figure 4.3 The backbone shear stress curves for the top clay layer. Model 1 uses the modulus reduction and damping curves generated by Darendeli (2001) procedure, Model 2 uses the modulus reduction and damping curves generated by Yee et al. (2013) and Model 3 follows the Yee et al. (2013) procedure considering the rate effect

Figure 4.4 shows the undrained strength ratio versus strain rate including the range of strain rates tested by Sheahan et al. (1996), Yong and Japp (1969), and the peak strain rate measured in the centrifuge test (which also happens to be associated with the peak stress and peak strain measurement). Sheahan et al. and Yong and Japp tested different soils and there was no range of overlap in the strain rates they tested, but the relative increase suggested by Sheahan et al. was similar to that suggested by Yong and Japp for strain rates lower than about 100%/s, after which the strength increases more sharply with increase in strain rate. Based on these observations, we have constructed a curve for the bay mud tested in the centrifuge test based on the assumption that the monotonic undrained strength measurement is associated with a strain rate of 20%/hr. The peak measured shear stress lies between the extrapolation of the Sheahan et al. laboratory testing program, and the rapid increase in strength at high strain rate observed by Yong and Japp. More research is required to more fully characterize the strength increase over the full range from typical laboratory strain rates to very high strain rates anticipated during earthquake loading. Although the model scale peak centrifuge strain rate was very high (approx. 6000 %/s), high strain rates would also be anticipated for shear failure under prototype shaking conditions. The prototype strain rate in this case would be about 100 %/s, which is well above the range measured by Sheahan et al. However, the best currently available evidence indicates that the Sheahan et al. extrapolation would be appropriate for the prototype strain rates associated with the centrifuge test, and that this rate correction can be applied for analysis of field cases until better information becomes available through additional research.

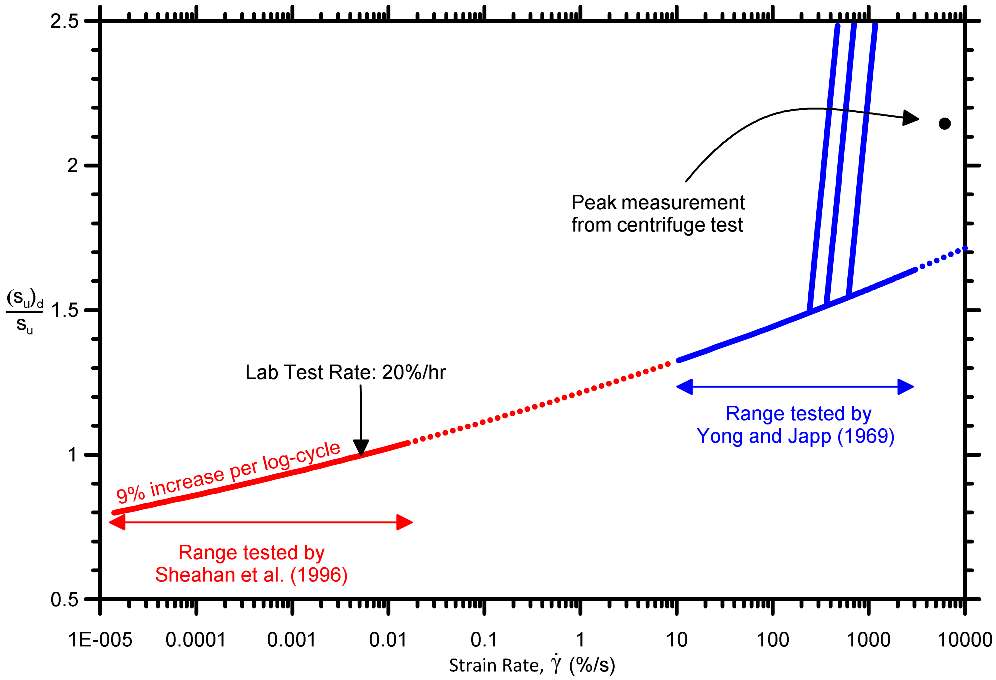

Figure 4.4 Strain rate effect measured by Sheahan et al. (1996), Yong and Japp (1969), and the peak stress-strain point measured in the centrifuge test.

4.4 SITE RESPONSE MODELING ANALYSES

A total of seven different models were performed for various combinations of modeling platforms (DeepSoil and OpenSees), analysis approaches (nonlinear and equivalent linear), and shear strength profiles (Table 4.1). Undrained shear strength was set to be equal to the strength implied by extrapolating the Darendeli relation (Model 1), the monotonic undrained strength (Model 2), a rate-correction of 115%, which is consistent with the peak measured ratio of $(s_u)_d/s_u$ (Models 3, 4, and 5), and a rate-correction of 67%, which is consistent with the correction by extrapolating Sheahan et al. to high strain rates (Models 6 and 7).

Table 4.1 Configuration of seven models analyzed in this study.

Model #	Nonlinear (NL) or Equivalent Linear (EQ)?	Modeling Platform	Modulus Reduction Curve	Damping Curve	Shear Strength Correction	Rate Correction
Model 1	NL	DeepSoil	Darendeli (2001)	Darendeli (2001)	None	0%
Model 2	NL	DeepSoil	Darendeli (2001)	Darendeli (2001)	Yee et al. (2013)	0%
Model 3	NL	DeepSoil	Darendeli (2001)	Darendeli (2001)	Yee et al. (2013)	115%
Model 4	NL	OpenSees	Darendeli (2001)	Masing's Rules	Yee et al. (2013)	115%
Model 5	EQ	DeepSoil	Darendeli (2001)	Darendeli (2001)	Yee et al. (2013)	115%
Model 6	EQ	DeepSoil	Darendeli (2001)	Darendeli (2001)	Yee et al. (2013)	67%
Model 7	NL	DeepSoil	Darendeli (2001)	Darendeli (2001)	Yee et al. (2013)	67%

DeepSoil is used for all of the models other than Model 4, which uses OpenSees instead. In DeepSoil, the target modulus reduction and damping curves were obtained using the hyperbolic fitting procedure described previously (the "UIUC" approach in DeepSoil). In OpenSees, the PressureIndependMultiYield (PIMY) material model (Elgamal et al., 2003) was used for the clay layers and the PressureDependMultiYield (PDMY) models as used for the sand layers. The outer yield surface was set to model the desired undrained shear strength, and the intermediate yield surfaces were set to match the desired modulus reduction backbone curve. The PIMY and PDMY material models adopt Masing's rules for unload-reload behavior, which is known to over-predict damping at high strains, as shown in Figure 4.5. Kwok et al. (2008) discussed various methods for matching the modulus reduction and damping curves using codes that rely upon Masing's rules. In this report, we match the modulus reduction curve, and accept a misfit in hysteretic damping.

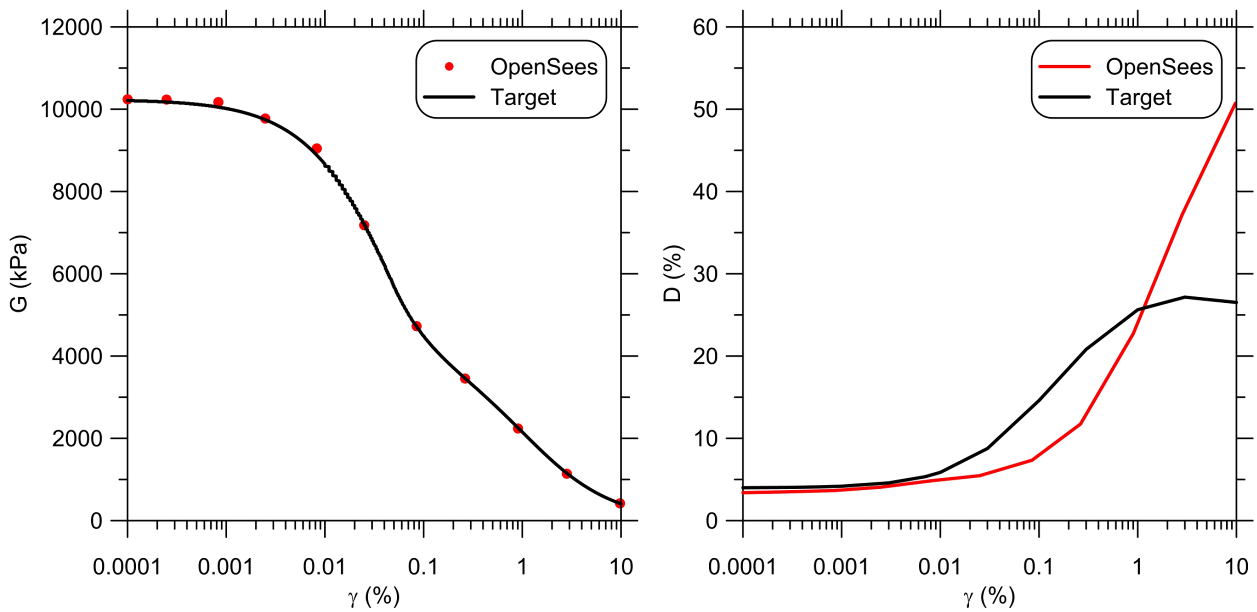

Figure 4.5 Shear modulus reduction and damping curves obtained from OpenSees compared to the target.

DeepSoil and OpenSees also have different approaches to modeling small-strain damping. DeepSoil provides an option to use a frequency-independent Rayleigh damping procedure (Hashash and Park 2004), a full Rayleigh damping procedure that permits specification of damping at two frequencies, and a simple Rayleigh damping procedure in which damping is matched at only a single frequency. We utilized the frequency-independent Rayleigh damping procedure despite its added computational cost. However, the frequency-independent algorithm is not implemented in OpenSees, and we therefore utilized full Rayleigh damping instead. The full Rayleigh damping equations are shown below.

$$a_0 = \frac{2.\xi_T.\omega_1.\omega_2}{\omega_1 + \omega_2} \tag{4.6}$$

$$a_1 = \frac{2.\xi_T}{\omega_1 + \omega_2} \tag{4.7}$$

$$\xi_R = \frac{a_0}{2.\omega} + \frac{a_1.\omega}{2} \tag{4.8}$$

where ξ_T is the target damping ratio and ω_1 and ω_2 are the angular frequencies associated with the target damping. The Rayleigh damping curves used in DeepSoil and OpenSees are shown in Figure 4.6.

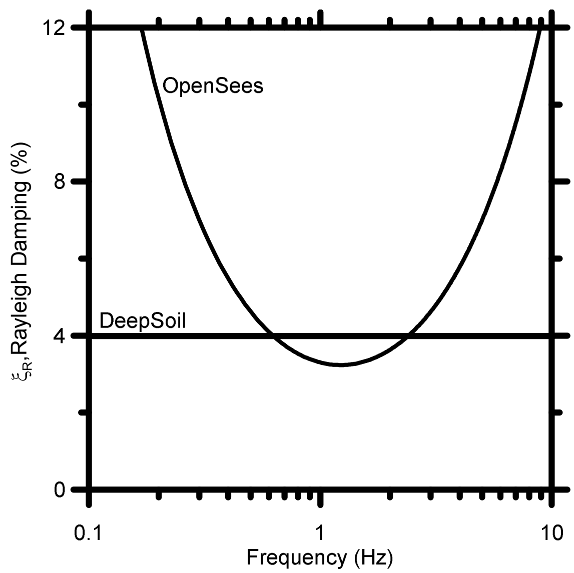

Figure 4.6 Rayleigh damping as a function of frequency

The numerical models utilized for the nonlinear site response analysis consist of 50 layers in order to capture the frequency content of the ground motions used in the study. Elements that are too large form a low-pass filter that prevents propagation of short wavelengths. The friction angle for the sand layers was set to 40°, which is reasonably consistent with estimates using Bolton's (1986) procedure, assuming a critical state friction angle of 32° for the Monterey sand.

4.5 SITE RESPONSE MODELING RESULTS

This section presents results for the site response modeling simulations compared with the test data. We first present computed and recorded time series, acceleration response spectra, and profiles of peak acceleration and peak shear strain for a single ground motion scaled to three different intensities. We then present residuals (defined as measured response minus predicted response) for spectral acceleration and other ground motion intensity measures.

4.5.1 Influence of Undrained Shear Strength

Time series and response spectra (5% damping) for three scaled versions of the WPI046-1994 Northridge Earthquake recording are shown in Figure 4.7. Measured data from AHA02 are compared with computed results from Models 1, 2, and 3. Models 1 and 2 consistently under-predict the surface motion, with the prediction error increasing as shaking intensity increases. Model 3 properly considers strain rate effects on undrained shear strength, whereas Models 1 and 2 use significantly smaller shear strengths. Profiles of peak acceleration and mobilized shear strain are shown in Figure 4.8. The larger motions produced peak shear strains in the soft clay on the order of 4% to 8%, which is essentially large enough to mobilize the strength of the clay. The lower strengths associated with Models 1 and 2 limited the transmission of ground motion, thereby resulting in an under-prediction of surface motion. On the other hand, Model 3 properly modeled the undrained strength by including strain rate effects, and correctly predicted the ground motion. The smaller motion mobilized shear strains on the order of 0.4% in the soft clay, which is too small to mobilize the undrained strength. However, this strain level is large enough that the shear strength has an influence on the stress-strain behavior, as illustrate by the Yee et al. procedure in Figure 4.2. Note that the mobilized shear strain (0.4%) is significantly higher than the transition shear strain (0.05%) applied using the Yee et al. procedure. An interesting observation is that none of the models predicted shear strains in the soft clay as high as the measured shear strain for the two larger motions, yet the ground motion predictions are reasonably consistent. A possible reason for this observation is that the shear strain levels mobilized in the simulations were still high enough to mobilize the undrained strength of the clay (e.g., 3 to 4% for the largest motion), and the ground acceleration is being limited by failure of the clay.

Two conclusions are drawn from the comparisons in Figures 4.7 and 4.8:

i. modeling shear strength correctly is important for predicting ground motion using nonlinear site response analysis, even if shear strains are not high enough to mobilize the shear strength, and

ii. strain rate significantly influences undrained shear strength in clay and should be included in site response simulations to avoid under-predicting ground motion.

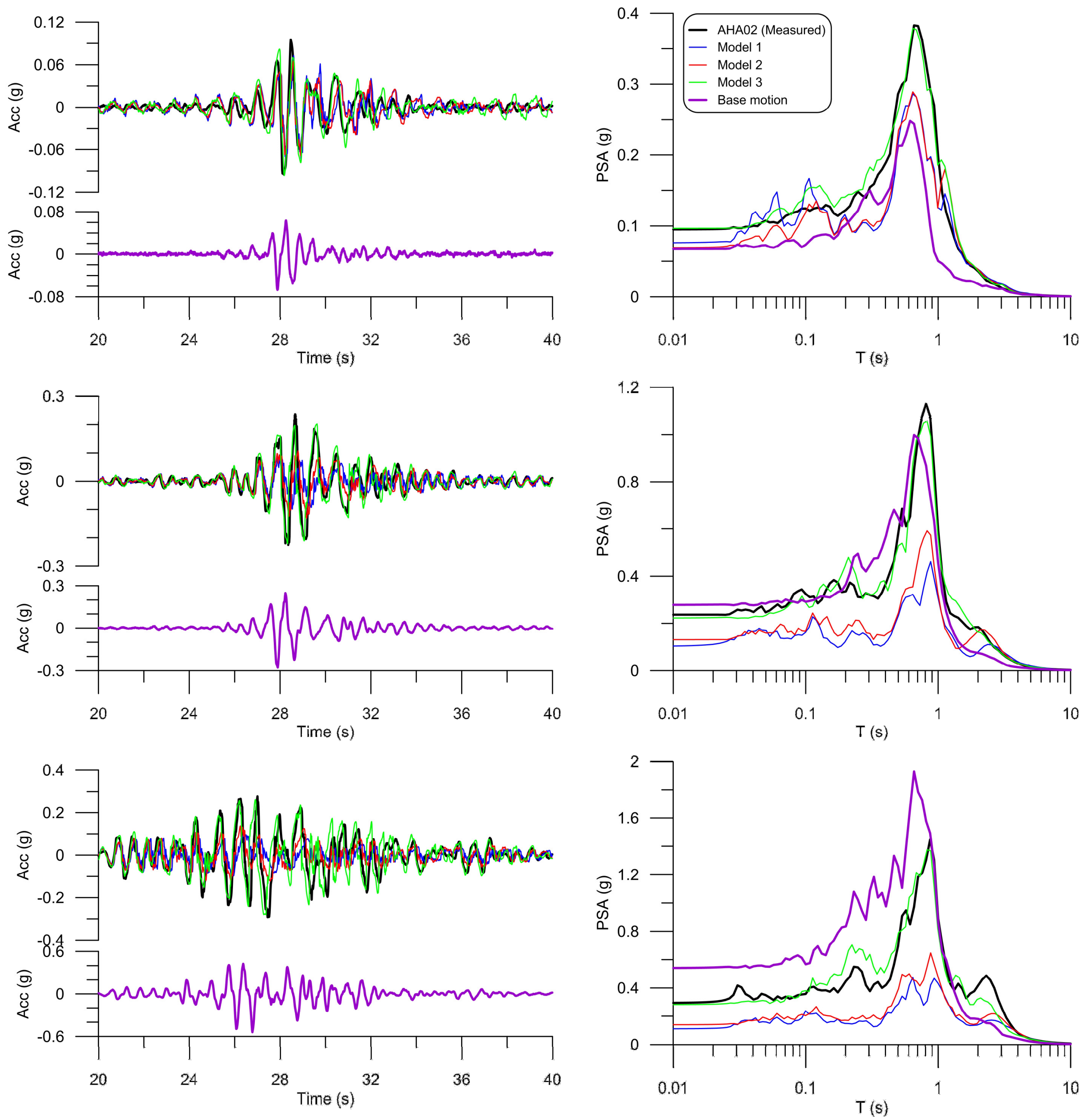

Figure 4.7 Example acceleration time series and spectral accelerations of surface motions for the centrifuge data and the nonlinear simulations

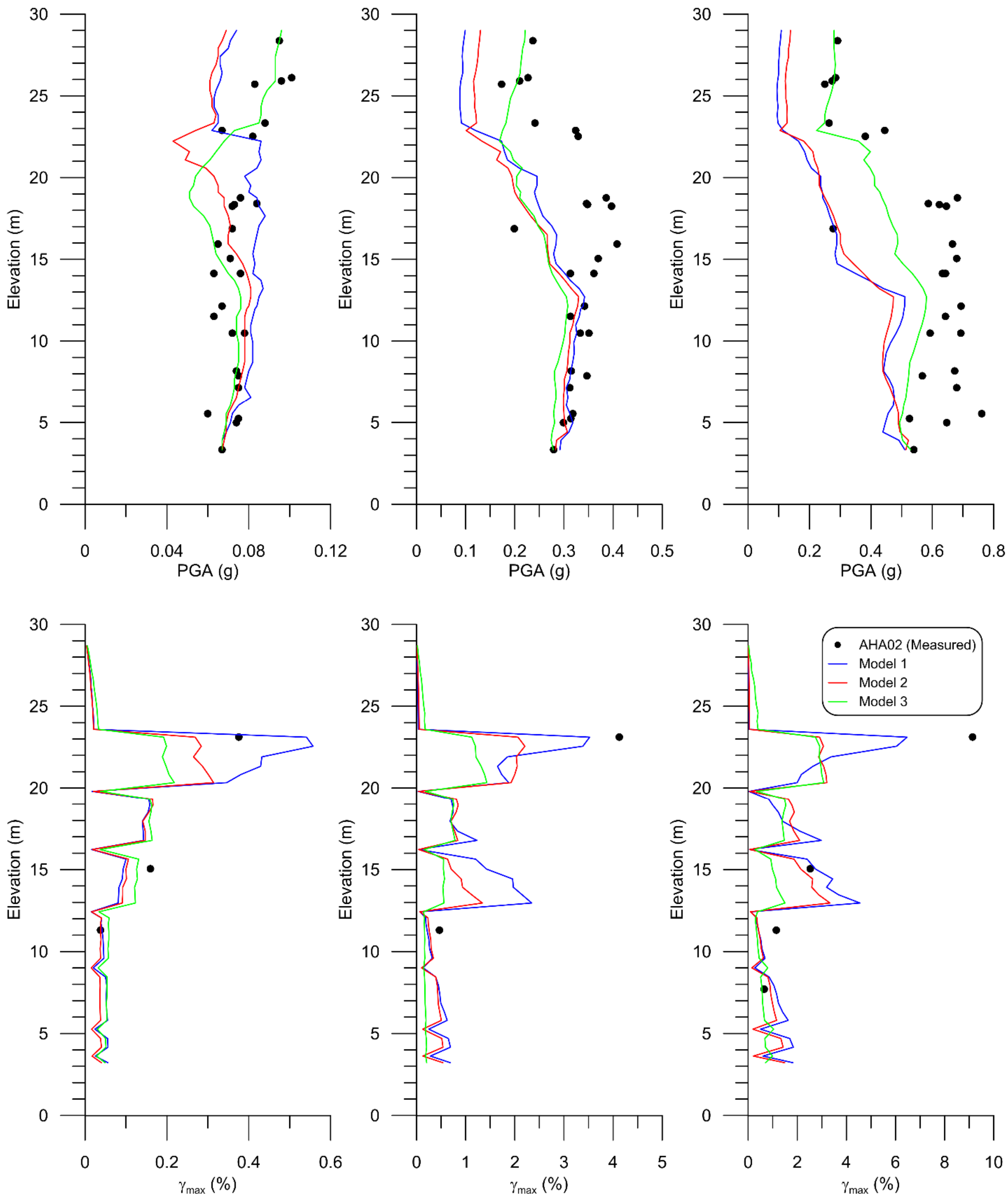

Figure 4.8 Peak horizontal acceleration and the maximum shear strain profiles for Model 1,2 and 3.

4.5.2 Comparison of DeepSoil and OpenSees

The same three ground motions are compared in Figures 4.9 and 4.10 using DeepSoil and OpenSees simulation platforms (Models 3 and 4). The results are very similar for all three motions, which indicates that differences between the simulation platforms do not significantly influence the outcome for this particular problem. The primary difference between the two analysis procedures is the hysteretic and small-strain Rayleigh damping formulations. DeepSoil is able to more accurately capture both sources of damping than the models implemented in OpenSees. In particular, we anticipated over-damping at high strain in the OpenSees model due to the Masing rule damping formulation. However, the strain levels mobilized in the OpenSees simulations are only on the order of 3% to 4%, which are associated with only modest differences between the target damping curve and the one achieved in OpenSees, and the differences may be offset by under-prediction of damping at smaller strains (see Figure 4.5).

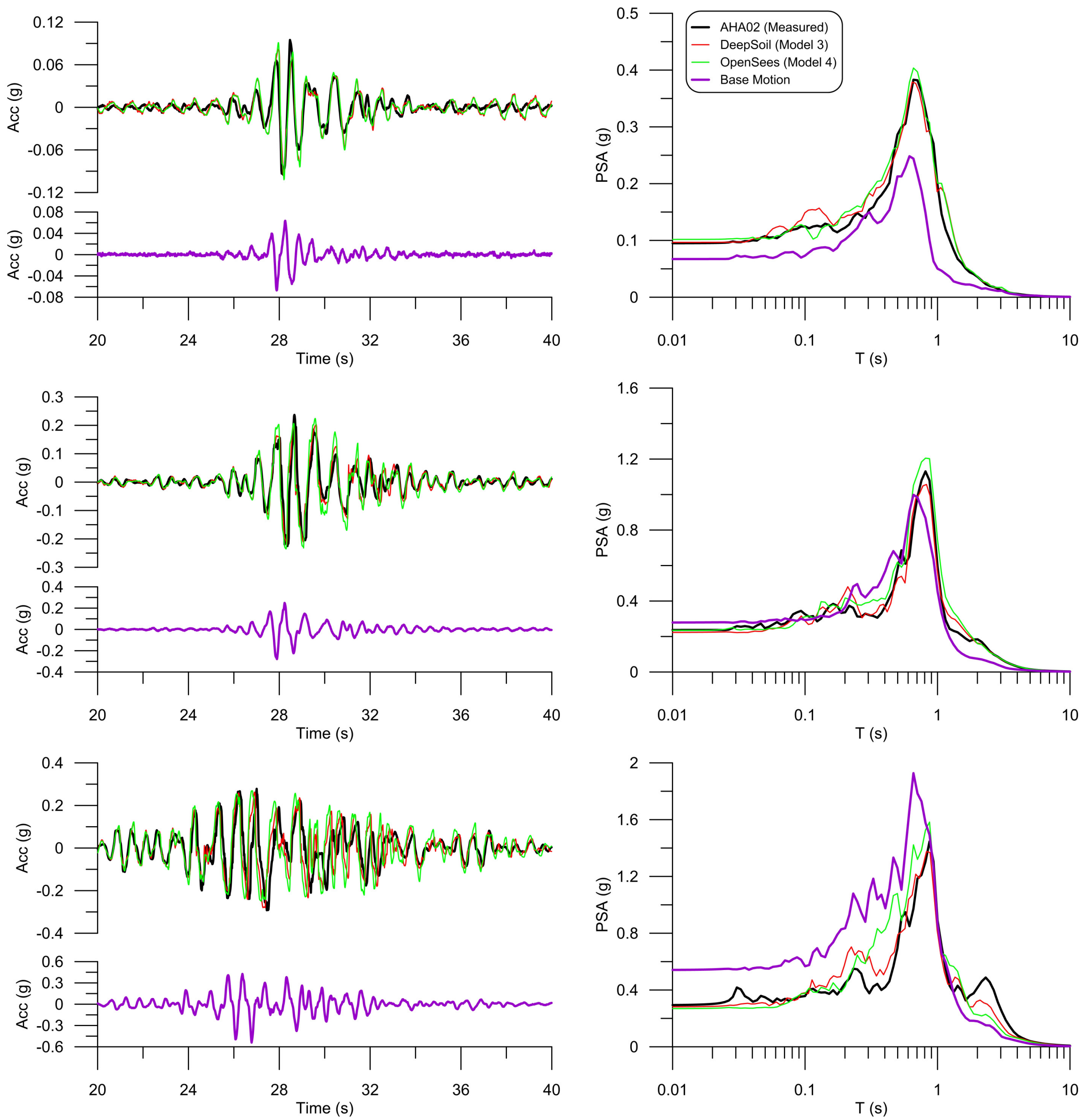

Figure 4.9 Example acceleration time series and spectral accelerations of surface motions for the centrifuge data and the nonlinear simulations using DeepSoil (Model 3) and OpenSees (Model 4).

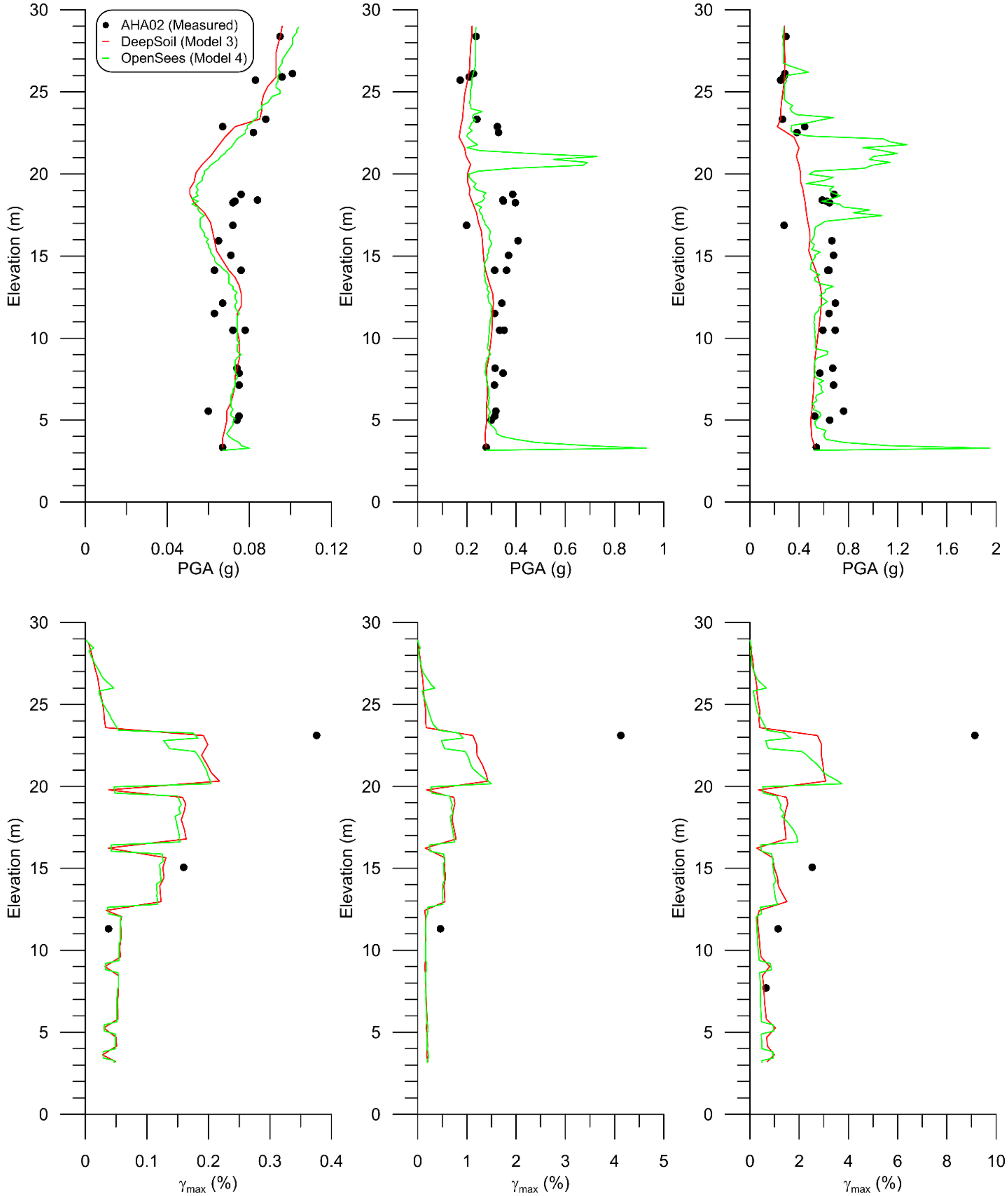

Figure 4.10 Peak horizontal acceleration and the maximum shear strain profiles for Model 3 and 4.

4.5.3 Comparison of Nonlinear and Equivalent Linear Simulations

A comparison between nonlinear (Model 3) and equivalent linear (Model 5) site response simulations, both following a modulus reduction curve with a 115% increase in shear strength for rate effects, are shown in Figures 4.11 and 4.12. The equivalent linear simulation agrees very well with the nonlinear simulation for the small motion, as anticipated since the largest differences are anticipated for larger motions and associated larger shear strains. The equivalent linear simulation tends to over-predict ground motion for the larger two motions. Interestingly, the equivalent linear simulation predicts larger strains than the nonlinear simulation in the softest clay layer. Errors in the equivalent linear approach are also readily apparent for the small cycles that proceed the large cycles during the ground motion, as illustrated in Figure 4.13. The phase and amplitude in this portion of the equivalent linear record do not match the measurements nearly as well as the nonlinear site response simulation. This observation is caused by the equivalent linear assumption that the secant shear modulus is constant for the entire record, whereas in reality it varies in time because strain amplitude varies in time. These errors in the equivalent linear site response simulations are subsequently demonstrated to cause errors in ground motion intensity measures that integrate ground motion in time (i.e., Arias intensity and cumulative absolute velocity).

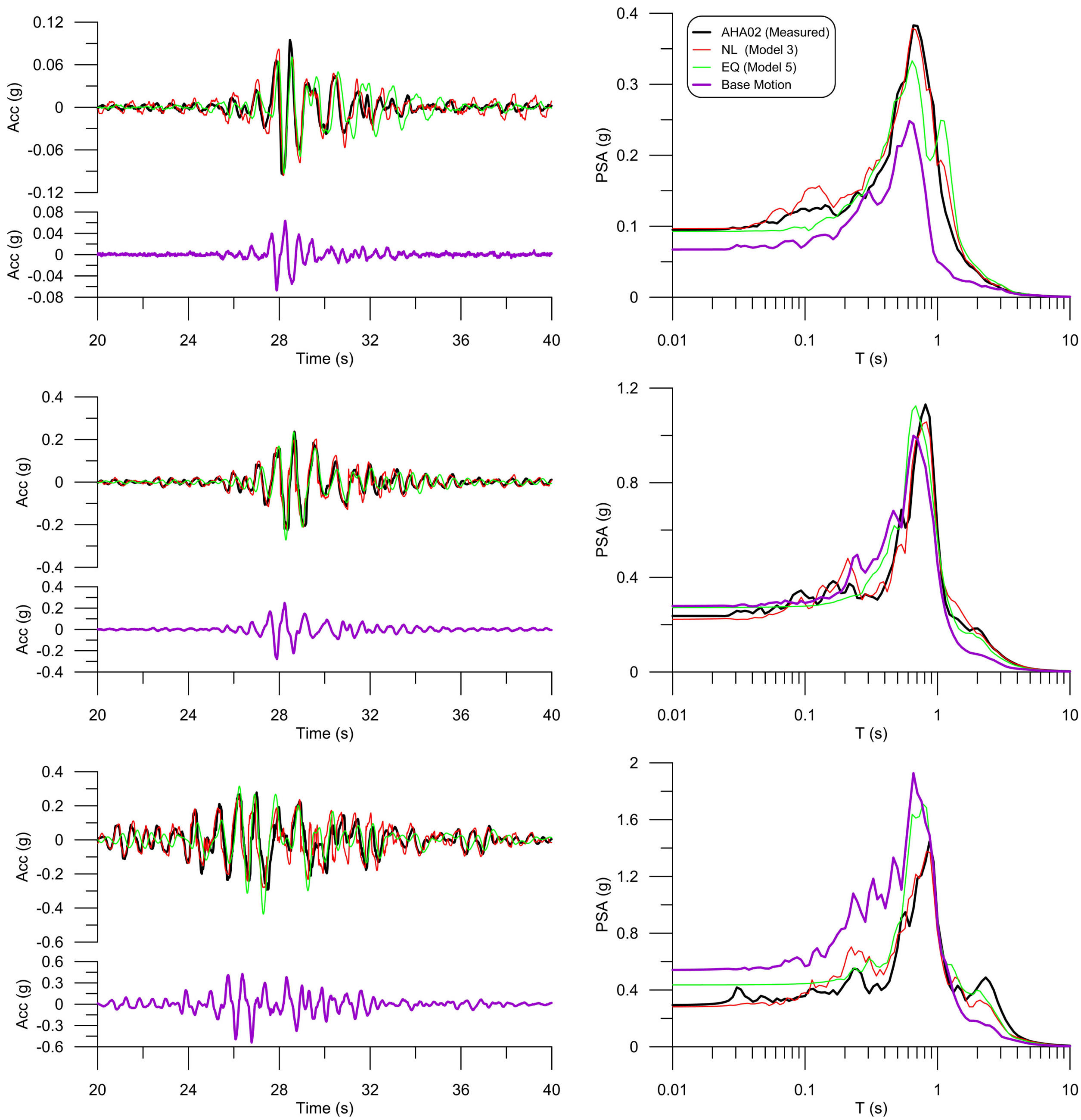

Figure 4.11 Example acceleration time series and spectral accelerations of surface motions for the centrifuge data and the nonlinear (Model 3) and equivalent linear (Model 5) simulations.

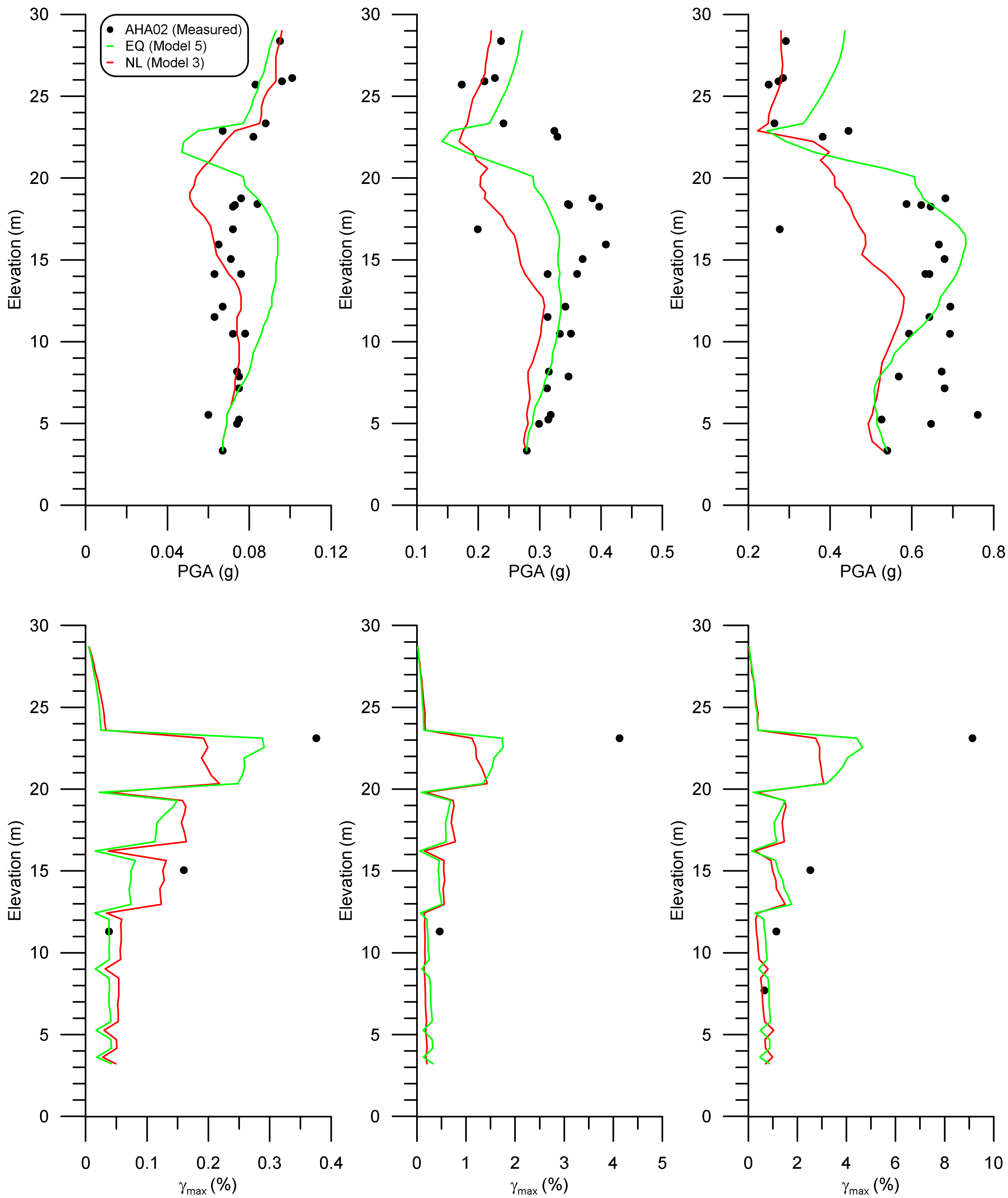

Figure 4.12 Peak horizontal acceleration and the maximum shear strain profiles for Models 3 and Model 5.

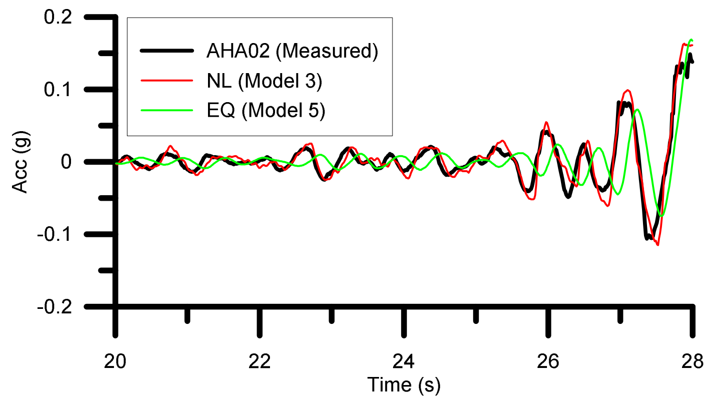

Figure 4.13 Zoomed-in view of the medium amplitude motion from Figure 4.11 showing the amplitude and phase errors in the small portion of motion for the equivalent-linear analysis.

4.5.4 Influence of strain rate correction

The influence of strain rate correction is shown in Figures 4.14 and 4.15 for Models 6 and 7, which utilize a 67% increase in strength following the Sheahan et al. (1996) finding rather than the measured 115% increase in strength. Decreasing the shear strength results in an under-prediction of ground motion for the nonlinear analysis (Model 7) and a slight reduction for the equivalent linear analysis (Model 6). The fact that Model 6 is actually improved by utilizing the incorrect shear strength is an indication that counterbalancing errors are in effect here. These figures indicate that obtaining the correct undrained strength is very important, and further illustrates that more work is needed to fully quantify rate effects over the full range of rates anticipated in site response studies.

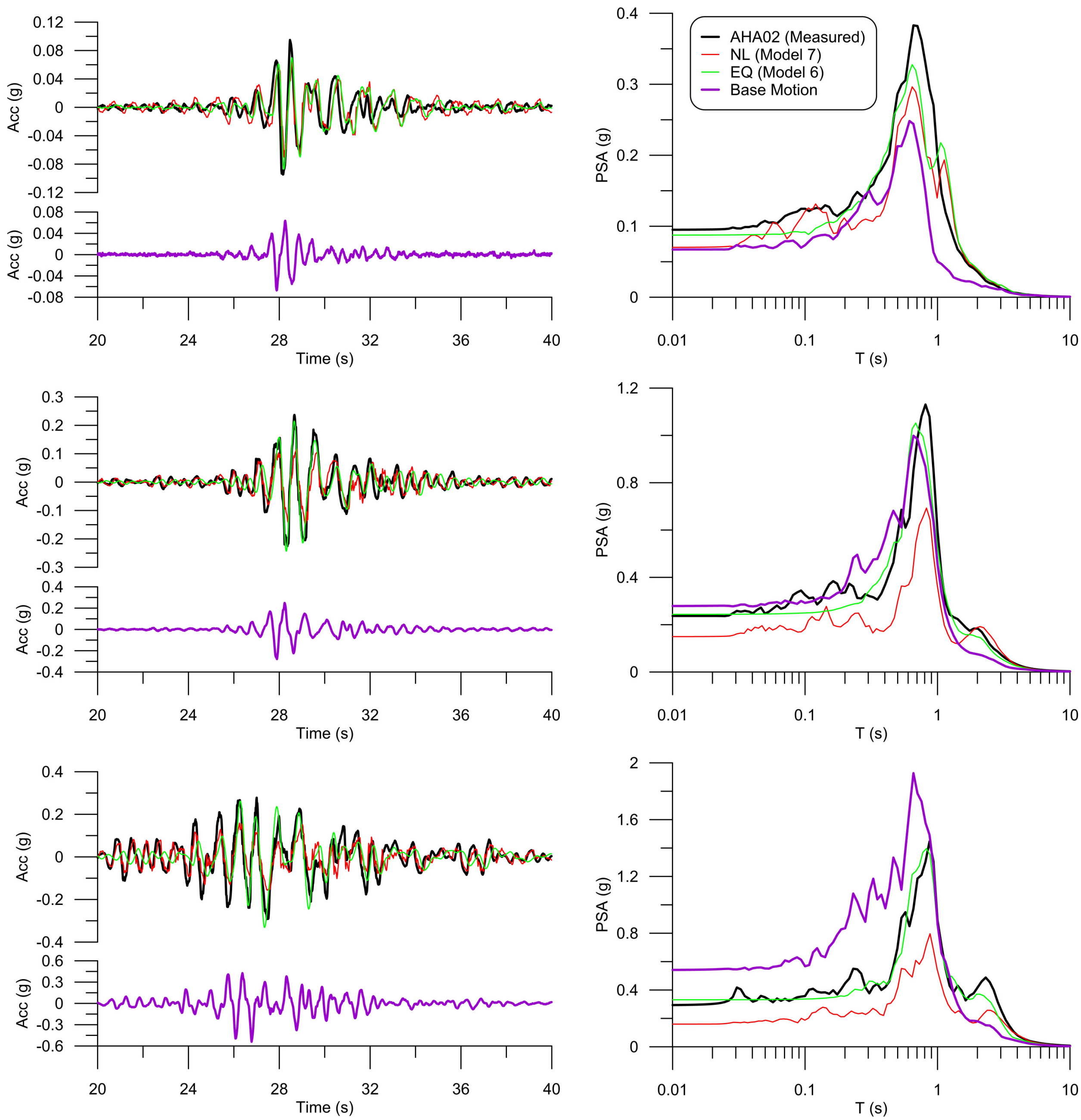

Figure 4.14 Example acceleration time series and spectral accelerations of surface motions for the centrifuge data and the nonlinear (Model 7) and equivalent linear (Model 3) simulations using a 67% increase in strength rather than the measured 115% increase in strength

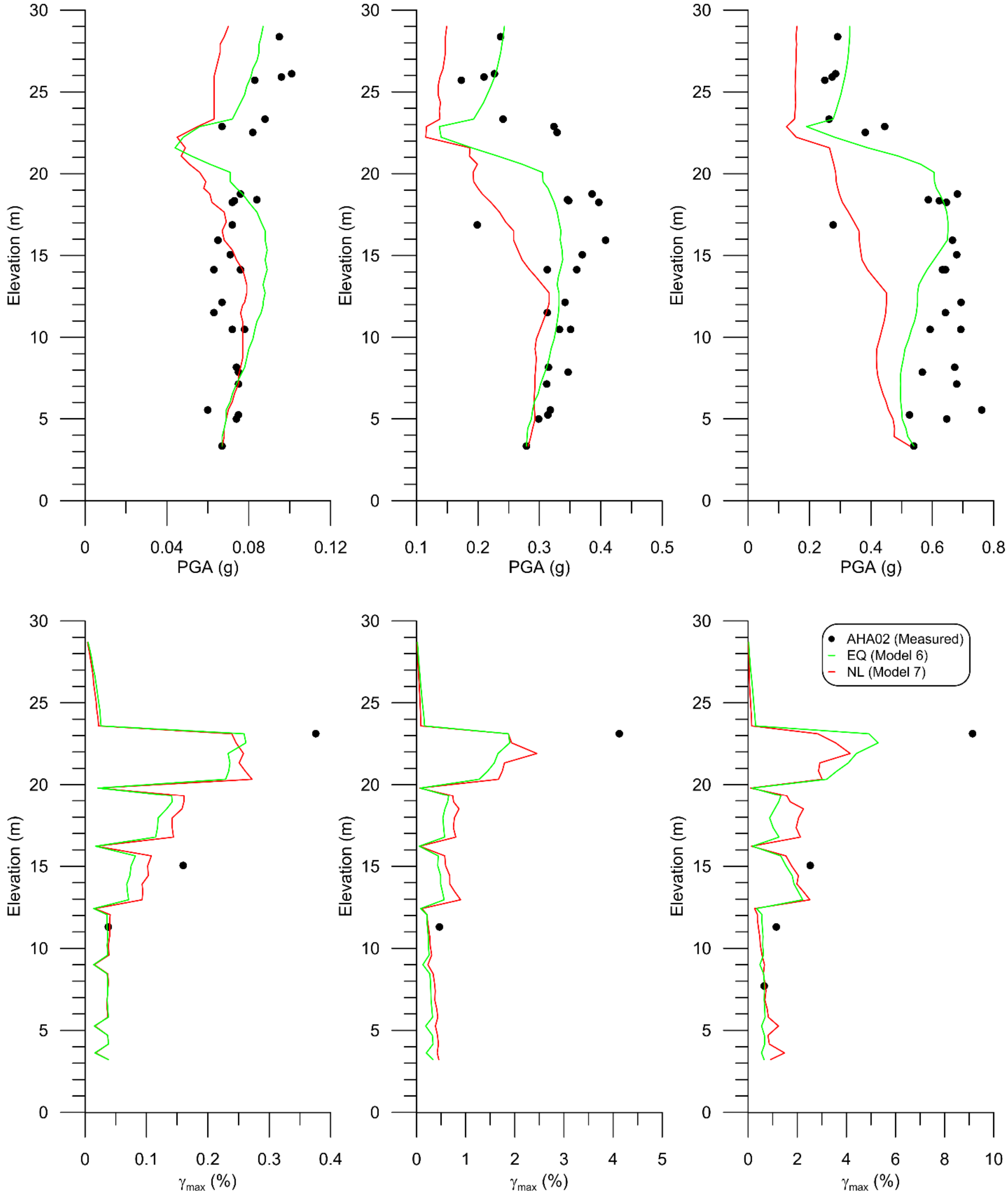

Figure 4.15 Peak horizontal acceleration and the maximum shear strain profiles for Models 6 and 7.

4.5.5 Residuals of Various Ground Motion Intensity Measures

Residuals of various ground motion intensity measures are presented in this section to demonstrate the overall accuracy of each site response modeling approach. Acceleration response spectra (5% damping) for the surface motion were computed for a period range from 0.01 to 10s, and residuals were computed by taking the difference in the natural log of spectral acceleration between the measurement and the prediction. A positive residual indicates an under-prediction of ground motion. The residuals are plotted with different symbols for small motions (peak base acceleration, PBA < 0.1g) and medium and large motions (PBA > 0.1g). The most accurate of all of the procedures is Model 3, which is the DeepSoil nonlinear site response analysis that uses the correct undrained shear strength. Second is the OpenSees nonlinear site response analysis that also uses the correct undrained shear strength. The third most accurate is Model 6, which is an equivalent linear analysis in DeepSoil using an undrained shear strength that is too low because the rate correction is only 67% rather than 115%. However, this model shows a general negative bias in the residuals, particularly at short period. The other models show significant bias, particularly for the medium and large motions. Differences among the models largely pertain to shear strength, so it makes sense that an erroneous assumption about shear strength will result in the most bias for large motions.

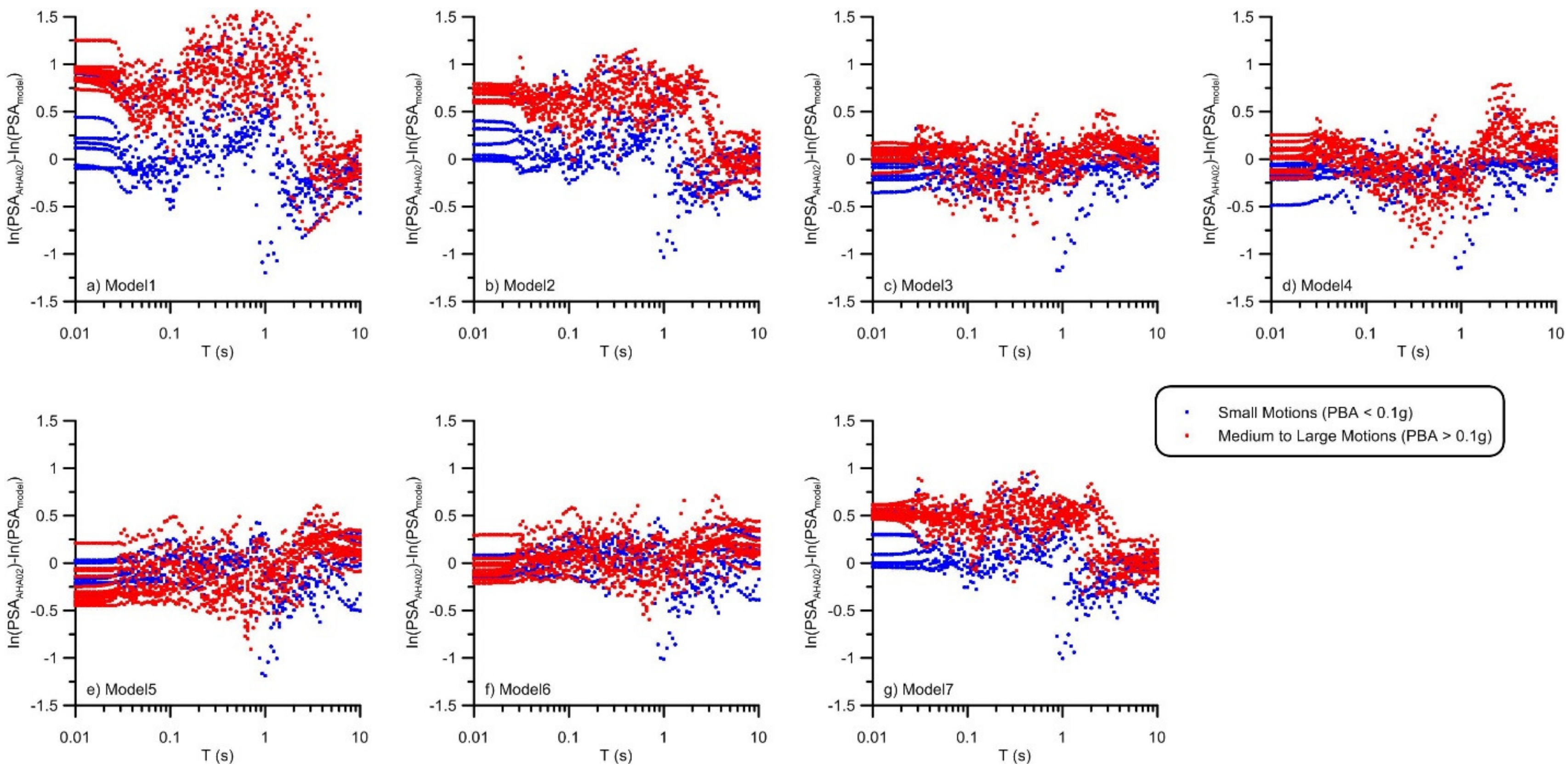

Figure 4.16 Residuals (measurement minus prediction) of the natural logarithm of spectral acceleration versus spectral period.

Residuals were also computed for Arias intensity and cumulative absolute velocity, as shown in Figures. 4.17 and 4.18. For both intensity measures, Models 3 and 4 again tend to be more accurate than the other models. However, more bias is apparent, as is a slight trend with PBA for small motions. The other models all exhibit significant trends in the residuals with PBA, indicating that they are likely to produce large errors in predictions of Arias intensity and cumulative absolute velocity. This may be an important finding since these intensity measures are increasingly being used to predict damage of earth structures such as earth dams.

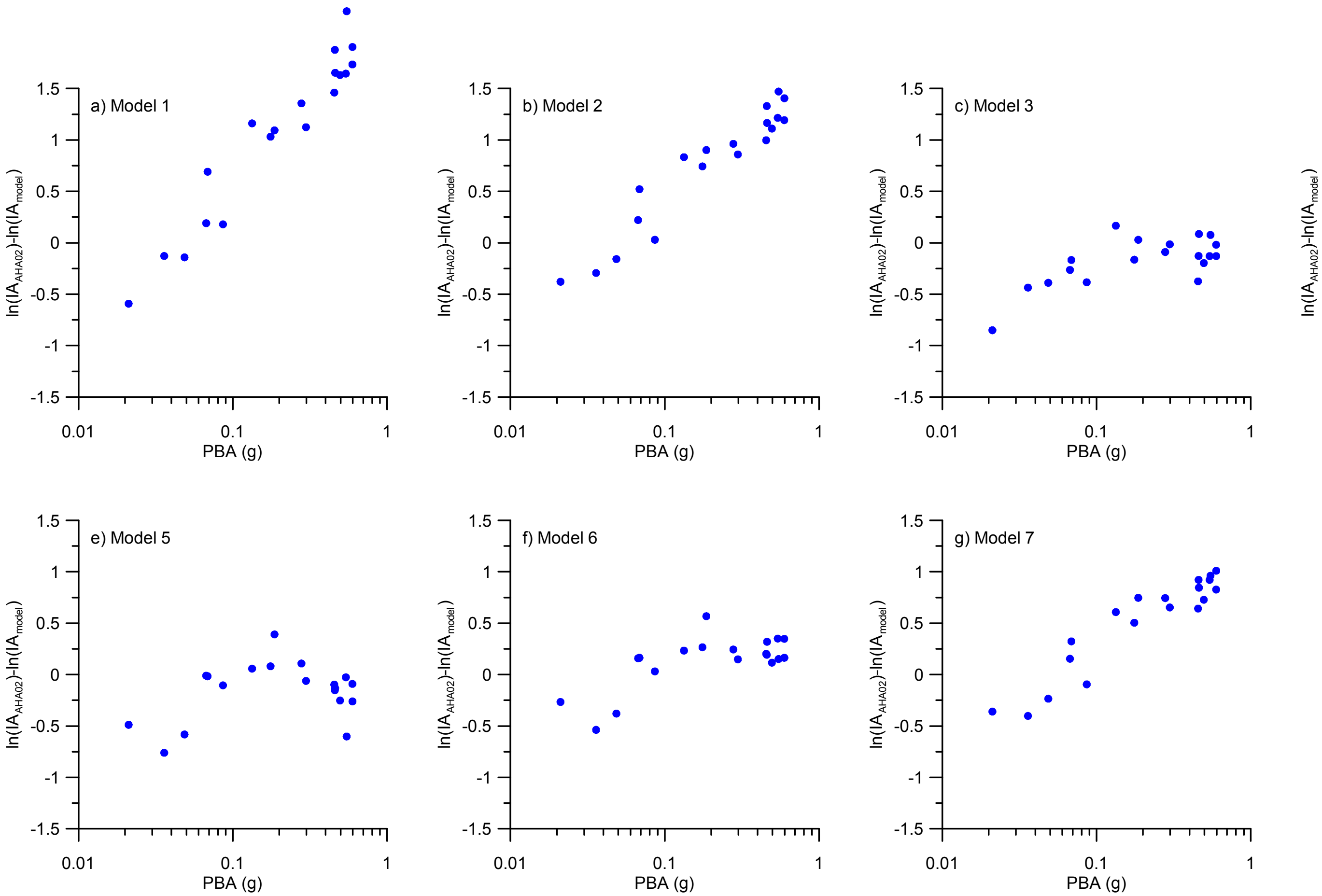

Figure 4.17 Residuals of Arias intensity (IA) versus peak base acceleration.

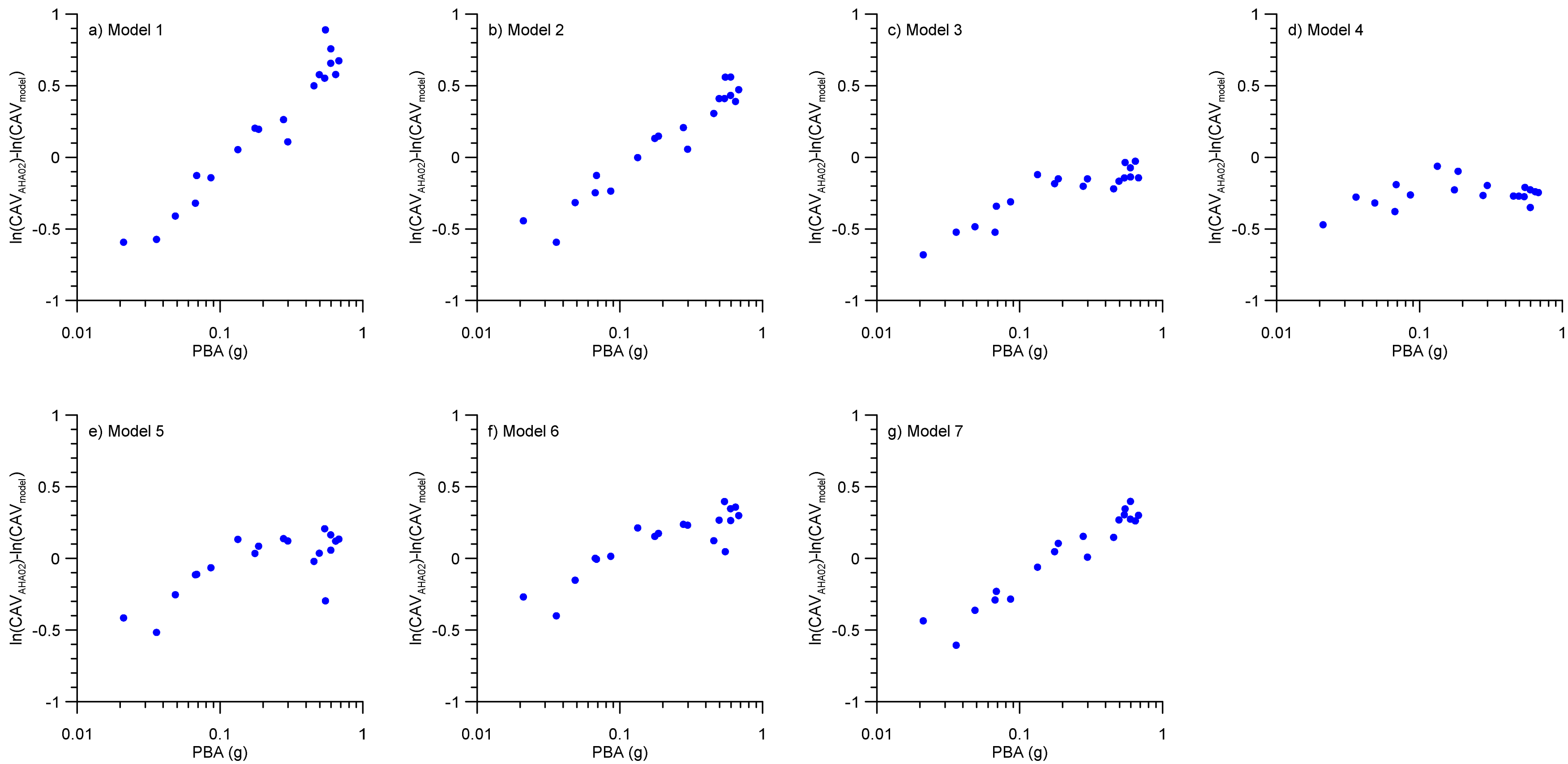

Figure 4.18 Residuals of cumulative absolute velocity (CAV) versus peak base acceleration.

5 EFFECTIVE STRESS NONLINEAR SITE RESPONSE ANALYSIS OF CENTRIFUGE MODELS INVOLVING LIQUEFACTION

This chapter focuses on effective stress nonlinear site response analysis of centrifuge models consisting of liquefiable sands to understand how well various models capture triggering and post-triggering ground motions. First, case studies and modeling studies will demonstrate that high-frequency high-acceleration pulses often propagate through liquefied soil profiles. These pulses are shown to be caused by the dilatant tendency of the liquefied sand being suppressed in undrained loading, causing a transient stiffening of the sand at high shear strains. Approaches for modeling the response of liquefied sand, including pore pressure generation models and advanced constitutive models, are then explained. Finally, the centrifuge tests are analyzed using various effective stress site response models, and comparisons between measurements and predictions are made.

5.1 MEASUREMENT OF ACCELERATION PULSES IN LIQUEFIED SAND

Liquefaction of cohesionless soils is widely acknowledged to exert an influence on earthquake ground motions. However, significant disagreements exist regarding the extent to which liquefaction attenuates or amplifies ground motion. A common argument made by many researchers is that liquefaction provides a "base isolator" effect that prevents propagation of vertical shear waves, thereby protecting overlying soil layers and sometimes preventing liquefaction of these layers (e.g., Martin and Qiu 2001). The "base isolator" effect, however, does not agree with observations of high frequency and sometimes high amplitude acceleration pulses that propagate through liquefied soil. Such observations have been made in strong motion records in the field, in physical modeling studies, and in numerical simulations that utilize constitutive models that properly capture dilatancy. In this chapter we seek to demonstrate that the "base isolator" effect is an erroneous outcome of a simplifying assumption made in the modeling of pore pressure generation in certain types of effective stress site response codes, and we show that proper treatment of dilatancy using advanced constitutive models can capture the high frequency high amplitude acceleration pulses.

Perhaps the most well-known recording of ground motion and pore pressure during earthquake-induced liquefaction is the Wildlife Liquefaction Array recordings from the 1987 Superstition Hills earthquake. Acceleration and pore pressure recordings clearly documented liquefaction at the site. Figure 5.1 shows the north-south acceleration recorded at the surface and 5.7m deep, and a pore pressure measurement in the liquefiable material (Holzer and Youd, 2007). The acceleration amplitude and frequency content tend to decrease with the buildup of significant excess pore pressure, with the exception of several high-frequency, moderate amplitude acceleration spikes late in the record. For example, a high frequency 0.1g spike is apparent in the surface acceleration measurement at about time = 54s, which corresponds to a similarly sharp drop in the pore pressure record. This response occurred after development of significant pore pressures, and clearly demonstrates that liquefied sand is not a soft, weak base isolator and that at least moderate ground shaking can propagate through liquefiable soil.

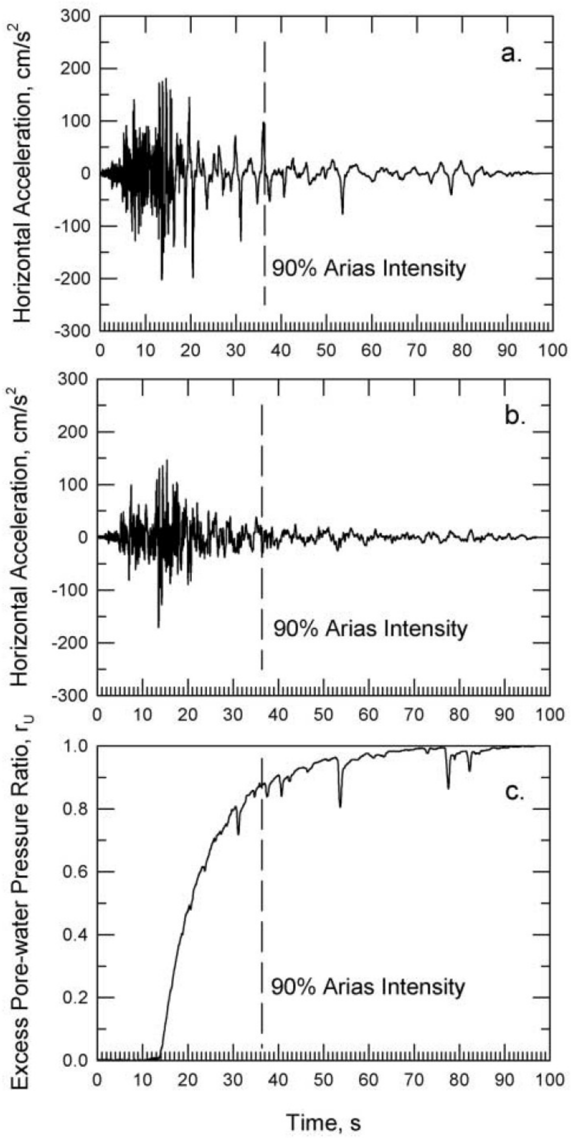

Figure 5.1 Wildlife liquefaction data recorded during 1989 Superstition Hills Earthquake (Holzer and Youd 2007).

Evidence of this phenomenon is also provided by the NIG018 N/S record in Kashiwazaki from the 2007 Niigata Ken Chuetsu-Oki earthquake (Kayen et al. 2007) shown in Figure 5.2. The strong motion station rests on an alluvial sand deposit with SPT blow counts around 20 at depths of about 5 to 9m (just below the water table) and denser materials at depth. The peak surface acceleration recorded at the site was 0.7g, producing estimated CSR>0.4, and placing the sand clearly on the "liquefaction" side of the Seed and Idriss (1971) simplified procedure (or any other triggering procedure for that matter). Surface evidence of liquefaction was found at sites very near the recording station.

Figure 5.2 shows the acceleration records and acceleration response spectra for two ground motion records both obtained on the surface projection of the fault plane (R_{jb} = 0). The primary difference in these records is the site conditions; the NIG018 site was susceptible to liquefaction whereas the 65039 site was not. The NIG018 acceleration record clearly shows large-amplitude acceleration spikes. Unlike the Wildlife site, where the high-frequency acceleration spikes were smaller than the peak horizontal acceleration, the peak horizontal acceleration in this case occurred during one such spike and is directly attributed to the undrained response of soil during cyclic loading. Hence, the high-frequency spikes are not merely an interesting academic artifact of liquefied soil behavior, but rather control the peak ground motions. To demonstrate this point further, the 65039 ground motion on non-liquefied ground was significantly lower. The 65039 station response spectrum has a fairly typical shape with a pronounced peak at about 0.3s, whereas the NIG018 response spectrum contains a very broad band over which spectral accelerations are high, and does not exhibit the characteristic low-period peak. The broad band in the NIG018 spectrum can be explained by the impulse-like acceleration pulses. Impulses exhibit a flat frequency response, and would therefore be expected to cause a broad band acceleration response spectrum. The difference between the 65039 and NIG018 records may be partially attributed to path effects or site effects that are unrelated to liquefaction, but the dilatant behavior of sand in undrained loading clearly played a role in the observed motions at the NIG018 site, and the liquefied sand clearly did not act as a "base isolator". In fact, the NIG018 station recorded the largest peak horizontal acceleration and velocity of any K-net station during the earthquake.

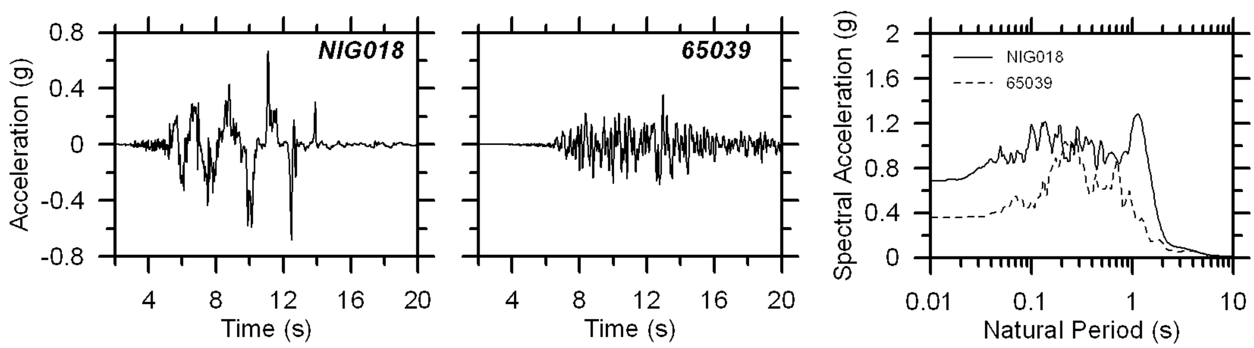

Figure 5.2 Ground motions from a site that liquefied (NIG018) and did not liquefy (65039) during 2007 Niigata Ken Chuetsu Oki earthquake. Both recording stations were on the surface projection of the fault plane (R_{jb} = 0).

A final example of this behavior from a centrifuge test is shown in Figure 5.3, where peak accelerations of more than 1g were observed during strong shaking, and were clearly related to the recorded drops in pore pressure (Brandenberg et al., 2005). The acceleration amplitude was large enough to cause the capacitive accelerometer to "clip", meaning that its capacity was exceeded and it exhibited a capacitive decay in voltage. The acceleration pulses correspond to transient reductions in pore pressure ratio, which is similar to the Wildlife Liquefaction Array response, though the acceleration pulses and transient pore pressure reductions are more pronounced.

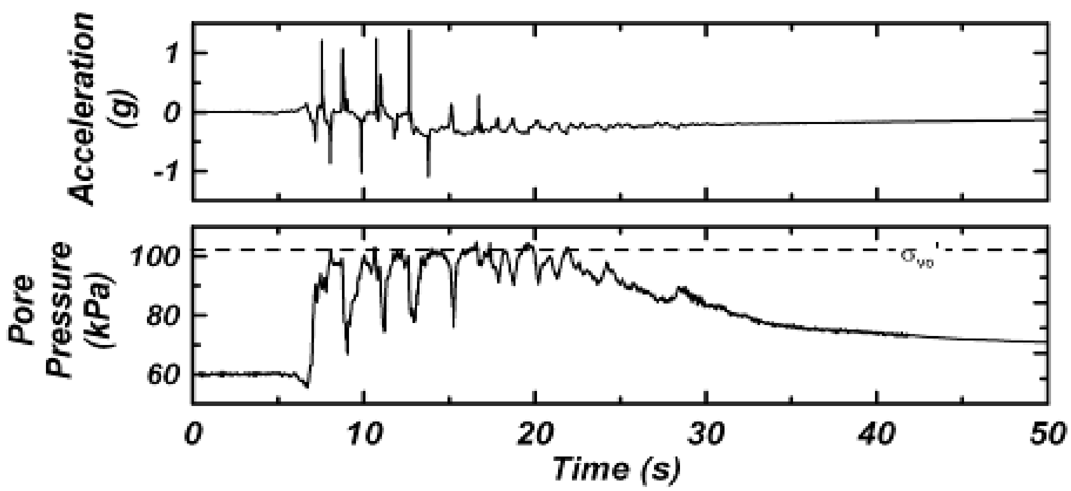

Figure 5.3 Acceleration and pore pressure record in liquefied sand from centrifuge test (Brandenberg 2005).

5.2 EXPLANATION OF ACCELERATION PULSES IN LIQUEFIED SAND

The presence of large-amplitude high-frequency spikes of acceleration in ground motions from liquefiable sites may seem surprising based on the assumption that liquefied sand is very weak, but is not surprising considering the well-known influence of dilatancy on undrained stress-strain behavior of sands. Figure 5.4 shows a stress-controlled cyclic triaxial test on Sacramento River sand conducted by Boulanger and Truman (1996). The sand gradually softens and eventually reaches a state of zero effective stress, i.e., $p'/p_c'=0$, at which point the sand does indeed exhibit a very low shear modulus. However, the liquefied sand does not remain soft and weak after reaching this state. Rather, the stress-strain response exhibits a strain-hardening behavior in which the tangent shear modulus increases as strain increases, exhibiting an inverted S-shaped stress-strain behavior that has been observed in many other cyclic undrained tests on sands and non-plastic silts. The stress path follows the critical state line in q/p' space, forming the characteristic butterfly shape. The strain-hardening behavior is caused by the dilatant tendency of the sand being suppressed in undrained loading.

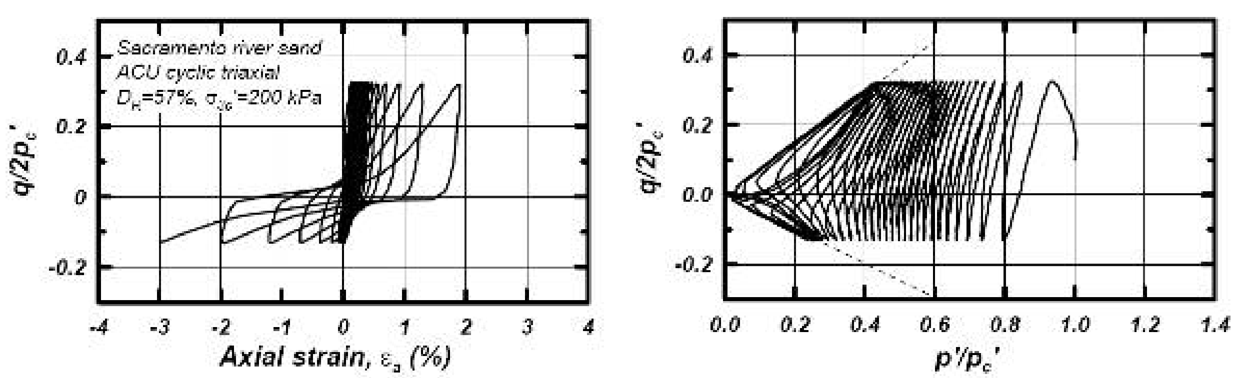

Figure 5.4 Cyclic triaxial test on saturated Sacramento River sand (Boulanger and Truman 1996).

The sudden increase in effective stress due to dilatancy results in an increase in shear modulus, which enables propagation of wave energy through the soil. This wave energy results in increased shear strains in overlying layers, and a high frequency high amplitude pulse of acceleration propagates through the sand. These waves have been called de-liquefaction shock waves by Kutter and Wilson (1999). Dilatancy of liquefied sand is clearly important for modeling the high frequency acceleration pulses. However, dilatancy is not modeled in some effective stress site response models that are currently used to predict ground motions in liquefying soil profiles. I now turn our attention to explaining modeling assumptions made in various classes of nonlinear effective stress site response models.

5.3 PORE PRESSURE GENERATION MODELS

Early pore pressure generation models proposed by Seed et al (1975) and Booker et al (1976) provided an empirical relationship between excess pore pressure ratio, r_u (excess pore pressure normalized by initial confining stress), and number of loading cycles, N (Eq. 5.1).

$$r_u = \frac{2}{\pi} sin^{-1}\left[\left(\frac{N}{N_{liq}}\right)^{\frac{1}{2\theta}}\right] \tag{5.1}$$

$$r_u = \frac{u_x}{\sigma'_{co}} \tag{5.2}$$

In Eqs. 5.1 and 5.2, θ is a calibration parameter, N_{liq} is the number of cycles required to initial liquefaction, u_x is excess pore pressure, and σ'_{co} is the initial consolidation stress. Both θ and N_{liq} can be determined from stress controlled cyclic triaxial tests. The calibration parameter θ is dependent on test conditions and the soil type whereas N_{liq} is related to loading intensity and relative density. This equation is intended to capture the low-frequency increase in excess pore pressure ratio, and neglects the transient cycling of excess pore pressure that accompanies undrained laboratory testing.

Matasovic (1992) suggested a functional form for pore pressure generation that is based on accumulation of strain above the volumetric threshold shear strain:

$$r_u = \frac{p.f.F.N_c.\left(\gamma_{ct} - \gamma_{tvp}\right)^s}{1 + f.F.N_c.\left(\gamma_{ct} - \gamma_{tvp}\right)^s} \tag{5.3}$$

In Eq. (5.3), *p*, *F* and *s* are the curve fitting parameters and *f* is the parameter that represents the directional pore pressure generation. f is 1 for 1-D condition and 2 for 2-D conditions. The threshold shear strain for initiation of volumetric strain, γ_{tvp}, is between 0.01% to 0.02% and there is no significant pore pressure generation expected for shear strains below this threshold. For soil at the Wildlife Liquefaction Array, the curve fitting parameters were found as p=1.04, F=2.6 and s=1.7.

The excess pore pressure generations results in a reduction of soil strength and the reduction is represented by degradation index, δ_t, where v=3.5-5.0 and it is 3.8 for Santa Monica beach sand.

$$\tau^* = \tau_0.\delta_t = \tau_0.\left[\left(1 - u_N\right)^v\right] \tag{5.4}$$

An example strain controlled simulation using the Matasovic pore pressure generation model is shown in Figure 5.5. A cyclic shear strain with amplitude of 0.05% is imposed on the model, and the pore pressure generation function is computed using Eq. (5.3). The updated stress amplitude for each cycle was computed using Eq. (5.4), and the stress-strain loops were generated accordingly. Note that the excess pore pressure ratio increases monotonically during loading, which is consistent with the modeling assumption. In reality, transient oscillations would be present in the pore pressure response due to dilatancy of the sand.

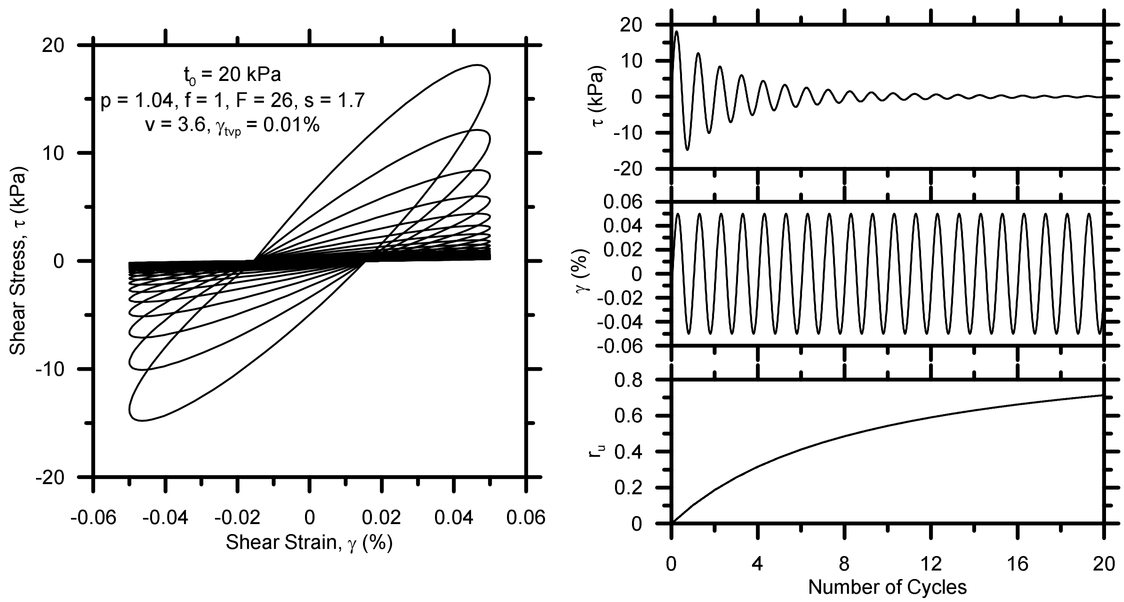

Figure 5.5 Numerical simulation of undrained strain-controlled test using pore pressure generation function by Matasovic (1992).

Pore pressure generation models have also been formulated based on the hysteretic energy dissipated per unit volume of soil. Dissipated hysteretic energy normalized by initial confining pressure, W_s, was used by Green et al (2000) to develop the following pore pressure generation model:

$$r_u = \sqrt{\frac{W_s}{PEC}} \tag{5.5}$$

where W_s is

$$W_s = \frac{1}{2\sigma_0'} \sum_{i=1}^{n-1} (\tau_{i+1} + \tau_i)(\gamma_{i+1} - \gamma_i) \tag{5.6}$$

PEC is a calibration parameter that represents the "pseudo energy capacity" and can be determined from cyclic tests. It was empirically derived as:

$$PEC = \frac{W_{s,r_u=0.65}}{0.4225} \tag{5.7}$$

In 2008, Polito et al modified the calibration parameter and expressed it as follows:

$$In(PEC) = \{\exp(c_3 D_R) + c_4\} \qquad \text{for FC<35\%} \tag{5.8a}$$

$$In(PEC) = \{c_1 FC^{c_2} + \exp(c_3 D_R) + c_4\} \qquad \text{for FC}\geq 35\% \tag{5.8b}$$

The energy-based pore pressure generation modeling approach is similar to the strain-based modeling approach in that the excess pore pressure ratio increases monotonically and never oscillates due to dilatancy. A fundamental difference between the strain-based and energy-based approaches is that the strain-based approach permits pore pressure generation only when the strain amplitude exceeds the volumetric threshold shear strain, γ_{tvp}. Soil dissipates hysteretic energy at strains lower than γ_{tvp}, yet pore pressure has not been observed to develop at such low strains. However, pore pressures would be predicted by the energy-based procedure at strains lower than γ_{tvp}.

5.4 ADVANCED CONSTITUTIVE MODELS

A thorough review of advanced constitutive models is beyond the scope of this chapter, and we focus on the ability of the models to capture dilatancy, which bears particular importance for undrained site response analysis in liquefied soils. Different approaches to modeling this behavior include multiple yield surface models (e.g., Elgamal et al. 2003) in which the tangent stiffness is controlled by nested yield surfaces that translate and rotate in stress space, and bounding surface models (e.g., Dafalias and Manzari 2004, Boulanger and Ziotopolou 2012) in which tangent modulus is a function of the distance between the current stress point and a bounding surface. Both modeling approaches can capture the strain-stiffening behavior that is associated with dilatancy of the sand being suppressed during undrained loading, as shown in Figures 5.6 and 5.7. This behavior has been measured during many stress-controlled cyclic laboratory tests. It is not always apparent in constant-amplitude strain-controlled cyclic laboratory tests because the dilatant tendency occurs when the shear strain exceeds the maximum past shear strain, which never happens during constant-amplitude strain controlled tests. Earthquake ground motions generate a complex loading path that is neither stress-controlled nor strain-controlled, and it is therefore important that stress-strain models are able to capture the dilatant tendency.

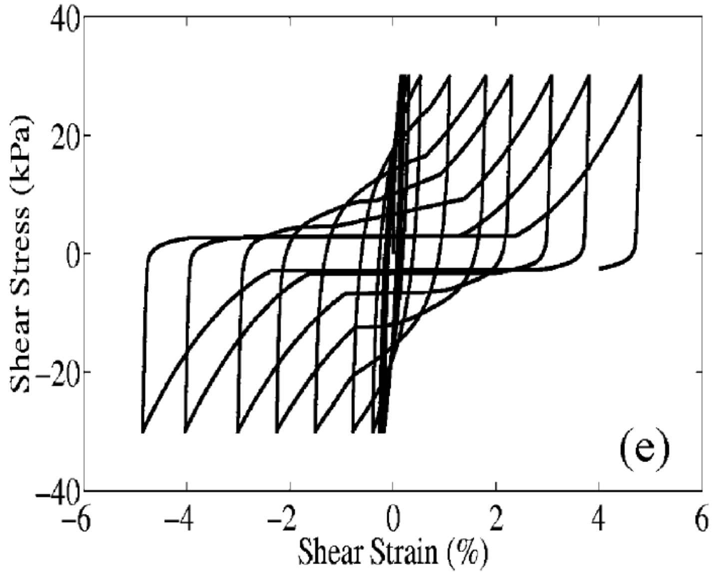

Figure 5.6 **Multiple yield surface plasticity model undrained stress-strain behavior (Elgamal et al. 2003).**

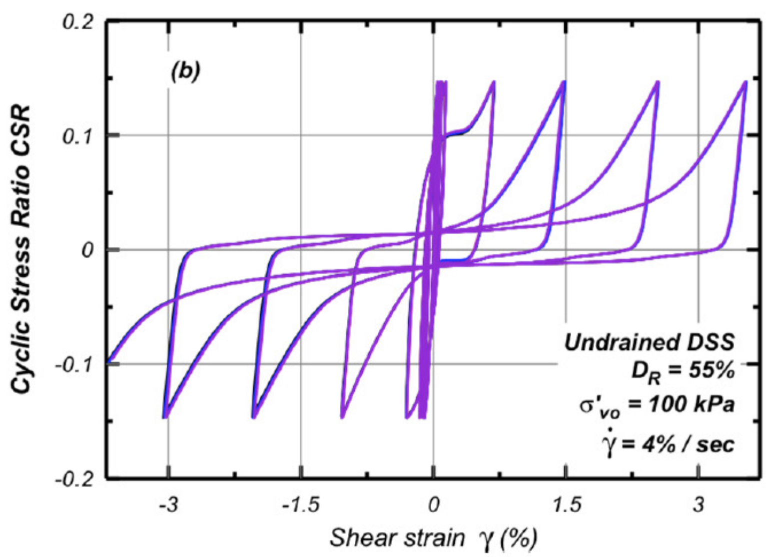

Figure 5.7 **Bounding surface plasticity model undrained stress-strain behavior (Boulanger and Ziotopolou 2012).**

5.5 DESCRIPTION OF CENTRIFUGE MODEL CSP3

A centrifuge modeling program presented by Wilson et al. (2000) is utilized in this chapter to compare the different effective stress modeling approaches. Model CSP3 (Figures 5.8 and 5.9) consists of a medium dense layer of sand (D_R = 55%) overlying dense sand (D_R = 85%) with the groundwater table at the surface. The model was constructed in a shear beam container consisting of steel and aluminum rings separated by flexible rubber layers. A variety of deep foundations were installed in the model, but we focus our attention on a "free-field" array of sensors that are far enough from any of the foundations to minimize interaction effects between the deep foundations and the soil. The model was shaken by a sequence of ground motions, and the large input motions liquefied the medium dense sand layer. We focus our attention in this manuscript on the large ground motions that liquefied the soil to observe the ability of nonlinear effective stress site response codes to

i. capture the buildup of pore pressure and liquefaction triggering, and
ii. model the post-liquefaction acceleration pulses associated with dilatancy of the sand.

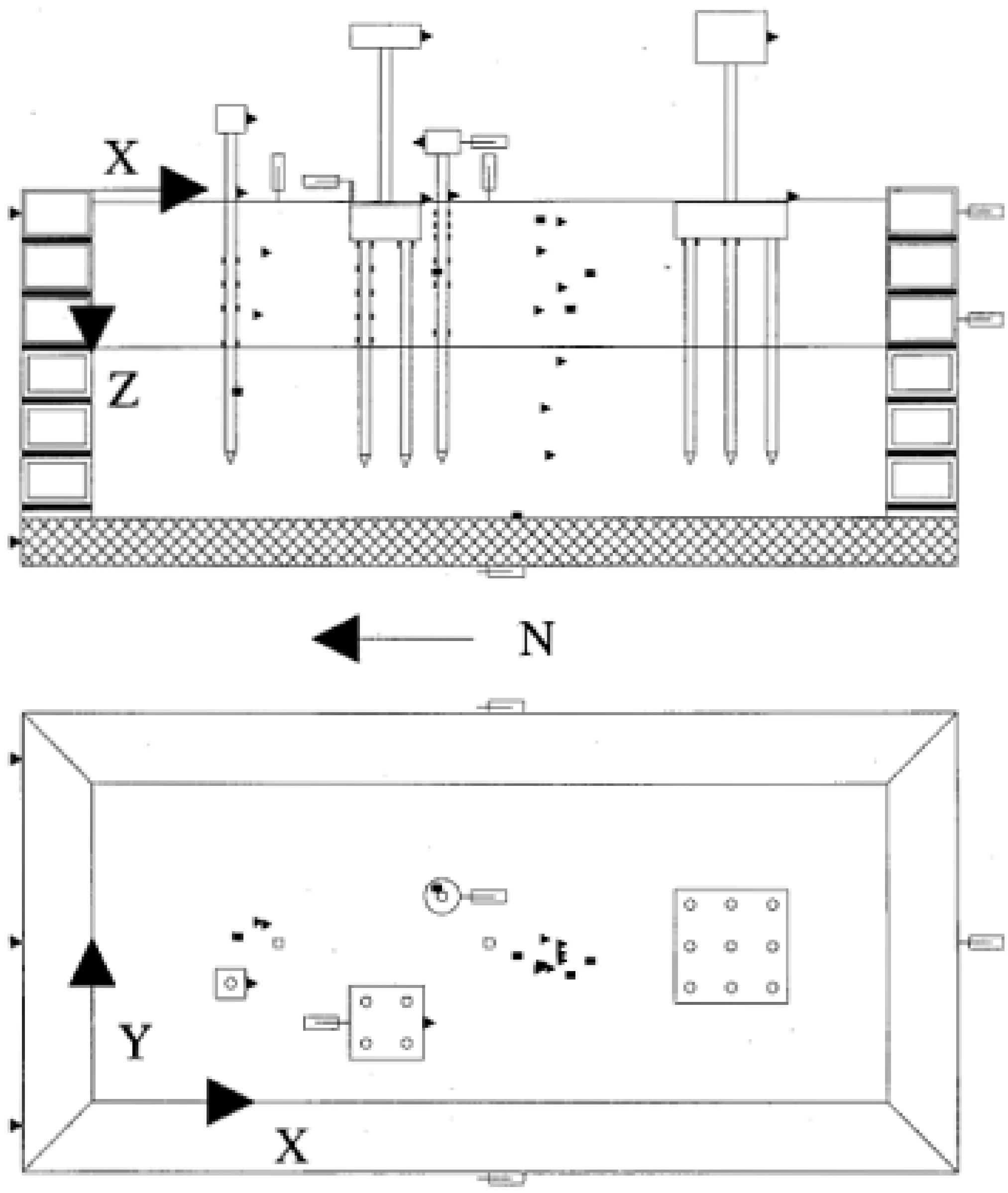

Figure 5.8 Configuration of model CSP3 (Wilson et al. 2000).

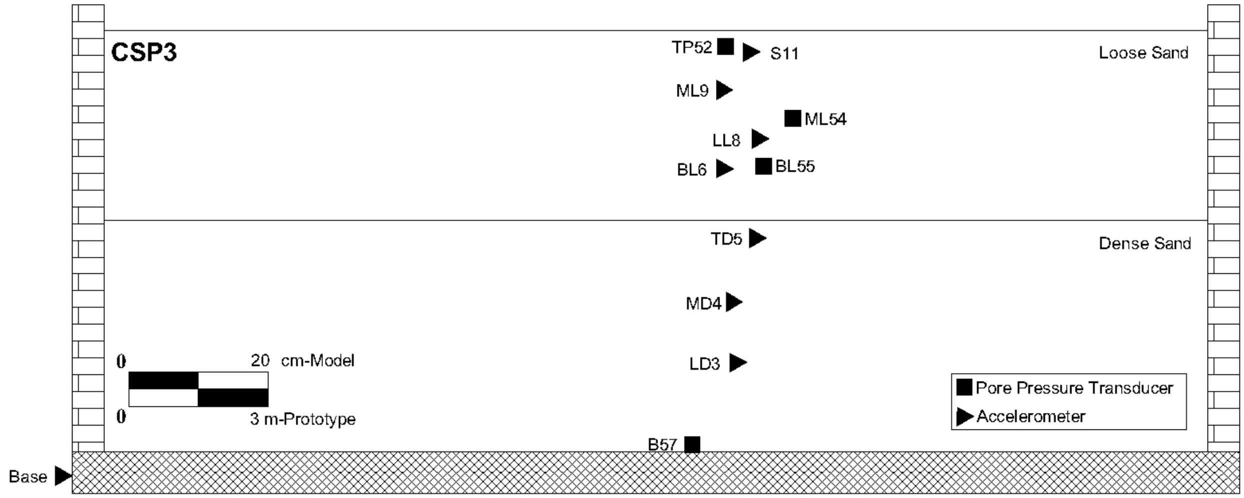

Figure 5.9 Sensors from CSP3 utilized in this study (pile foundations omitted for clarity).

Unfortunately, a shear wave velocity profile was not measured for the centrifuge tests. However, local experience with Nevada sand indicates that the shear wave velocity profile can be defined using the functional form:

$$V_s = V_{s1}\left(\frac{p'}{p_a}\right)^n \tag{5.9}$$

where p_a is atmospheric pressure, V_{s1} = 250 m/s for medium dense sand and 280 m/s for dense sand, and n=0.5. Furthermore, we assume K_o=0.5 for defining the mean effective stress profile.

5.6 SITE RESPONSE MODELING

Four different site response modeling approaches were used to analyze the centrifuge test data, as summarized in Table 5.1. Models 8, 9, ad 10 are performed in DeepSoil whereas OpenSees is used for Model 11. The Menq (2003) modulus reduction and damping curves were used to model the dynamic properties of the sand. The friction angle for the medium dense layers was assumed 35° and it was assumed 40° for dense layers. The target strength for each of the 50 layers in the site response models was achieved using the Yee et al. (2013) procedure previously explained in the total stress analysis section. For the DeepSoil nonlinear site response models, the "target" modulus reduction curve was seeded with erroneous values at high strain to obtain a least squares hyperbolic curve fit that provides the desired shear strength, as described in the previous chapter. For all of the models, unit weights were 19.5 kN/m^3 for the medium dense layer and 20.0 kN/m^3 for the dense layer.

Table 5.1 Properties of models for effective stress analysis

Model #	Nonlinear (NL) or Equivalent Linear (EQ)?	Modeling Platform	Modulus Reduction Curve	Damping Curve	Pore Pressure Generation Model or Constitutive Model
Model 8	EQ	DeepSoil	Menq, 2003	Menq, 2003	N/A
Model 9	NL	DeepSoil	Menq, 2003	Menq, 2003	Matasovic (1992)
Model 10	NL	DeepSoil	Menq, 2003	Menq, 2003	Green et al. (2000)
Model 11	NL	OpenSees	Menq, 2003	Masing's Rules	Elgamal et al. (2003)

The DeepSoil nonlinear site response models require additional parameters to define pore pressure generation and the rate of shear modulus reduction, and the OpenSees model requires additional constitutive modeling parameters. Model 9 follows the Matasovic approach using curve fitting parameters, p=1.1, F=2.6, and s = 1.7. The volumetric threshold shear strain was set to 0.02% and v is assumed 3.8 for the model based on results presented for Santa Monica beach sand by Matasovic. Model 10 uses the procedure by Green et al. (2000) assuming D_r=55% for the medium dense layers and D_r=85% for the dense layers. The fines content was assumed 0. Model 11 uses the PressureDependMultiYield model and simulations were performed using

Cyclic 1-D, a user interface developed specifically for nonlinear effective stress site response. Input parameters for the two different layers are summarized in Table 5.2.

Table 5.2 Model parameters for Model 11.

Model parameters	Medium Dense	Dense
Depth Range (m)	0-8.4	8.4-19.2
Reference Shear Wave Velocity, V_{s1} (m/s)[a]	235	250
Reference Confining Pressure, p_r (kPa)	100	100
Confinement Dependence Coefficient, n	0.5	0.5
Lateral Earth Pressure Coefficient, K_o	0.5	0.5
Friction Angle, ϕ' (deg)	35	40
Cohesion, c (kPa)	0	0
Peak Shear Strain (%)	10	10
Number of Yield Surfaces	20	20
Dilat2	4.5	5
liquefac1	0	0
Dilation Angle, ψ (deg)	27	27
Contraction Parameter 1	0.03	0.03
Contraction Parameter 2	0.6	0.6
Dilation Parameter 1	0.75	0.8
Dilation Parameter 2	4.5	5
Liquefaction Parameter 1	0	0
Permeability Coefficient (m/s)	0.0001	0.0001

a) $V_s = V_{s1}\left(\frac{p'}{p_r'}\right)^n$

5.7 COMPARISON OF SITE RESPONSE SIMULATIONS WITH MEASURED RESULTS

Acceleration records at four different depths in the model are presented in Figure 5.10, along with acceleration response spectra for the motions recorded at these elevations. Pore pressure records are shown in Figure 5.11 at several depths where measurements were obtained in the centrifuge tests. Turning first to the acceleration response, at a depth of 15.3 m all of the model predictions agree reasonably well with the measured acceleration records because this recording is fairly close to the base of the model container, and the ground motion does not differ significantly from the base motion. As depth becomes shallower, the model predictions begin to diverge from each other and from the measured ground motion. At a depth of 0.5m (the shallowest recorded ground motion), the recorded motion exhibits a sharp pulse at approximately t = 10s. This acceleration pulse is reproduced in the OpenSees simulation, but not in the other simulation procedures. Shortly after this acceleration pulse, the excess pore pressure ratio reached approximately 1.0 (see Figure 5.11) indicating liquefaction occurred in the medium dense layer. Following liquefaction, a number of additional acceleration pulses are present in the record, and these pulses are associated with transient reductions in the excess pore pressure ratio. These pulses are also captured by the OpenSees simulation, but not the other simulations. Both pore pressure generation models predict significantly lower ground motion than what was measured following liquefaction triggering. In fact, the equivalent linear simulation predicts more accurate post-liquefaction ground motion amplitude than the pore pressure generation models, although the frequency content of the equivalent linear ground motion does not agree with measurements.

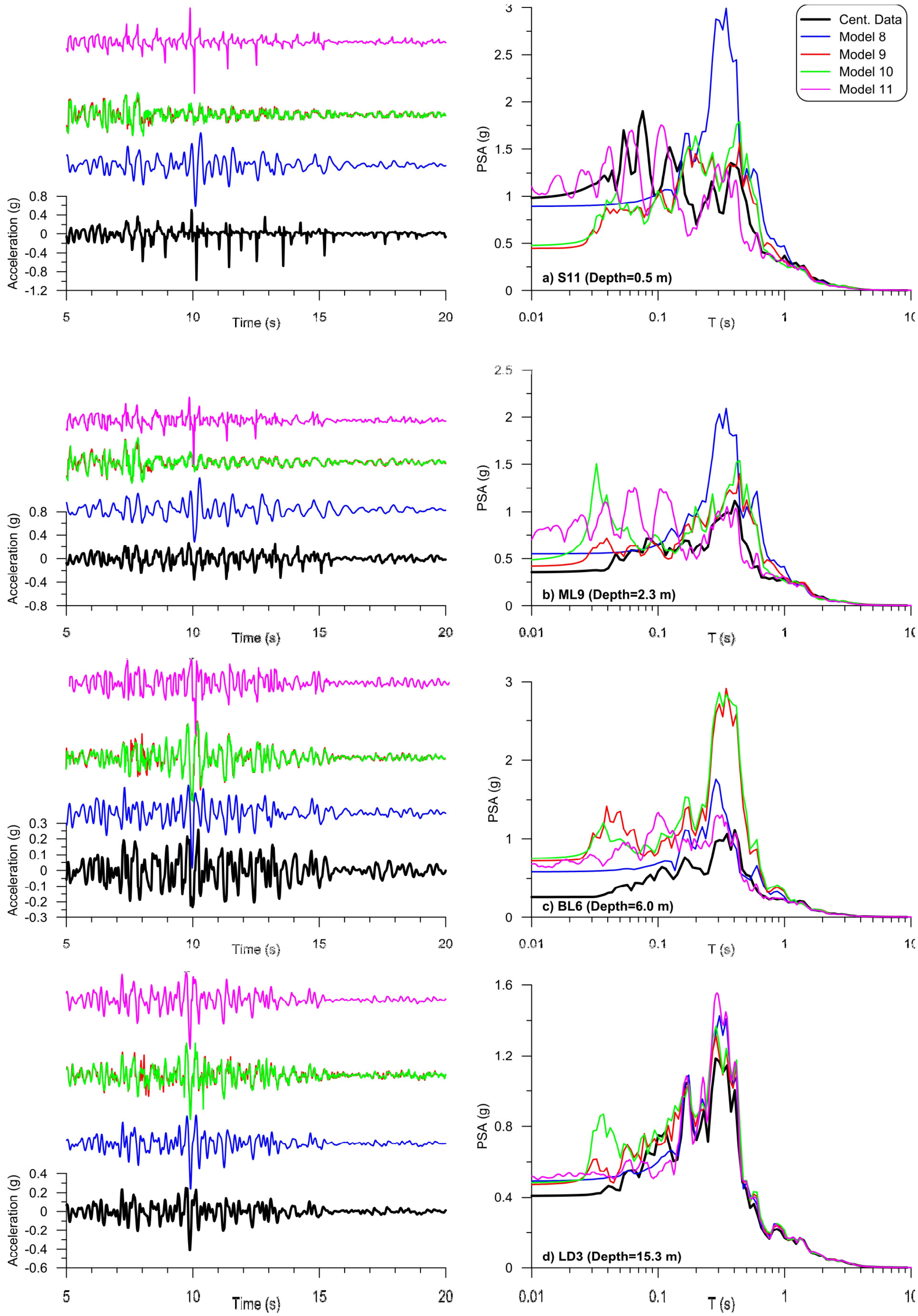

Figure 5.10 Ground motion predictions at various depths using four different modeling approaches.

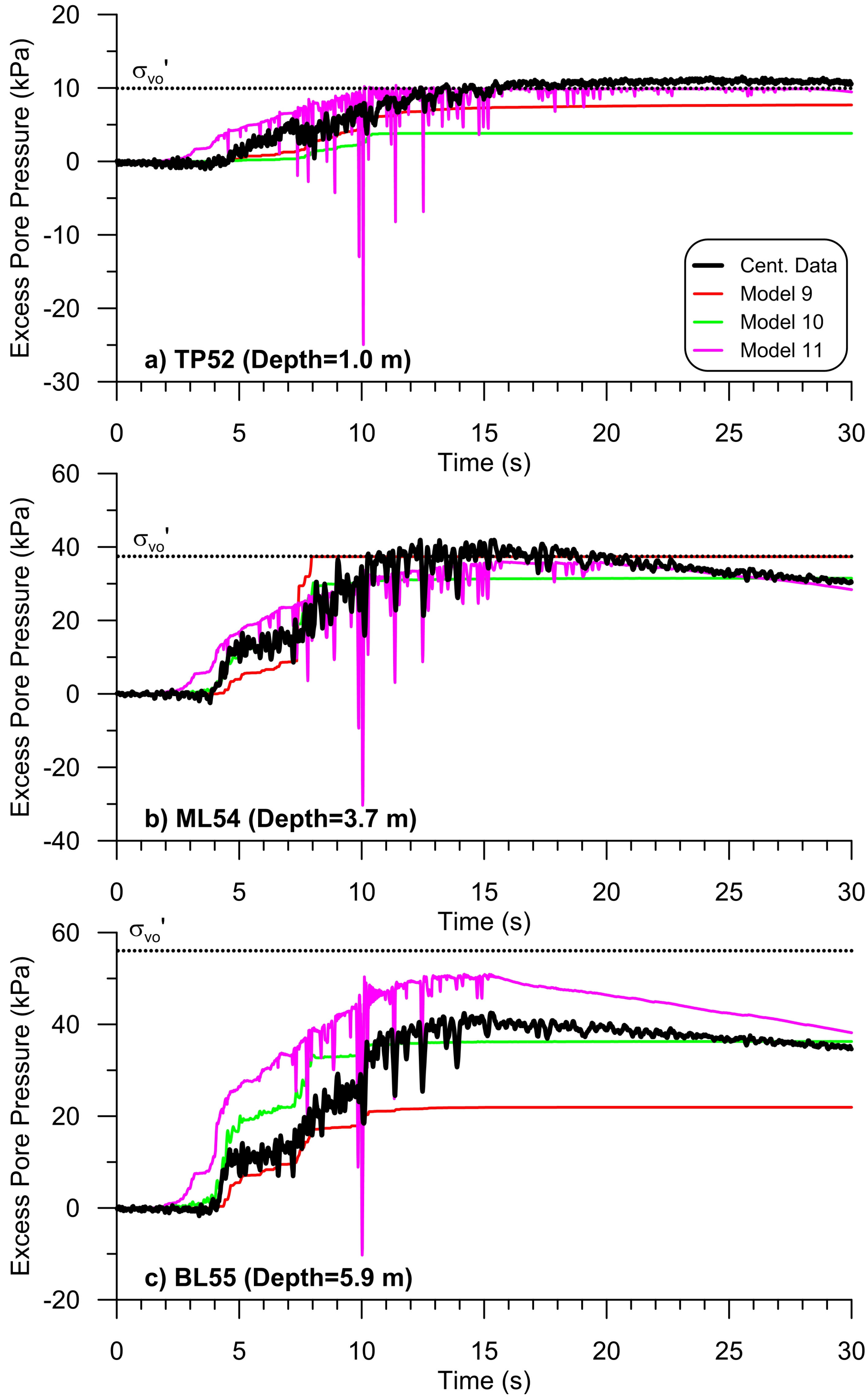

Figure 5.11 Measured and predicted pore pressure responses.

Turning to the pore pressure responses, the centrifuge model reached a condition of full liquefaction at depths of 1.0m and 3.7m, but did not approach full liquefaction at 5.9m. The Model 9 simulation predicted that none of the layers would fully liquefy (i.e., reach a condition of zero effective stress), whereas the Model 10 simulation predicted full liquefaction at depths of 5.9m and 3.7m, but not at 1.0m. The OpenSees simulation (Model 11) predicted full liquefaction at depths of 1.0m and 3.7m, but not at 5.9m, which agrees well with measurements. The Model 10 simulation illustrates a base isolator effect, in which full liquefaction deep in the profile reduces propagation of earthquake ground motion at shallower depths, thereby shielding these shallow layers from liquefying. On the other hand, significant motion did propagate through the soil profile and the near-surface layers did liquefy. Also note that Model 9 and 10 predict a monotonically increasing excess pore pressure ratio, whereas the measurements and Model 11 predict transient oscillations in which excess pore pressure ratio decreases. Model 11 is therefore more accurate than Models 9 and 10 in this regard.

Profiles of peak acceleration and peak shear strain are shown in Figure 5.12. Model 10 exhibits a concentration of high shear strain at a depth of approximately 4m, where full liquefaction is predicted for this model. A similar concentration of strain occurs at a depth of 3m for Model 9, although this model did not fully liquefy. The concentration of strain in a particular layer can be easily explained by the modeling assumption that pore pressure can only increase, but never decrease, using a pore pressure generation model. As pore pressures begin to increase in the element with the highest shear strain demand, the soil softens and accumulates more strain thereby generating even more pore pressure. This process continues until this element has fully liquefied. After liquefaction, very little ground motion propagates through the liquefied zone since this element is so soft forming what has been called a "base isolator" effect, which explains why the shear strains are smaller at depths shallower than the critical element. However, this "base isolator" effect is not observed in the measured data. The peak measured acceleration was nearly 1.0g at a depth of 0.5m, compared with predicted accelerations of only about 0.4g using the pore pressure generation models. By contrast, the OpenSees model predicts the acceleration at this depth reasonably well. The OpenSees model over-predicts accelerations deeper within the model, which could be related to modeling errors, or non-one-dimensional wave propagation due to container effects in the centrifuge model.

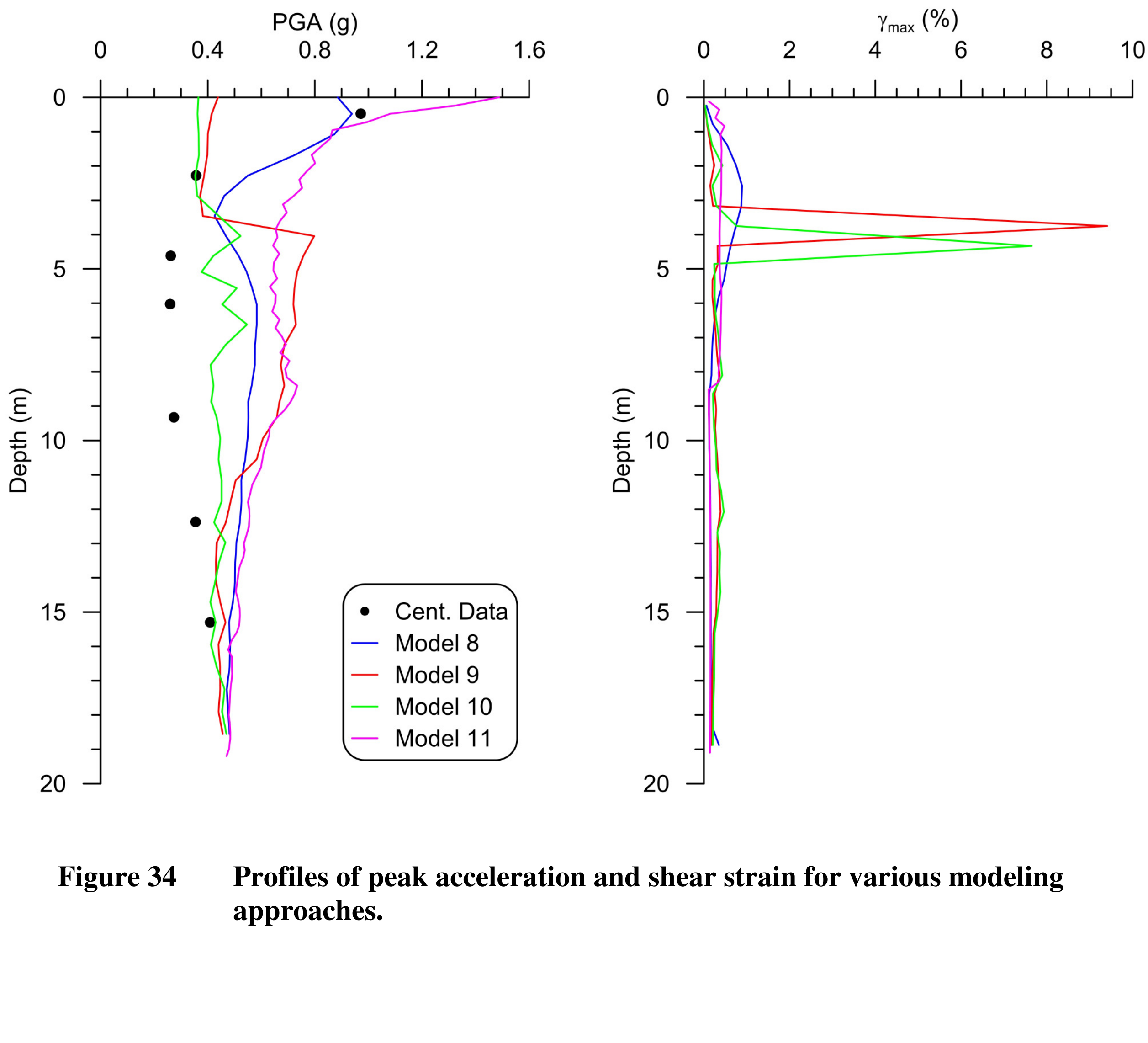

Figure 34 Profiles of peak acceleration and shear strain for various modeling approaches.

6 CONCLUSION AND RECOMMENDATIONS FOR FUTURE RESEARCH

This dissertation presented a centrifuge modeling study of site response in soft clay spanning a broad strain range that includes nearly linear and strongly nonlinear soil behavior. The model response was characterized using dense sensor arrays and 1-D shaking conditions were achieved using an innovative hinged-plate container. The test data provides a useful resource for validating nonlinear site response from empirical models and wave propagation routines.

Modulus reduction and damping values back-calculated from the recorded acceleration data indicate modest misfit relative to empirical models within the strain range of applicability of those models (γ_c< ~ 0.3%). The bias is towards the models having too-high modulus reduction at low strain and too-low damping. The damping values exhibited significant scatter as a result of the complex shapes of the hysteresis loops that result from broadband excitation. Perhaps the most significant aspect of the observed soil behavior was a large-strain response in which mobilized shear stresses significantly exceeded the undrained monotonic shear strength by factors on the order of 1.5 to 2.0. These large stresses mobilize at shear strains beyond approximately 5%. We attribute these high stresses to strain-rate effects that temporarily increase the available shear resistance in the clay during strong shaking. Following the recommendation of Sheahan et al. (1996) that shear strength increases by 9% per log-cycle increase in strain rate, shear strength at the model scale strain rates observed in the centrifuge models would be 67% higher than observed at typical laboratory strain rates. Although strain rates in the centrifuge are unrealistically high, strength increases on the order 40% would be expected based on the prototype strain rates more representative of field conditions compared with the much lower strain rates in typical laboratory tests. The rate correction is therefore a potentially important consideration for selecting shear strength for nonlinear site response studies.

Spectral amplification factors observed from centrifuge modeling are compared to levels predicted by nonlinear site factors in ground motion prediction equations. Of particular interest in these comparisons is the nonlinearity of site response, which is typically quantified by the rate of change of amplification with base peak acceleration (PHA_b). When plotted in log-log space, amplification levels decrease nearly linearly with increasing PHA_b at a slope denoted as b. Values of b are poorly constrained by empirical ground motion databases, particularly for the soft soil condition utilized in the centrifuge modeling. The interpreted b-values indicate substantial nonlinearity for periods at and below the elastic site period of approximately 1.0s and effectively linear response at longer periods (e.g., 3.0s).

Site response simulations were run using DeepSoil and OpenSees, and compared with centrifuge test measurements. Total stress analysis procedures were compared with centrifuge models of soft clay that were shaken with strong enough ground motion to induce strains higher than 10%, resulting in shear failure of the soil. Parameter variations in the site response simulations included the modeling approach (equivalent linear versus nonlinear), shear strength of the soil including corrections for strain rate effects, and nonlinear modeling platform (DeepSoil versus OpenSees).

The most important conclusions drawn from the total stress site response simulations presented in this study are as follows:

- Accurately modeling the shear strength of the soft clay was crucial to obtaining accurate ground motion predictions. The large-strain portion of the modulus reduction curve should be adjusted to obtain a desired shear strength, and the functional form of the modulus reduction equations (experimentally calibrated to strains only up to about 0.3%) should not be extrapolated to large strain. Yee et al. (2013) suggest a procedure for adjusting the modulus reduction curve to obtain a desired strength profile.
- Shear strain rate played a crucial role in increasing the shear strength mobilized during the centrifuge tests, and should be included in nonlinear site response simulations. Mobilized shear stresses exceeded monotonic undrained shear strengths by more than a factor of two due to the very large mobilized strain rates (as high as 6000%/s). Although model scale strain rates in the centrifuge are significantly higher than those anticipated at an equivalent prototype site (strain rate scales with centrifugal acceleration, in this case 57g), very large strain rates would also be anticipated under more realistic shaking conditions. The procedure suggested by Sheahan et al. is calibrated over typical laboratory strain rates, and extrapolation of this procedure resulted in an under-prediction of strength at high strain rates. However, this procedure appears to be suitable for strain rates that would be anticipated for field shaking conditions that mobilize strain rates lower than in centrifuge models due to centrifugal time scaling factors. More research is required to obtain strain rates for the range anticipated during earthquake shaking at soft soil sites.

- Nonlinear site response simulations utilizing the correct shear strength profile provided the most accurate results. Bias in model predictions that utilize an incorrect strength profile increases as shaking intensity increases. However, bias is present for small input motions as well because the strength correction adjusts the modulus reduction curves at strains as small as 0.1%.
- Equivalent linear simulations can be adjusted to reasonably capture the peak response during any particular ground motion, but the amplitude and phase of these simulations were found to differ significantly from the data for smaller cycles. This is caused by the assumption that the strain-compatible modulus and damping values do not change in time, whereas in reality the secant modulus and damping evolve during shaking because strain amplitude also evolves.

Effective stress site response models were compared with centrifuge test data for a soil profile consisting of medium dense sand overlying dense sand. The model was shaken with a sequence of ground motions that generated large excess pore pressures in the model, resulting in liquefaction of the medium dense layer. High amplitude, high frequency acceleration pulses propagated through the liquefied soil profile due to the dilatant response of the sand in undrained loading. The models were analyzed using various nonlinear site response procedures and an equivalent linear site response method.

The primary conclusions from this section of the report are as follows:

- Ground motion records in liquefiable soils from field measurements and laboratory modeling studies indicate that liquefiable sand can propagate significant seismic energy in the form of high frequency pulses caused by the dilatant tendency of the sand being suppressed in undrained loading.

- Two classes of nonlinear effective stress site response modeling were studied: (1) pore pressure generation models that degrade the backbone stress-strain curve stiffness, and result in monotonic increases in excess pore pressure, and (2) advanced constitutive models that capture the tangent stiffening in the stress-strain behavior associated with the dilatant tendency of the sand being suppressed in undrained loading.
- Pore pressure generation models are incapable of capturing the transient stiffening associated with dilatancy in liquefiable deposits, and therefore fail to capture the acceleration pulses that propagate through liquefied sand. These models predict a "base isolator" effect in which surface motions are significantly reduced by the formation of a single layer that liquefies and reflects seismic energy downward. The "base isolator" effect is not supported by measurements of ground motions in liquefiable soils, and these models should not be used to predict post-liquefaction ground motions. In fact, the equivalent linear simulations predicted post-liquefaction ground motion better than these effective stress models.
- Advanced constitutive models that capture the dilatant tendency of liquefiable sands are capable of producing acceleration pulses similar to those observed in real ground motions in liquefiable soils. Although the model studied in this report qualitatively was able to capture the acceleration pulses, the amplitude of the pulses was not perfectly captured. More research will be required to resolve this issue.

All of the nonlinear effective stress models accurately predicted liquefaction triggering of the centrifuge model. Hence, the pore pressure generation models may be useful for modeling triggering of liquefaction, but post-liquefaction ground motions were significantly unconservative.

As mentioned earlier, shear strain rate is an important phenomenon that should be considered in nonlinear site response simulations. Sheahan et al. (1996) procedure doesn't provide a good fit to centrifuge data since the strain range that Sheahan et al. suggests is very small compared to the test data. The high strain rate ranges that matches with the centrifuge data was studied by Yong and Japp in 1969 however the procedure didn't also provide a good approach to capture the test data. Therefore laboratory testing of the bay mud is needed to better understand the rate effect on undrained strength for future research. As the highest recorded shear strain rate was as high as 6000%/s in the centrifuge data, the test should aim to reach higher strain rates than Sheahan et al. tested.

Regarding the nonlinear effective site response, more complicated, advanced constitutive models such as PM4Sand (Boulanger and Ziotopoulou) and Kramer's model should be run in order to understand the stress-strain behavior of liquefiable sands, especially dilatancy behavior of the soil. Advanced constitutive models will help us to understand this fundamental feature of sand which is not considered by pore pressure generation models. In order to do that, first, the required input parameters should be identified. Later, the results of these constitutive models should be compared to understand the strengths and weaknesses of the model approaches. These models can be tested by applying field arrays such as Wildlife and Port Island and or data sets from the Tohoku earthquake in Japan. This work will improve the constitutive models in terms of parameter selection and better capturing the observed behavior. Finally, these validated models can be used to run simulations for soil profiles with variations to develop statistical amplification factors for use in ground motion prediction equations. This research is beyond the scope of this dissertation; however I plan to undertake this work as a professor.

REFERENCES

Afacan, K.B., Brandenberg, S.J., and Stewart, J.P. (2014). "Centrifuge Modeling Studies of Site Response in Soft Clay over Wide Strain Range.", Journal of Geotechnical and Geoenvironmental Engineering, 140(2), 04013003

Afacan, K.B., Harounian, A., Brandenberg, S.J., and Stewart, J.P., (2011). "Evaluation of non-linear site response of soft clay using centrifuge models: Centrifuge data report for AHA02." *UCLA-SGEL Report*, University of California, Los Angeles, 43 pgs.

Baturay, M.B. and Stewart, J.P. (2003). "Uncertainty and bias in ground motion estimates from ground response analyses."*Bull. Seism. Soc. Am.*, 93 (5), 2025-2042.

Bolton, M. D. "The strength and dilatancy of sands." Geotechnique 36.1 (1986): 65-78.

Booker, John R., M. Shamimur Rahman, and Harry Bolton Seed. "GADFLEA: A computer program for the analysis of pore pressure generation and dissipation during cyclic or earthquake loading." Unknown 1 (1976).

Boore, D.M. and Atkinson, G.M. (2008)."Ground-motion prediction equations for the average horizontal component of PGA, PGV, and 5%-damped PSA at spectral periods between 0.01s and 10.0s."*Earthquake Spectra*. 24(1), 99-138.

Boore, D.M. and Bommer, J.J. (2005). "Processing of strong-motion accelerograms: needs, options and consequences." *Soil Dyn. Earthquake Engrg.*, 25(2), 93-115.

Borcherdt, R.D., (1994). "Estimates of site-dependent response spectra for design (Methodology and Justification)." *Earthquake Spectra*, 10, 617-653.

Boulanger, Ross W., and Stephen P. Truman. "Void redistribution in sand under post-earthquake loading." Canadian geotechnical journal 33.5 (1996): 829-834.

Boulanger, R.W., and Ziotopoulou, K. (2012). "PM4Sand (Version 2): a sand plasticity model for earthquake engineering." Department of Civil and Environmental Engineering, University of California, Davis, Report. No. UCD/CGM-12/01, 101p.

Brandenberg, S.J., Boulanger, R.W., Kutter, B.L., and Chang, D. (2005). "Behavior of pile foundations in laterally spreading ground during centrifuge tests." J. Geotech. Geoenviron. Eng., ASCE., 131(11), 1378-1391.

Brandenberg, S.J., Kutter, B.L., and Wilson, D.W. (2008). "Fast stacking and phase corrections of shear wave signals in a noisy environment."*J. Geotech. Geoenviron. Eng.,* ASCE, 134(8), 1154-1165.

Brandenberg, S.J., Stewart, J.P., Afacan, K.B., Harounian, A., Deng, L., and Park, D. (2010). "Final Report for USGS Award Number 08HQGR0037: Evaluation of nonlinear site response of soft clay using centrifuge models." United States Geological Survey. 33pg

Chiou, B.S.J., Darragh, R., Dregor, D., and Silva, W.J. (2008).“NGA project strong-motion database,” *Earthquake Spectra,* 24, 23-44.

Choi, Y and Stewart, J.P., (2005). "Nonlinear site amplification as function of 30 m shear wave velocity,"*Earthquake Spectra,* 21, 1-30.

Dafalias, Y.F., and Manzari, M.T. (2004). "Simple plasticity sand model accounting for fabric change effects." *J. Engineering Mechanics*, ASCE, 130(6), 622-634.

Darendeli, M. B. (2001). “Development of a new family of normalizedmodulus reduction and material damping curves.” Ph.D. thesis, Univ. ofTexas, Austin, TX.

Elgamal, A., Yang, Z., Parra, E., and Ragheb, A. (2003). "Modeling of cyclic mobility in saturated cohesionless soils." *International Journal of Plasticity*, 19(03) 883-905.

Elgamal, A., Lai, T., Yang, Z., and He, L.(2001). “Dynamic soil properties, seismic downholearrays and applications in practice.”*Proc., 4th Int. Conf. on Recent Advances in Geotechnical EarthquakeEngineering and Soil Dynamics*, Univ. of Missouri-Rolla, San Diego.

Elgamal, A., Yang, Z., Lai, T., Kutter, B.L., and Wilson, D.W.(2005). "Dynamic response of saturated densesand in laminated centrifuge container."*J. Geotech. &Geoenviron. Eng.*, 131(5), 598-609.

Fiegel, G. L. (1995). “Centrifugal and Analytical Modeling of Soft Soil Sites Subjected to Seismic Shaking.” *PhD Thesis*, The University of California, Davis.

Green, R.A., Mitchell, J.K. and Polito, C.P. (2000). "An Energy-Based Pore Pressure GenerationModel for Cohesionless Soils", Proceedings: John Booker Memorial Symposium, Melbourne,Australia, November 16-17, 2000.

Hardin,B.O. and Drnevich, V.P. (1972). “Shear modulus and damping in soils: design equations and curves.” *J. of the Soil Mechanics and Foundations Div*., ASCE, 98 (SM7), 667-692.

Harounian,A.(2010). “Evaluation of non-linear site response of soft clay using centrifuge models: Centrifuge data report for AHA01.”*M.S. Thesis*, University of California, Los Angeles, Los Angeles, CA.

Harounian, A., Afacan, K.B., Stewart, J.P., and Brandenberg, S.J. (2013a). “AHA01: Evaluation of nonlinear site response of soft clay using centrifuge models.” Network for Earthquake Engineering Simulation (database).Dataset.DOI: 10.4231/D32B8VB9D

Harounian, A., Afacan, K.B., Stewart, J.P., and Brandenberg, S.J. (2013b). “AHA02: Evaluation of nonlinear site response of soft clay using centrifuge models.” Network for Earthquake Engineering Simulation (database).Dataset.DOI: 10.4231/D3XK84Q4D

Hashash, Y.M., Philips, C., and Groholski, D.R. (2010). "Recent advances in non-linear site response analysis." *5th International Conference on Recent Advances in Geotechnical Earthquake Engineering and Soil Dynamics*, May 24-29, San Diego, Paper no. OSP 4.

Holzer, Thomas L., and T. Leslie Youd. "Liquefaction, ground oscillation, and soil deformation at the Wildlife Array, California." Bulletin of the Seismological society of America 97.3 (2007): 961-976.

Jaky, J. (1944). "The coefficient of earth pressure at rest."*J. Soc. Hung.Archit. Eng.*, 78 (22), 355–358.

Kramer, S.L. and Paulsen, S.B. (2004). "Practical use of geotechnical site response models." *Proc. Int. Workshop on Uncertainties in Nonlinear Soil Properties and their Impact on Modeling Dynamic Soil Response*, PEER Center Headquarters, Richmond, CA

Kayen, Robert, et al. "Geoengineering and seismological aspects of the Niigata-Ken Chuetsu-Oki earthquake of 16 July 2007." Earthquake Spectra 25.4 (2009): 777-802.

Kwok, A.O., Stewart,J.P., Hashash, Y.M.A., Matasovic, N., Pyke, R., Wang, Z.,and Yang, Z. (2007)."Use of exact solutions of wave propagation problems to guide implementation of nonlinear seismic ground response analysis procedures." *J. Geotech.&Geoenv. Eng.*, ASCE, 133 (11), 1385-1398.

Kutter, Bruce L., and Daniel W. Wilson. "De-liquefaction shock waves." Proc., 7th US–Japan Workshop on Earthquake Resistant Design of Lifeline Facilities and Countermeasures Against Soil Liquefaction, Rep. MCEER-99. Vol. 19. 1999.

Ladd, C.C. (1991). "Stability evaluation during staged construction."*J. Geotech.Eng. Div.,* ASCE, 117(4), 540-615.

Lai, T., Elgamal, A., Wilson, D.W., and Kutter, B.L. (2001). "Numerical modeling for site seismic response in laminated centrifuge container." *Proc. 1st Albert CAQUOT Int. Conf.*, Paris.

Lee, J.S. and Santamarina, J.C. (2005)."Bender elements: Performance and signal interpretation."*J.Geotech. &Geoenviron. Eng.*, ASCE, 131 (9), 1063-1070.

Martin, G.R., and Qiu, P., 2001, "Site Liquefaction Evaluation: TheApplication of Effective Stress Site Response Analyses," drafttechnical report prepared for the Multidisciplinary Center forEarthquake Engineering Research, Buffalo, NY.

Matasovic, N. (1992) "Seismic response of composite horizontally-layered soil deposits." Ph.D.Thesis, University of California, Los Angeles.

Mason, H.B., Kutter, B.L., Bray, J.D., Wilson, D.W., and Choy, B.Y. (2010). "Earthquake motion selection and calibration for use in a geotechnical centrifuge." *7th International Conference on Physical Modeling in Geotechnics,* Zurich Switzerland, July 2010.

Menq, Farn-yuh. (2003) "Dynamic properties of sandy and gravelly soils". Ph.D. thesis, Univ. ofTexas, Austin, TX.

Park, D.S. (2011). "Strength loss and softening of sensitive clay slopes." *PhD Thesis*, University of California, Davis, Davis, CA.

Park, D., and Y. M. A. Hashash (2004) "Soil damping formulation in nonlinear time domain siteresponse analysis," Journal of Earthquake Engineering, Vol. 8, No. 2, pp 249-274.

Phillips, C., and Hashash, Y.M.A. (2009). "Damping formulation for nonlinear 1-D site response analyses", *Soil Dynamics and Earthquake Engineering,"* 29, 1143–1158.

Polito, Carmine P., Russell A. Green, and Jongwon Lee. "Pore pressure generation models for sands and silty soils subjected to cyclic loading." Journal of Geotechnical and Geoenvironmental Engineering 134.10 (2008): 1490-1500.

Santamarina, J.C., Klein K.A., and Fam, M.A. (2001). “Soils and waves.” John Wiley & Sons, Ltd., Chicester, West Sussex, England., 488 p.

Schmidt, B. (1966). “Discussion of earth pressures at rest related to stress history.” *Canadian Geotechnical Journal*, III (4), 239-242.

Seed, Harry Bolton, Philippe P. Martin, and John Lysmer. “The generation and dissipation of pore water pressures during soil liquefaction”. College of Engineering, University of California, 1975.

Seed, H.B., De Alba, P.M., 1986. Use of SPT and CPT tests for Evaluating the Liquefaction Resistance of Sands. Proc., INSITU'86. ASCE Spec. Conf. on Use of In Situ testing in Geotechnical Engg., Spec. Publ. No. 6. ASCE, New York, N.Y.

Seyhan, Emel, and Jonathan P. Stewart. "Semi-empirical nonlinear site amplification from NGA-West 2 data and simulations." Earthquake Spectra(2014).

Sheahan, T., Ladd, C., and Germaine, J. (1996). ”Rate-dependent undrained shear behavior of saturated clay.” *J.Geotech. &Geoenviron. Eng.*, ASCE, 122(2), 99–108.

Sheather, S.J. (2009). A Modern Approach to Regression with R.Springer Science Business Media, New York, NY, 407 pg.

Stewart, J.P. and Kwok, A.O. (2008). "Nonlinear seismic ground response analysis: code usage protocols and verification against vertical array data.” *Geotechnical Engineering and Soil Dynamics IV,*, May 18-22, 2008, Sacramento, CA, ASCE Geotechnical Special Publication No. 181, D. Zeng, M.T. Manzari, and D.R. Hiltunen (eds.), 24 pgs

Tsai, C..C. and Hashash,Y.M. (2009)."Learning of dynamic soil behavior from downholearrays."*J. Geotech. &Geoenviron. Eng.*, ASCE, 135(6), 745-757.

Vucetic, M. and Dobry, R. (1991). “Effect of soil plasticity on cyclic response.”*J. Geotech. &Geoenviron. Eng.*, ASCE, 114(2), 133–149.

Walling, M., Silva, W.J., and Abrahamson, N.A. (2008). “Nonlinear site amplification factors forconstraining the NGA models.” *Earthquake Spectra*, 24, 243–255.

Wilson, D.W., Boulanger, R.W., and Kutter, B.L. (1997). "Soil-pile-superstructureinteraction at soft or liquefiable soil sites - Centrifuge data report for Csp5."Report No. UCD/CGMDR-97/06, Center for Geotechnical Modeling, Departmentof Civil and Environmental Engineering, University of California, Davis.

Wilson, D.W., Boulanger, R.W., and Kutter, B.L. (2000). "Observed seismic lateral loading resistance of liquefying sand." *J. Geotech. Geoenviron. Eng.* 126(10), 898-906.

Yamada, S., Hyodo, M., Orense, R. P., Dinesh, S. V., and Hyodo, T. (2008). “Strain-dependent dynamic properties of remolded sand-clay mixtures.”*J. Geotech. &Geoenviron.Eng*.,ASCE, 134(7), 972–981.

Yee, E., Stewart, J.P., and Tokimatsu, K. (2013). “Elastic and large-strain nonlinear seismic site response from analysis of vertical array recordings.” *J. Geotech. Geoenviron. Eng.,* DOI: 10.1061/(ASCE)GT.1943-5606.0000900

Yong, R. N., and R. D. Japp. "Stress-strain behavior of clays in dynamic compression." Vibration effects of earthquakes on soils and foundations, ASTM Special Technical Publication 450 (1969): 233-262.

Zeghal, M. and A. W. Elgamal. (1994). “Analysis of site liquefaction using earthquake records.”*J. Geotech. &Geoenviron.Eng*.,ASCE, 120 (6), 996-1017.